

# INDUCED STRAIN OF ACTUATION OF SURFACE BONDED AND EMBEDDED PIEZOCERAMIC PATCHES

by

David Hilton Mollenhauer

Thesis submitted to the Faculty of the Virginia Polytechnic Institute and State University in partial fulfillment of the requirements for the degree of

MASTER OF SCIENCE

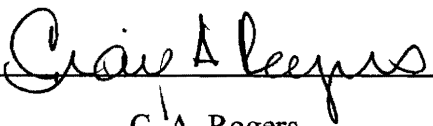
in

Engineering Mechanics

APPROVED:



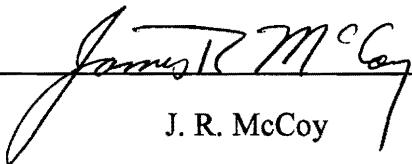
O. H. Griffin, Jr., Chairman



C. A. Rogers



D. T. Mook



J. R. McCoy

April, 1992

Blacksburg, Virginia

5055

V855

1992

M644

C.2

# **INDUCED STRAIN OF ACTUATION OF SURFACE BONDED AND EMBEDDED PIEZOCERAMIC PATCHES**

by

David Hilton Mollenhauer

Committee Chairman: O. H. Griffin, Jr.  
Engineering Science and Mechanics

(ABSTRACT)

The strain induced into isotropic flat plates by surface bonded and embedded piezoceramic patches was investigated. The free piezoceramic patch voltage/strain response was characterized using moiré interferometry and Twyman-Green interferometry techniques. Moiré interferometry experiments were conducted to investigate the induced strain of actuation in a flat plate with two surface bonded piezoceramic patches and a flat plate with one embedded patch. Three-dimensional finite element models of these two specimens were constructed and analyzed.

The measured in-plane voltage/strain response of a free piezoceramic patch was found to be nearly linear and of a much higher magnitude than the published data. Similarly, the out-of-plane voltage/strain response was found to be much higher in magnitude than the published data as well as being non-linear.

Correlation between the moiré experiment concerning the surface bonded patch specimen and the corresponding finite element model was good, indicating the validity of the modeling technique. Possible depoling damage of the embedded patch caused the correlation between the experiment and analysis of this specimen to be poor. Both finite element models predicted stresses that are not statically significant but may represent problems over many loading cycles.

## **Acknowledgements**

The author of this work was funded through the Palace Knight Program of the United States Air Force. Piezoceramic materials were provided by Dr. C. A. Rogers, director of the Center for Intelligent Material Systems and Structures at Virginia Polytechnic Institute and State University (VPI&SU). The assistance provided by Dr. D. Post, Dr. B. Han, and Mr. P. Ifju of the Department of Engineering Science and Mechanics at VPI&SU, without whom the experimental portion of this work would not have been possible, is gratefully appreciated. Thanks to Mrs. Danniella Thompson for her guidance and assistance with available computer facilities and techniques. Thanks also to Dr. C. A. Rogers and Dr. D. T. Mook at VPI&SU and Dr. J. R. McCoy at Wright Laboratories for their service on this committee. Special thanks to Dr. O. H. Griffin, Jr. for serving as committee chairman. His excellent blend of guidance while allowing self-determination is especially appreciated.

# Table of Contents

<b>Chapter 1: Introduction and Review of Literature .....</b>	<b>1</b>
1.1 Overview of Intelligent Material Systems and Research Focus.....	1
1.1.1 Intelligent Material Systems: Definitions and Examples .....	1
1.1.2 Actuator and Sensor Material Candidates .....	3
1.1.3 Focus of Research .....	4
1.2 Analysis Techniques Applied to Piezoceramic Based Hybrid Structures.....	5
1.2.1 Analysis Techniques Examined by the Research Community.....	5
1.2.2 Analysis Techniques Used in This Study .....	7
1.3 Experimental Techniques Used in This Research .....	8
1.3.1 Experiments Performed .....	8
1.3.2 Moiré Interferometry.....	9
1.3.3 Twyman-Green Interferometry .....	11
<b>Chapter 2: Free Piezoceramic Voltage Response Characterization.....</b>	<b>13</b>
2.1 In-plane Voltage Response Characterization .....	13
2.1.1 Set-up of Moiré Interferometry Experiment.....	13
2.1.2 Specimen Construction and Grating Replication.....	15
2.1.3 Testing and Results.....	18
2.2 Out-of-plane Voltage Response Characterization .....	23
2.2.1 Set-up of Twyman-Green Interferometry Experiment.....	23
2.2.2 Testing and Results.....	25

<b>Chapter 3: Induced Strain of Actuation in a Flat Plate With Surface Bonded Piezoceramic Patches .....</b>	<b>29</b>
3.1 Moiré Interferometry Experiment .....	29
3.1.1 Specimen Geometry, Construction, and Materials .....	29
3.1.2 Test Set-up and Experimental Procedure .....	30
3.2 Finite Element Modeling.....	33
3.2.1 The Finite Element Model .....	33
3.2.2 Finite Element Analysis.....	33
3.3 Results and Comparisons .....	35
3.3.1 Discussion of Moiré Fringe Pattern Results .....	35
3.3.2 Comparison of Moiré Fringe Patterns to Finite Element Displacement Contours .....	37
3.3.3 Comparison of Experimental and Finite Element Surface Strain Data.....	39
3.3.3.1 $\epsilon_x$ strain data .....	40
3.3.3.2 $\epsilon_y$ strain data .....	43
3.3.3.3 $\gamma_{xy}$ strain data .....	46
3.3.4 Finite Element Strain Results Near the Surface and Mid-Plane of the Plate .....	49
3.3.4.1 In-Plane Strains.....	49
3.3.4.2 Out-of-Plane Strains.....	55
3.3.5 Stress Results Near the Plate Surface.....	61

<b>Chapter 4: Induced Strain of Actuation in a Flat Plate With an Embedded Piezoceramic Patch</b> .....	<b>67</b>
4.1 Moiré Interferometry Experiment .....	67
4.1.1 Specimen Geometry, Construction, and Materials .....	67
4.1.2 Test Set-up and Experimental Procedure .....	68
4.2 Finite Element Modeling.....	70
4.2.1 The Finite Element Model .....	70
4.2.2 Finite Element Analysis.....	72
4.3 Results and Comparisons .....	72
4.3.1 Moiré Fringe Pattern Results .....	72
4.3.2 Comparison of Moiré Fringe Patterns to Finite Element Displacement Contours .....	74
4.3.3 Comparison of Experimental and Finite Element Surface Strain Data.....	76
4.3.3.1 $\epsilon_x$ strain data .....	76
4.3.3.2 $\epsilon_y$ strain data .....	79
4.3.3.3 $\gamma_{xy}$ strain data .....	82
4.3.4 Finite Element Strain Results Near the Surface and Mid-Plane of the Plate .....	85
4.3.4.1 In-Plane Strains.....	85
4.3.4.2 Out-of-Plane Strains.....	88
4.3.5 Stress Results Near the Specimen Mid-Plane.....	96

<b>Chapter 5: Conclusions and Recommendations .....</b>	<b>103</b>
5.1 Conclusions .....	103
5.2 Recommendations.....	105
<b>References .....</b>	<b>107</b>
<b>Vita .....</b>	<b>109</b>



## List of Illustrations

Figure 1: Schematic of a generalized moiré interferometry system. ....	10
Figure 2: Schematic of a generalized Twyman-Green interferometry system.....	10
Figure 3: Set-up of moiré interferometric test for piezoceramic in-plane voltage response. ....	14
Figure 4: Specimen grating replication technique for moiré interferometry. ....	17
Figure 5: Specialized specimen grating replication technique used to replicate a grating onto a fragile piezoceramic wafer. ....	17
Figure 6: Displacement fringe patterns for the u- and v-fields at 0 and 300 volts. ....	20
Figure 7: Experimental and published variations of $\epsilon_x$ with applied voltage for a free piezoceramic patch. ....	22
Figure 8: Experimental and published variations of $\epsilon_y$ with applied voltage for a free piezoceramic patch. ....	22
Figure 9: Set-up of the Twyman-Green interferometer for characterizing the out-of-plane voltage response of a free piezoceramic patch.....	24
Figure 10: Fringe pattern results from the Twyman-Green interferometry experiment for the characterization of out-of-plane voltage response. ....	26
Figure 11: Experimental and published variations of $\epsilon_z$ with applied voltage for a free piezoceramic patch. ....	27
Figure 12: Set-up of the moiré interferometric test conducted on the PSM-5 epoxy plate with surface bonded piezoceramic patches. ....	31
Figure 13: Finite element model grid views; undeformed and deformed. ....	34
Figure 14: U- and v-field fringe pattern results from the moiré interferometry experiment conducted on the surface bonded piezoceramic patch specimen. ....	36

Figure 15: Comparison of a moiré interferometric fringe pattern (u-field, 300 volts) and finite element displacement contours (u-field, -0.000560 patch free strain). .....	38
Figure 16: Variation of $\epsilon_x$ on the surface of the plate along the line $y = 0.5147$ inches. ....	41
Figure 17: Variation of $\epsilon_x$ on the surface of the plate along the line $y = 0.6432$ inches. ....	41
Figure 18: Variation of $\epsilon_x$ on the surface of the plate along the line $y = 0.9486$ inches. ....	42
Figure 19: Variation of $\epsilon_x$ on the surface of the plate along the line $y = 1.3500$ inches. ....	42
Figure 20: Variation of $\epsilon_y$ on the surface of the plate along the line $y = 0.5147$ inches. ....	44
Figure 21: Variation of $\epsilon_y$ on the surface of the plate along the line $y = 0.6432$ inches. ....	44
Figure 22: Variation of $\epsilon_y$ on the surface of the plate along the line $y = 0.9486$ inches. ....	45
Figure 23: Variation of $\epsilon_y$ on the surface of the plate along the line $y = 1.3500$ inches. ....	45
Figure 24: Variation of $\gamma_{xy}$ on the surface of the plate along the line $y = 0.5147$ inches. ....	47
Figure 25: Variation of $\gamma_{xy}$ on the surface of the plate along the line $y = 0.6432$ inches. ....	47
Figure 26: Variation of $\gamma_{xy}$ on the surface of the plate along the line $y = 0.9486$ inches. ....	48
Figure 27: Variation of $\gamma_{xy}$ on the surface of the plate along the line $y = 1.3500$ inches. ....	48

Figure 28: Variation of $\epsilon_x$ on the plane of Gauss points nearest the plate surface of the surface bonded piezoceramic patch specimen. ....	50
Figure 29: Variation of $\epsilon_x$ on the plane of Gauss points nearest the plate mid-plane of the surface bonded piezoceramic patch specimen. ....	51
Figure 30: Variation of $\gamma_{xy}$ on the plane of Gauss points nearest the plate surface of the surface bonded piezoceramic patch specimen. ....	53
Figure 31: Variation of $\gamma_{xy}$ on the plane of Gauss points nearest the plate mid-plane of the surface bonded piezoceramic patch specimen. ....	54
Figure 32: Variation of $\epsilon_z$ on the plane of Gauss points nearest the plate surface of the surface bonded piezoceramic patch specimen. ....	56
Figure 33: Variation of $\epsilon_z$ on the plane of Gauss points nearest the plate mid-plane of the surface bonded piezoceramic patch specimen. ....	57
Figure 34: Variation of $\gamma_{xz}$ on the plane of Gauss points nearest the plate surface of the surface bonded piezoceramic patch specimen. ....	59
Figure 35: Variation of $\gamma_{xz}$ on the plane of Gauss points nearest the plate mid-plane of the surface bonded piezoceramic patch specimen. ....	60
Figure 36: Variation of $\sigma_x$ on the plane of Gauss points nearest the plate surface of the surface bonded piezoceramic patch specimen. ....	62
Figure 37: Variation of $\sigma_z$ on the plane of Gauss points nearest the plate surface of the surface bonded piezoceramic patch specimen. ....	63
Figure 38: Variation of $\tau_{xy}$ on the plane of Gauss points nearest the plate surface of the surface bonded piezoceramic patch specimen. ....	64
Figure 39: Variation of $\tau_{xz}$ on the plane of Gauss points nearest the plate surface of the surface bonded piezoceramic patch specimen. ....	65
Figure 40: Set-up of the moiré interferometric test conducted on the PC-10C epoxy plate with an embedded piezoceramic patch. ....	69
Figure 41: Finite element model grid views; undeformed and deformed. ....	71

Figure 42: U- and v-field fringe pattern results from the moiré interferometry experiment conducted on the embedded piezoceramic patch specimen. ....	73
Figure 43: Comparison of a moiré interferometric fringe pattern (u-field, 343 volts) and finite element displacement contours (x-displacements, -0.000639 in-plane patch free strain). ....	75
Figure 44: Variation of $\epsilon_x$ on the surface of the plate along the line $y = 0.0451$ inches. ....	77
Figure 45: Variation of $\epsilon_x$ on the surface of the plate along the line $y = 0.2595$ inches. ....	77
Figure 46: Variation of $\epsilon_x$ on the surface of the plate along the line $y = 0.5248$ inches. ....	78
Figure 47: Variation of $\epsilon_x$ on the surface of the plate along the line $y = 0.7824$ inches. ....	78
Figure 48: Variation of $\epsilon_y$ on the surface of the plate along the line $y = 0.0451$ inches. ....	80
Figure 49: Variation of $\epsilon_y$ on the surface of the plate along the line $y = 0.2595$ inches. ....	80
Figure 50: Variation of $\epsilon_y$ on the surface of the plate along the line $y = 0.5248$ inches. ....	81
Figure 51: Variation of $\epsilon_y$ on the surface of the plate along the line $y = 0.7824$ inches. ....	81
Figure 52: Variation of $\gamma_{xy}$ on the surface of the plate along the line $y = 0.0451$ inches. ....	83
Figure 53: Variation of $\gamma_{xy}$ on the surface of the plate along the line $y = 0.2595$ inches. ....	83
Figure 54: Variation of $\gamma_{xy}$ on the surface of the plate along the line $y = 0.5248$ inches. ....	84

Figure 55: Variation of $\gamma_{xy}$ on the surface of the plate along the line $y = 0.7824$ inches. ....	84
Figure 56: Variation of $\epsilon_x$ on the plane of Gauss points nearest the plate surface of the embedded piezoceramic patch specimen. ....	86
Figure 57: Variation of $\epsilon_x$ on the plane of Gauss points nearest the plate mid-plane of the embedded piezoceramic patch specimen. ....	87
Figure 58: Variation of $\gamma_{xy}$ on the plane of Gauss points nearest the plate surface of the embedded piezoceramic patch specimen. ....	89
Figure 59: Variation of $\gamma_{xy}$ on the plane of Gauss points nearest the plate mid-plane of the embedded piezoceramic patch specimen. ....	90
Figure 60: Variation of $\epsilon_z$ on the plane of Gauss points nearest the plate surface of the embedded piezoceramic patch specimen. ....	91
Figure 61: Variation of $\epsilon_z$ on the plane of Gauss points nearest the plate mid-plane of the embedded piezoceramic patch specimen. ....	92
Figure 62: Variation of $\gamma_{xz}$ on the plane of Gauss points nearest the plate surface of the embedded piezoceramic patch specimen. ....	94
Figure 63: Variation of $\gamma_{xz}$ on the plane of Gauss points nearest the plate mid-plane of the embedded piezoceramic patch specimen. ....	95
Figure 64: Variation of $\sigma_x$ on the plane of Gauss points nearest the plate mid-plane of the embedded piezoceramic patch specimen. ....	97
Figure 65: Variation of $\sigma_z$ on the plane of Gauss points nearest the plate mid-plane of the embedded piezoceramic patch specimen. ....	98
Figure 66: Variation of $\tau_{xy}$ on the plane of Gauss points nearest the plate mid-plane of the embedded piezoceramic patch specimen. ....	99
Figure 67: Variation of $\tau_{xz}$ on the plane of Gauss points nearest the plate mid-plane of the embedded piezoceramic patch specimen. ....	100

## **List of Tables**

Table 1: Free piezoceramic patch in-plane voltage/strain response . . . . .	23
Table 2: Free piezoceramic patch out-of-plane voltage/strain response . . . . .	28
Table 3: Material properties of PSM-5 epoxy, PC-10C epoxy, and G-1195 piezoceramic . . . . .	30

# **Chapter 1: Introduction and Review of Literature**

## **1.1 Overview of Intelligent Material Systems and Research Focus**

### **1.1.1 Intelligent Material Systems: Definitions and Examples**

The definition of intelligent materials or material systems is rather subjective. Takagi (1990) defines intelligent materials as "materials which respond to environmental changes at the most optimum conditions and manifest their own functions according to the changes." He further divides the "intelligence" of a material into three basic categories, the intelligence at the most primitive levels in materials, intelligence inherent in materials, and intelligence from the viewpoint of human beings. The primitive intelligence of a material involves the nature of its functional ability as a sensor, actuator, and/or processor. The intelligence inherent in a material consists of the utilization of the primitive functions to accomplish a macroscopic goal such as environmental response, self-diagnosis, self-repair, and others. The intelligence of a material from the human viewpoint includes considerations of reliability, life span, economy, and environmental friendliness.

Wada, Fanson, and Crawley (1990) define an intelligent material in a different, but still subjective, manner. They first define an "adaptive" structure as one that is capable of altering its characteristics or state through controlling inputs to actuators. They also define a "sensory" structure as one that can monitor the state and characteristics of a structure through a sensor network. The overlapping of the sensory function and the adaptive function results in a "controlled" structure. Finally, the

intelligent structure is a subset of the controlled structure that has highly integrated sensory and actuator control.

In spite of the subjective nature of the definition of intelligent materials and structures, there is clear value in considering the use of these materials in the design process. The concept of controlling crack propagation and fatigue damage with induced strain actuators was presented by Rogers, Liang, and Li (1991). They proposed using a sensing material to characterize a load state and through a controlling computer cause actuators to respond and reduce the stress levels in critical areas. The potential for buckling control of stiffened panels was examined by Mollenhauer, Thompson, and Griffin (1992). A commercially available finite element program was used to evaluate the effects of embedded actuating materials on the buckling response of stiffened panels. Hickman, Gerardi, and Feng (1990) examined the use of actuating and sensing materials in the monitoring of aircraft health. The actuating materials were used to induce a specified vibration into the aircraft, while the sensors monitored the resulting vibrations and noted any differences over time. Changes in the vibrational characteristics over time were shown to be useful in determining the start of rivet line failures, fatigue cracks, and wing leading edge icing.

Other concepts for intelligent material systems include the vibration suppression of large space-based interferometers (Sirlin and Laskin, 1990). In the space structure discussed, the optical path lengths of certain elements must be maintained to within a 5 nanometer range, over separation lengths as large as 26 meters. The active suppression of sound reflection and transmission was examined by Braga, et al (1990) and Anders, Rogers, and Fuller (1991). Obvious applications of this sound suppression concept include the use of such technologies on submarine hulls. In contrast to these high frequency applications, Lazarus, Crawley, and Bohlmann (1990) examined the



applications of actuating materials to static aeroelastic control over wing camber and twist. Results indicate that in certain cases these adaptive wings would improve upon the performance exhibited by conventional flap and aileron designs.

### **1.1.2 Actuator and Sensor Material Candidates**

Many materials exhibit characteristics that allow for their use as either a sensor material, an actuator material, or both. These materials include, but are not limited to, optical glass fibers, shape memory alloys (SMA), electrostrictive materials, magnetostrictive materials, and piezoelectric materials. Optical glass fibers, when embedded in a composite structure, can be used as sensors. Possible applications include structural health monitoring and vibration sensing on space structures (Dehart and Griffin, 1990). Shape memory alloys can be used as both sensors and actuators, although they are generally used more in the role of actuators. Their use as an actuation material is due to the ability to recover large plastic deformations with the application of heat, usually through electric resistance. Specific applications of SMA include crack propagation control (Rogers, Liang, and Li, 1991), static aeroelastic control (Lazarus, Crawley, and Bohlmann, 1990), and sound suppression (Anders, Rogers, and Fuller 1991), as alluded to above. Electrostrictive and magnetostrictive materials exhibit nonlinear deformation upon exposure to an electric field and a magnetic field, respectively, and have been examined as candidates for actuating materials (Rogers, Liang, and Li, 1991).

Aside from SMAs, the majority of actuation materials examined in the literature has been the family of piezoelectric materials. A piezoelectric material has the ability to deform under the influence of an electric field or produce an electric charge when mechanically deformed. This near linear behavior can be exploited equally well as an

actuator or a sensor. The unique properties of a piezoelectric material is a result of a phenomenon called spontaneous polarization (Piezo Systems,1990). This is the process where the shifting of the electron clouds around individual atoms is accompanied by a shifting of positive ions relative to negative ions within a crystal lattice. Thus a net change in dimensions of the piezoelectric is accompanied by a change in the electric field. At this time, only small strains of the order of 0.1% are possible, but the bandwidth of usable frequencies is quite large. Piezoelectrics, and specifically piezoceramics, can be used at frequency ranges from static actuation to 10,000 Hz (Lazarus, Crawley,and Bohlmann, 1990). Specific applications of piezoelectric materials include fatigue damage control (Rogers, Liang, and Li, 1991), static aeroelastic control (Lazarus, Crawley, and Bohlmann, 1990), and aircraft health monitoring (Hickman, Gerardi, and Feng, 1990), among others.

### **1.1.3 Focus of Research**

The objective of using an actuating material is to induce a beneficial change in the state of the host structure. With piezoelectric materials, usually manufactured as thin wafers or patches, this is accomplished by bonding the material to the structure surface or embedding the piezoelectric material within the structure itself. The actuation occurs when a voltage is applied across the patch, causing the patch to strain relative to the adjacent material, thus inducing a strain in the adjacent structure itself. To properly design an intelligent structure, the strain induced into a host structure must be quantified. Several methods of analysis, detailed in the following sections of this chapter, have been considered by the research community.

The goal of this project was to examine the induced strain of piezoceramic patches, both surface bonded and embedded, using numerical and experimental

techniques, and to evaluate the usefulness of these techniques as applied to this research. The free response to an electric field of a lead zirconate titanate (PZT) piezoceramic was evaluated using moiré interferometry and Twyman-Green interferometry. Three-dimensional finite element models of two piezoceramic patch configurations were constructed using the information from these experiments. Concurrently, experiments were conducted on specimens of identical geometry to those modeled with the finite element method (FEM). The results of the numerical analyses were compared with the experimental data for verification of the numerical technique as applied to these models.

The model configurations chosen for this study include a surface bonded configuration and an embedded configuration. The surface bonded specimen consisted of a 2.87 inch square, 0.125 inch thick plate with 0.94 inch square piezoceramic patches bonded to the middle top and bottom surfaces. The embedded specimen consisted of a 2.43 by 2.36 inch rectangular, 0.1 inch thick plate with a 1.03 by 0.87 inch patch embedded at the mid-plane. Both plates were made of epoxy-based plastics while the thickness of all patches was 0.0095 inches. The large stiffness dominance of the PZTs over that of the plates was chosen so that the induced strains would be relatively large. This allowed for a more accurate experimental measurement of the induced strains through moiré interferometry.

## **1.2 Analysis Techniques Applied to Piezoceramic Based Hybrid Structures**

### **1.2.1 Analysis Techniques Examined by the Research Community**

Research into quantifying the induced strain of a surface bonded or embedded piezoceramic wafer has included a wide variety of analysis techniques. These include strain-energy methods, classical laminated plate theory, and finite element methods. Crawley and de Luis (1987) developed a one-dimensional strain-energy solution based

on the assumption of Bernoulli-Euler type strains and perfect bonding. This model was later refined (Crawley and Anderson, 1990) to include finite bond lines and a comparison with finite element solutions and experiments. It was found that the Bernoulli-Euler model adequately predicted extensional and bending strains for thin beams but significant differences occurred for thicker beams when compared to finite element solutions.

Wang and Rogers (1991a) developed an approach to the problem of quantifying the induced strain of actuation using classical laminated plate theory (CLPT). Using the CLPT approach, they were able to determine the equivalent forces and moments caused by piezoceramic patch actuation on two-dimensional laminated plates. Later a strain-energy model for beams was also developed to predict the equivalent forces and moments induced by finite-sized, spatially-distributed strain actuators (Wang and Rogers 1991b). With this model, the CLPT analysis technique developed earlier was refined.

Rogers, Liang, and Li (1991) used a commercially available finite element package to study the induced strain of actuation for use in evaluating active damage control. Two-dimensional models were constructed for structures with shape memory alloy actuators and for structures with piezoceramic actuators. The actuating materials were constructed with elements that had non-zero coefficients of thermal expansion (CTE), while the remainder of the structure was built with zero CTE elements. Actuation occurred by applying a temperature change to the model. The amount of strain applied was varied by manipulating the amount of temperature change or the value of the non-zero CTE.

A finite element formulation for composite materials containing piezoceramic actuators was developed by Ha, Keilers, and Chang (1990). The model was based on the theory of elasticity and Maxwell's equations and is capable of static and dynamic

analyses. The development resulted in a near-standard finite element formulation of the following form.

$$[M]\{\ddot{u}\} + [C]\{\dot{u}\} + [K]\{u\} = \{F_M\} + \{F_E\} \quad (1)$$

Where  $M$ ,  $C$ , and  $K$  represent the mass, damping, and stiffness matrices, respectively, while  $u$ ,  $\dot{u}$ , and  $\ddot{u}$  represent the nodal displacements, nodal velocities, and nodal accelerations, respectively.  $F_M$  and  $F_E$  represent the mechanical and electrical force vectors. The advantage of this finite element formulation over the simpler model described previously is that this model includes the electrical forcing vector in addition to the mechanical forcing vector. This allows the model to predict the electrical response of the piezoceramic patches to a mechanical load as well as the structural response to the actuation of the piezoceramic patches. The authors demonstrated that the model was useful in simulating the response to a controlling algorithm of a structure with actuators and sensors.

### **1.2.2 Analysis Techniques Used in This Study**

The two piezoceramic patch configurations chosen for this research were analyzed in a manner similar to that presented in Rogers, Liang, and Li (1991), described above. Three-dimensional finite element models were constructed and analyzed using commercially available software packages on the Apollo DN10000 computer in the Department of Engineering Science and Mechanics at Virginia Polytechnic Institute and State University (VPI&SU). Pre- and post-processing was accomplished using PATRAN (version 2.4), a product of the PATRAN Division of PDA Engineering located in Costa Mesa, California. The analyses were performed using ABAQUS (version 4.8), produced by Hibbitt, Karlsson, & Sorensen, Inc. of Providence, Rhode Island. Patch actuation was

accomplished by specifying a 1 degree ( $^{\circ}\text{C}$  or  $^{\circ}\text{F}$ ) temperature change for the models and choosing an appropriate value of CTE for the patch elements. The values chosen for the CTE of the patch elements corresponds to the strain experienced by a free patch when exposed to the desired voltage. The voltage/strain response of the piezoceramic patches was determined using the experiments described in the next section and detailed in chapter 2.

An important consideration in any finite element analysis is the mesh density. With thin plate structures, the mesh density through the thickness is also quite important. Vidussoni and Griffin (1990) concluded that for a laminated plate, two 20-node brick elements through the thickness of a given lamina was necessary to properly model out-of-plane effects. MacNeal and Harder (1988) demonstrated in a series of finite element test problems that the 20-node brick element with reduced order integration performed better in most cases than the 20-node brick element with the full 27 Gauss-point integration. The models constructed for the study presented herein used two 20-node brick elements through the thickness of a given layer (piezoceramic or plate material). These elements, designated within ABAQUS as C3D20R, are standard isoparametric serendipity elements with reduced order integration.

## **1.3 Experimental Techniques Used in This Research**

### **1.3.1 Experiments Performed**

Four distinct experiments were conducted during the course of this research. Two experiments were performed to characterize the in-plane and out-of-plane displacement and strain response of a free piezoceramic patch to an applied voltage. These experiments included a moiré interferometric experiment to quantify in-plane

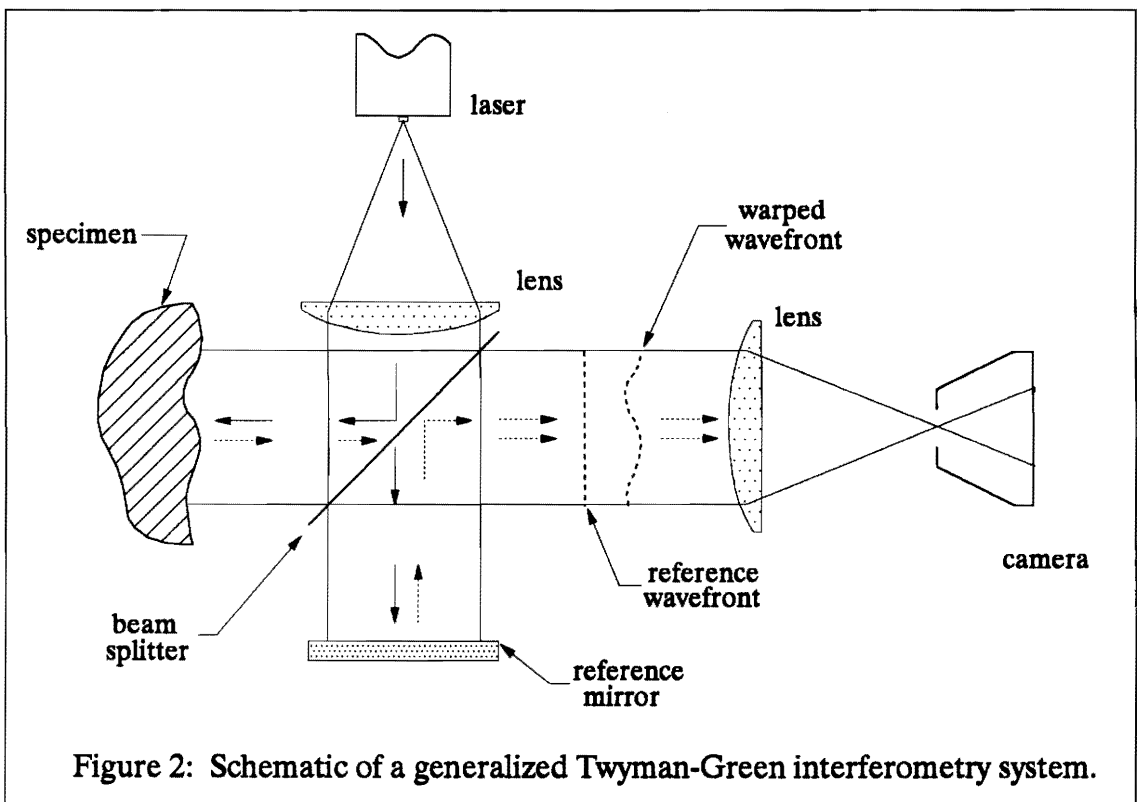
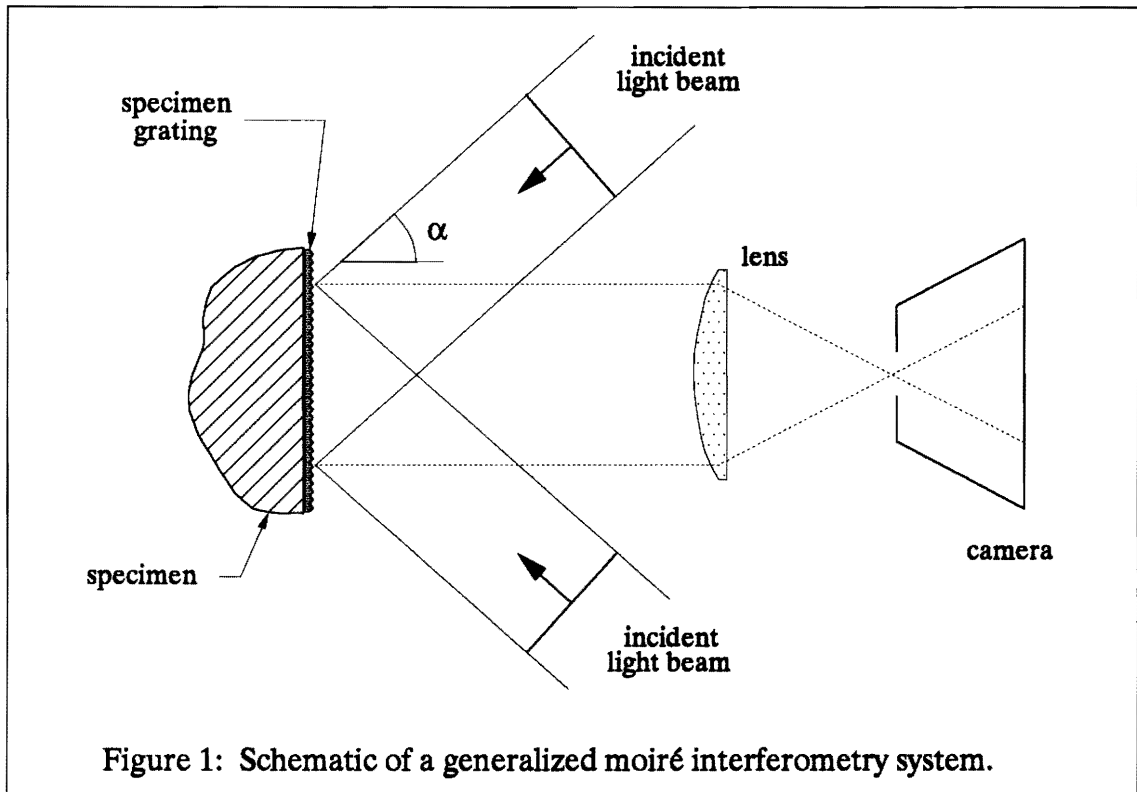
responses and a Twyman-Green interferometric experiment to characterize the out-of-plane response. Two other moiré interferometric experiments were performed on the two patch/plate configurations described above. Both of these experiments examined the induced strain response of the plate to the actuation of the piezoceramic. In-plane surface displacements in the vicinities of the patches were recorded.

### 1.3.2 Moiré Interferometry

Moiré interferometry is a whole-field technique to determine in-plane displacements and strains (Post, 1987, 1989). A high frequency, cross-line, phase-type grating is applied to the specimen. The grating is illuminated by two coherent beams of light intersecting at an angle,  $\alpha$ , as shown in Figure 1. The intersecting beams create a virtual, reference grating of constructive and destructive interference with a frequency of  $f$ . These incident beams diffract from the specimen and form an interference pattern that is proportional to in-plane displacements and is photographically recorded as a fringe pattern. A fringe is simply the locus of all points experiencing the same displacement in a given direction with respect to some reference point. Considering  $u$  and  $v$  as the  $x$ -displacement and  $y$ -displacement components, respectively,  $u$  and  $v$  are computed from the fringe data as follows.

$$u = \left(\frac{1}{f}\right)N_x \quad v = \left(\frac{1}{f}\right)N_y \quad (2)$$

Where  $N_x$  and  $N_y$  represent the fringe orders at the point of interest obtained from the  $x$ -displacement and  $y$ -displacement fringe patterns, respectively, and  $f$  is the reference





grating frequency. At a point, the linear strains are

$$\epsilon_x = \frac{\delta u}{\delta x} \quad \epsilon_y = \frac{\delta v}{\delta y} \quad \gamma_{xy} = \frac{\delta u}{\delta y} + \frac{\delta v}{\delta x} \quad (3)$$

The reference grating frequency,  $f$ , is determined by the wavelength of the incident beams of light and the incidence angle,  $\alpha$ . It typically has a value of 60960 lines per inch (2400 lines per mm) which produces a value of 16.4  $\mu$ inches per fringe (0.417  $\mu$ m per fringe).

### 1.3.3 Twyman-Green Interferometry

A Twyman-Green interferometer is an optical apparatus designed to measure the surface topography (out-of-plane displacement) of an object using the interference between two beams of coherent light (Post 1980). Figure 2 is a schematic of a basic Twyman-Green interferometer. A coherent beam of light is split by an optically flat beam splitter with half of the beam being directed toward the sample and the other half toward an optically flat mirror. Both beams are then reflected back toward the beam splitter. The beam reflected from the specimen has warped wave fronts with warpage proportional to the surface topography of the specimen. The other beam has flat wave fronts and acts as a reference beam. Upon reaching the beam splitter again, the reference beam is split into two beams with one approaching the camera. The warped beam is also split into two beams with one beam approaching the camera as well. The combination of these two beams at the camera causes an interference pattern of dark and light fringes proportional to the surface topography of the specimen. The sensitivity of Twyman-Green interferometry is

$$w = N(\lambda/2) \quad (4)$$

Where  $w$  is the elevation of a given point relative to a reference point,  $N$  is the fringe order of the point of interest relative to a reference fringe, and  $\lambda$  is the wavelength of light being used. The wavelength of light used in this research was  $2.03 \times 10^{-5}$  inches (514nm) which gives a sensitivity of  $1.01 \times 10^{-5}$  inches (257nm) per fringe order.

## **Chapter 2: Free Piezoceramic Voltage Response Characterization**

### **2.1 In-plane Voltage Response Characterization**

#### **2.1.1 Set-up of Moiré Interferometry Experiment**

The set-up of the experiment to determine the in-plane voltage response of a free piezoceramic patch is presented in Figure 3. A cross-lined phase-type grating was replicated on the surface of the piezoceramic patch. The piezoceramic patch was then connected to a DC voltage supply and mounted on an adjustable mirror stand. The mounting was accomplished through the use of compliant foam posts constructed of several layers of double-stick foam-core tape. This allowed the deformation of the piezoceramic patch without significant restriction and also minimized vibrations that are detrimental to the experimental technique. The phase grating was illuminated by two incident coherent beams of light, and the fringe patterns were recorded by a camera. As pictured in Figure 3, the convergence of the incident light beams parallel to the x-z plane represent the optical configuration responsible for determining the x-displacements. The resulting fringe pattern is known as the u-field. When the incident beams converge parallel to the y-z plane, the y-displacement field is recorded as a fringe pattern known as the v-field.

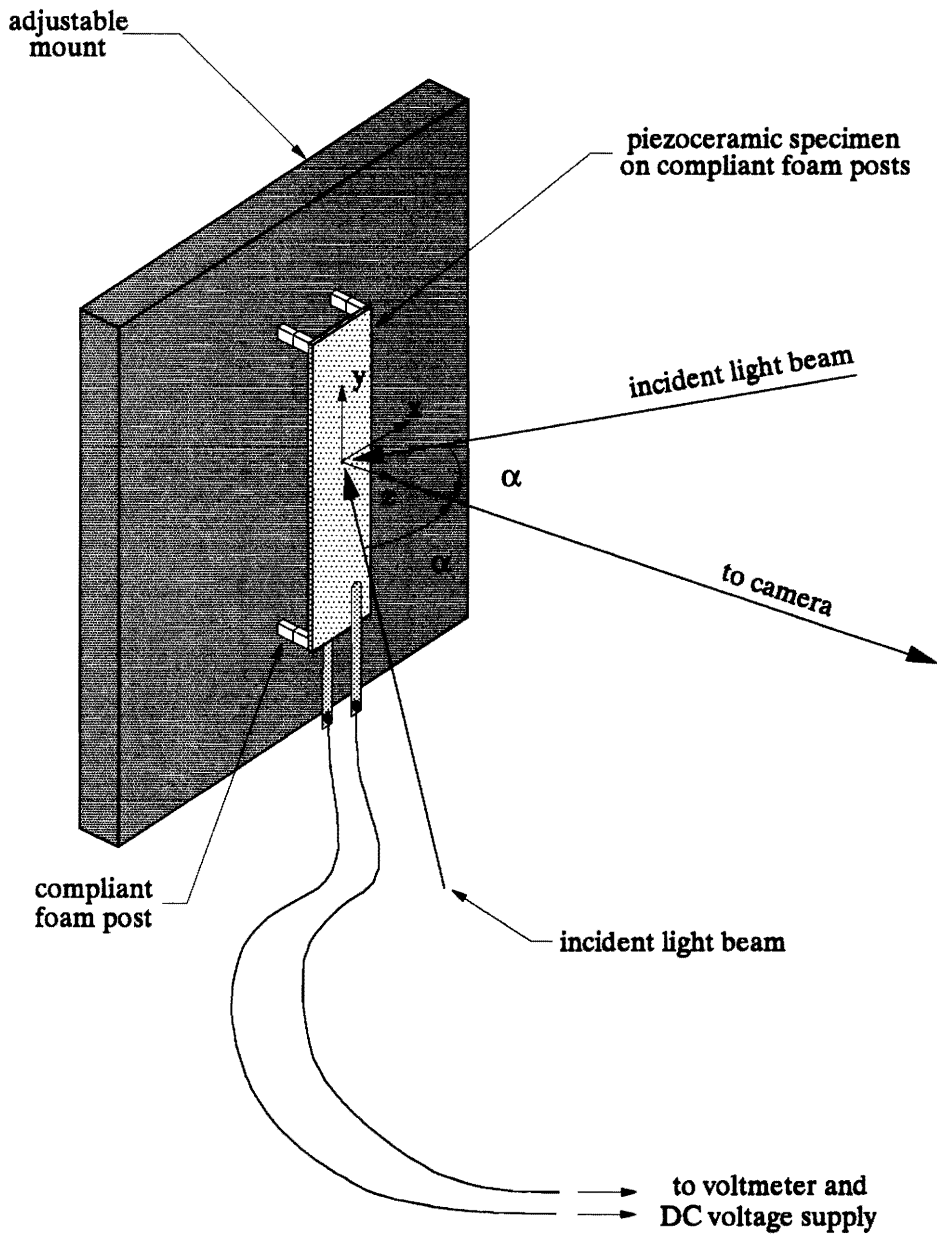


Figure 3: Set-up of moiré interferometric test for piezoceramic in-plane voltage response.

### **2.1.2 Specimen Construction and Grating Replication**

Two specimens were constructed for in-plane voltage response characterization. Both specimens were 0.5 inches wide and approximately 1.25 inches long. The patch material, provided by The Center for Intelligent Material Systems and Structures (CIMSS) at VPI&SU, was manufactured as 1.5 inch by 2.5 inch patches, 0.0095 inches thick. The manufacturer of the patches used throughout this research was Piezo Electric Products, Inc. of Metuchen, New Jersey. These piezoceramic materials, designated as G1195 or Navy Type-II, were all from the same lot number, 5/15/91. The brittle, non-conducting ceramic material is sputter coated on each side with a film of nickel. The nickel acts to distribute the applied charge over the surface of the piezoceramic patch as well as providing a surface to which electrical leads are soldered.

The piezoceramic patches were cut using a sharp razor blade to score the surface of the patch. Repeated passes with the razor blade resulted in the semi-controlled breakage of the patch along the desired line. The cut was rarely clean and required delicate sanding to smooth the edge. The electrical leads consisted of narrow strips, approximately 0.1 inches wide, of 0.001 inch thick brass shim material. These strips were sanded with 600 grit sandpaper to further reduce their thickness. Surface preparation for soldering consisted of burnishing the surface of the nickel coated patch with a pencil eraser and degreasing with acetone. A very small amount of low temperature solder and an acid flux was used to silver the surface in preparation for attaching the brass shim material. The leads were soldered on with the excess solder being pushed out from under the shim and removed. The thinness of the electrical leads resulted in minimal interference with the performance of the piezoceramic patch.

Moiré interferometry requires a diffraction grating to be present on the surface of the specimen of interest. Usually this diffraction grating is "replicated" onto the surface as presented in Figure 4. The standard process involves several steps. First, the grating mold is coated with a release agent. A layer of aluminum a few angstroms thick is then vapor deposited on the grating surface. The mold is then bonded onto the specimen with a low shrinkage adhesive, often epoxy. A weight is used to apply an even pressure during curing. As the adhesive cures, the edges are cleaned with a swab to remove excess adhesive, allowing more adhesive to ooze from under the mold. Cleaning results in a thin grating, less than 0.001 inches thick, with sharply defined edges. After the adhesive is allowed to cure, the mold is separated from the specimen, leaving the metallic film behind.

The separation of the mold from the specimen usually requires quite a bit of force. Due to the fragile nature of the piezoceramic patches and the 0.0095 inch thickness, a special replication technique was employed as shown schematically in Figure 5. The piezoceramic patch was prepared by first cutting and sanding it to the same size as a steel gage block, 0.5 by 1.25 inches. Then the brass electrical leads were soldered near the bottom of the patch. The replication process began by bonding the piezoceramic patch to the steel gage block using a paper-based double-stick tape. The piezoceramic/gage block assembly was then treated as a standard specimen, the gage block providing support for the patch, preventing breakage during separation. After separation, the gage block was removed by carefully dissolving the double-stick tape adhesive with a solvent. The paper base of the double-stick tape wicked the solvent deep into the joint between the gage block and the piezoceramic patch. Care was taken to avoid contaminating the face of the grating with dissolved tape adhesive. In spite of the careful nature of this replication technique, the two patches examined in this research

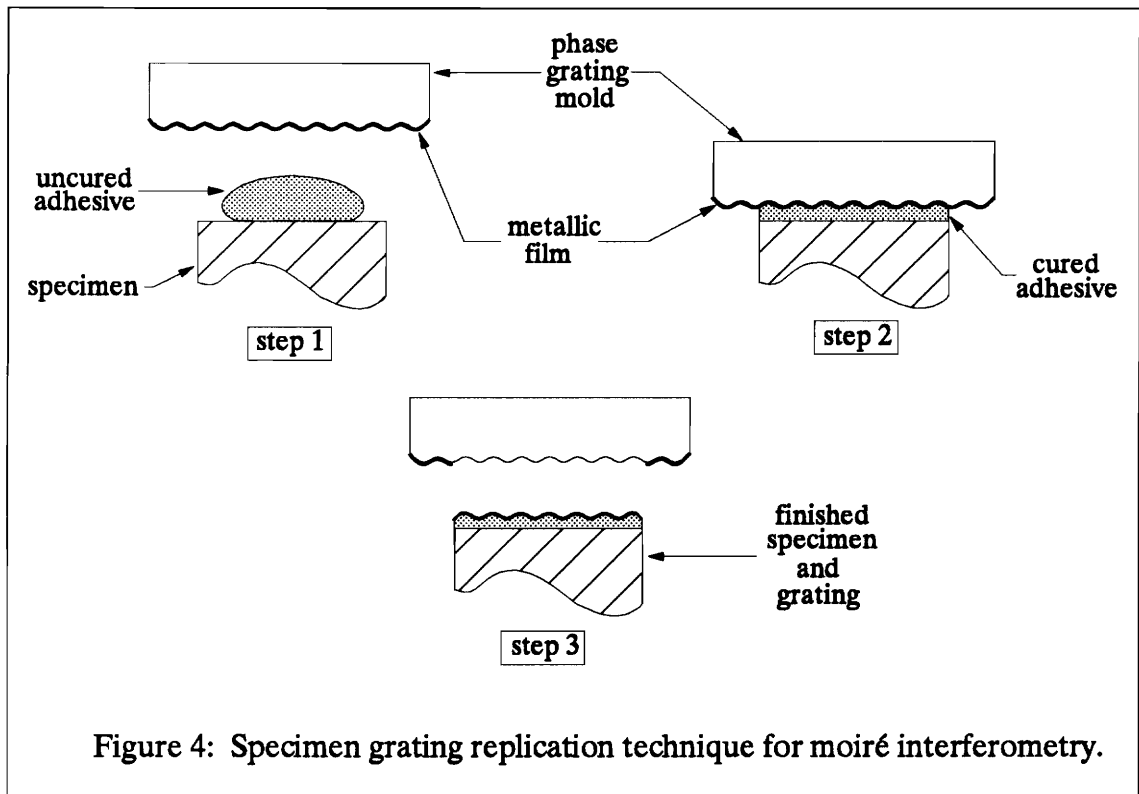


Figure 4: Specimen grating replication technique for moiré interferometry.

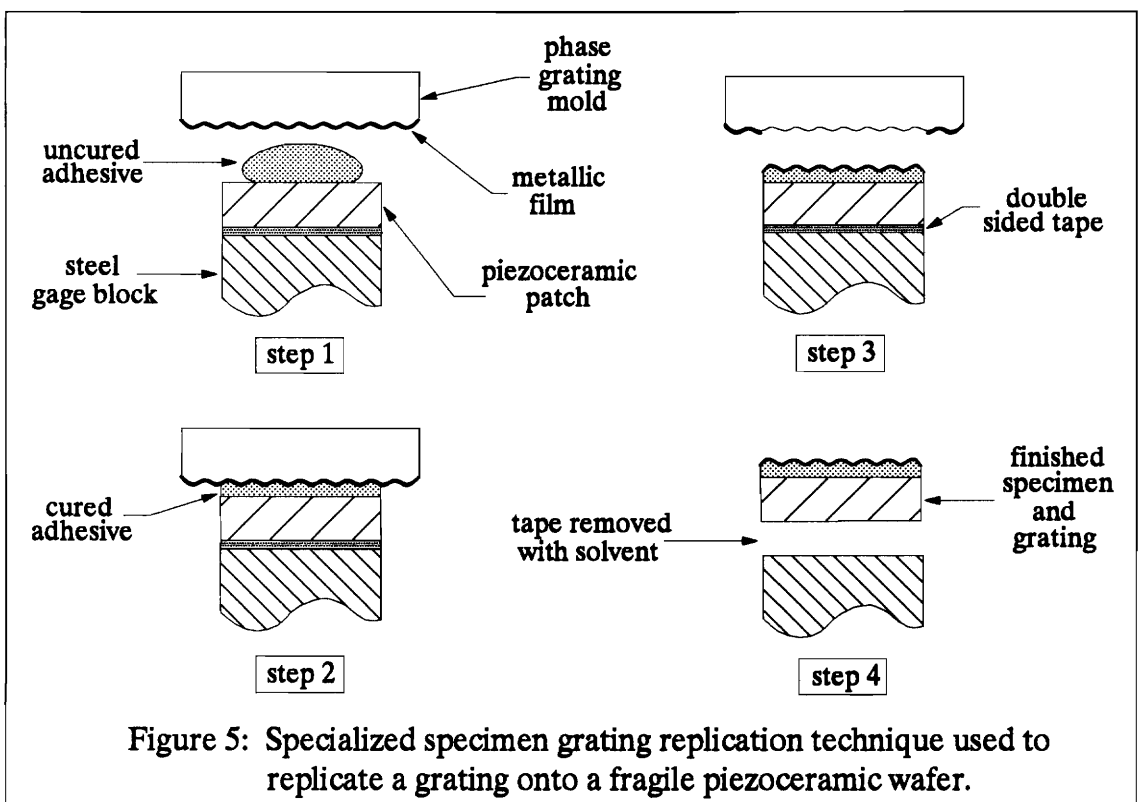


Figure 5: Specialized specimen grating replication technique used to replicate a grating onto a fragile piezoceramic wafer.

broke during the removal of the gage block. Both of the breaks occurred at a corner near the bottom edge and did not present a problem as far as the moiré testing was concerned, although the electrical lead on one of the patches was attached to one of these broken corners and had to be reattached.

### 2.1.3 Testing and Results

The first patch examined was tested at 100, 150, 200, 250, 300, and 343 volts. The DC voltage supply had a maximum capability of 343 volts. The second patch examined was tested at 300 and 343 volts. The electric field strength is often reported instead of the applied voltage. In this particular study, the electric field strengths examined were 10.52, 15.78, 21.05, 26.32, 31.57, and 36.11 volts/mil. These correspond with the applied voltages divided by the patch thickness, in this case, 9.5 mil. The voltages were applied in the direction of the initial poling of the piezoceramic patch. Poling of the ceramic part of the patch occurs during manufacturing by applying a large voltage across the patch to align the crystalline structure for optimum piezoelectric response. By applying voltage with the same sign as the poling voltage, the patch will be less likely to depole, a phenomenon that can spontaneously occur with piezoceramic patches and will occur if a large voltage is applied opposite to the poling voltage. When a patch depoles, the optimum piezoelectric response is lost. The in-plane strain is compressive when the applied voltage is in the same direction as the poling voltage and tensile when the applied voltage is of opposite sign from the poling voltage.

To find the total in-plane strain at a point, it is necessary to consult both the u- and v-field fringe patterns. The u-field yields  $\delta u/\delta x$  and  $\delta u/\delta y$ , while the v-field yields  $\delta v/\delta x$  and  $\delta v/\delta y$ . If, for example,  $\delta u/\delta x$  is desired at a point, the displacements at two points horizontally spanning the point of interest are determined. The difference between



these displacements is divided by the distance by which they are separated, yielding an average strain over the selected area which can be assumed to exist at the point of interest.

Selected fringe patterns from both tests are presented in Figure 6. The fringe patterns in Figure 6a&b are the 0-volt and 300-volt u- and v-field fringe patterns from the first test. The determination of voltage-induced strain for a given voltage, say 300 volts, is accomplished by first calculating the strain at a given point for both the 0- and 300-volt patterns using the method described above. The true 300-volt induced strain is the difference of the 300-volt and 0-volt strains calculated from the respective fringe patterns. Ideally, the fringe pattern for the 0-volt case (called a null field) should contain no fringes. This assumes that the grating mold is perfect and the replication process does not induce any residual strains into the specimen. In the case of the piezoceramic patches tested, the replication process is responsible for the residual strains in the specimen, or more correctly, the grating itself. As manufactured, the piezoceramic patches tested were not completely flat, but when bonded to the steel gage block, they were forced flat. When separation and removal of the gage block occurred, the patches returned to their initial shape, inducing a residual strain in the specimen grating. This strain had no effect on the testing, except for the difficulty in the analysis caused by the large number of fringes in the null field fringe patterns.

A method to eliminate the tedious nature of analyzing the initial pattern and subtracting the results from the loaded patterns is detailed in Post (1987) and was applied to the second free patch experiment. This technique involves applying a carrier pattern to the initial and loaded fringe patterns. A carrier pattern is simply a change in the fringe pattern due to a change in the frequency or direction of the virtual reference grating through the manipulation of the optical elements in the moiré interferometry experiment

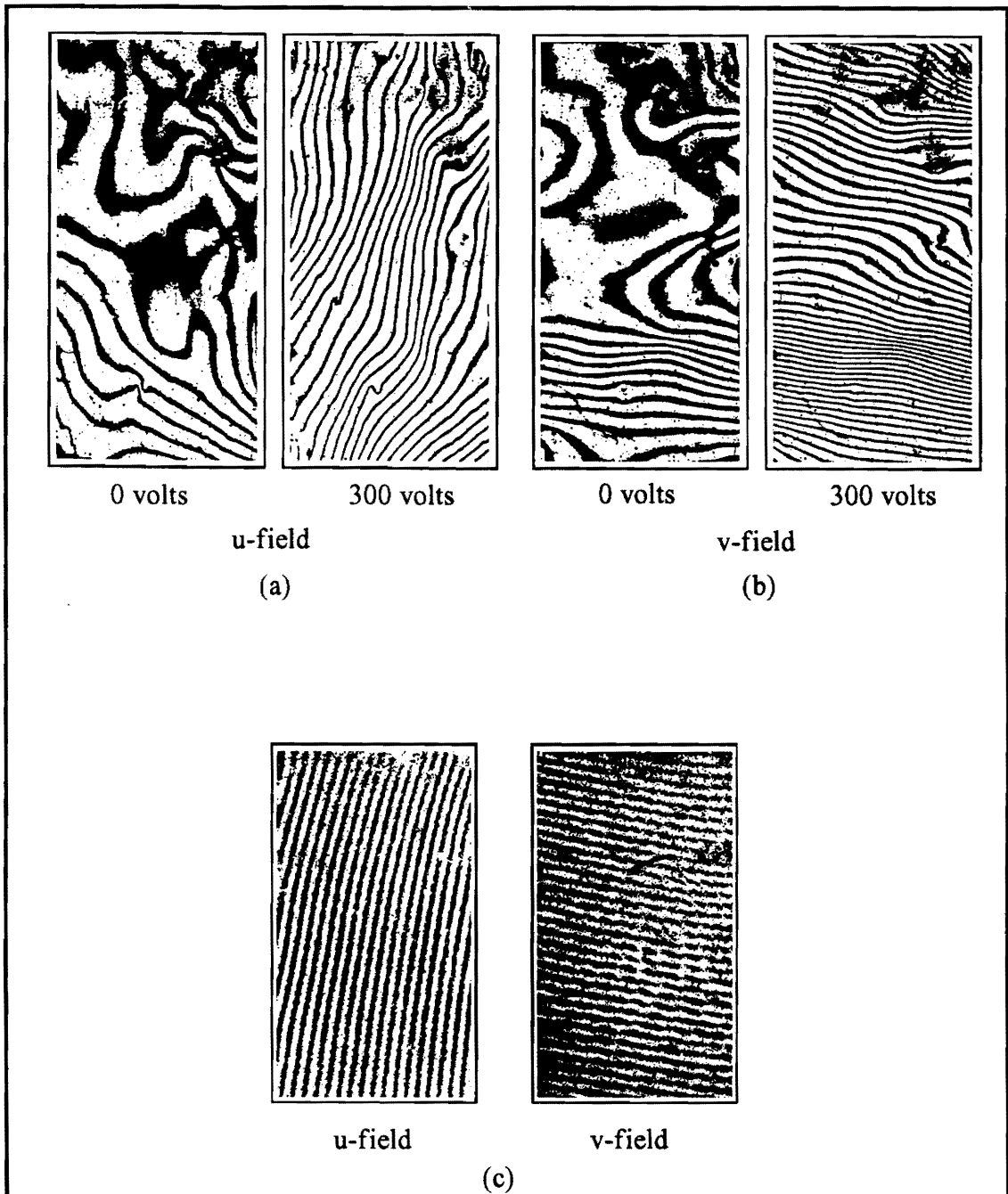


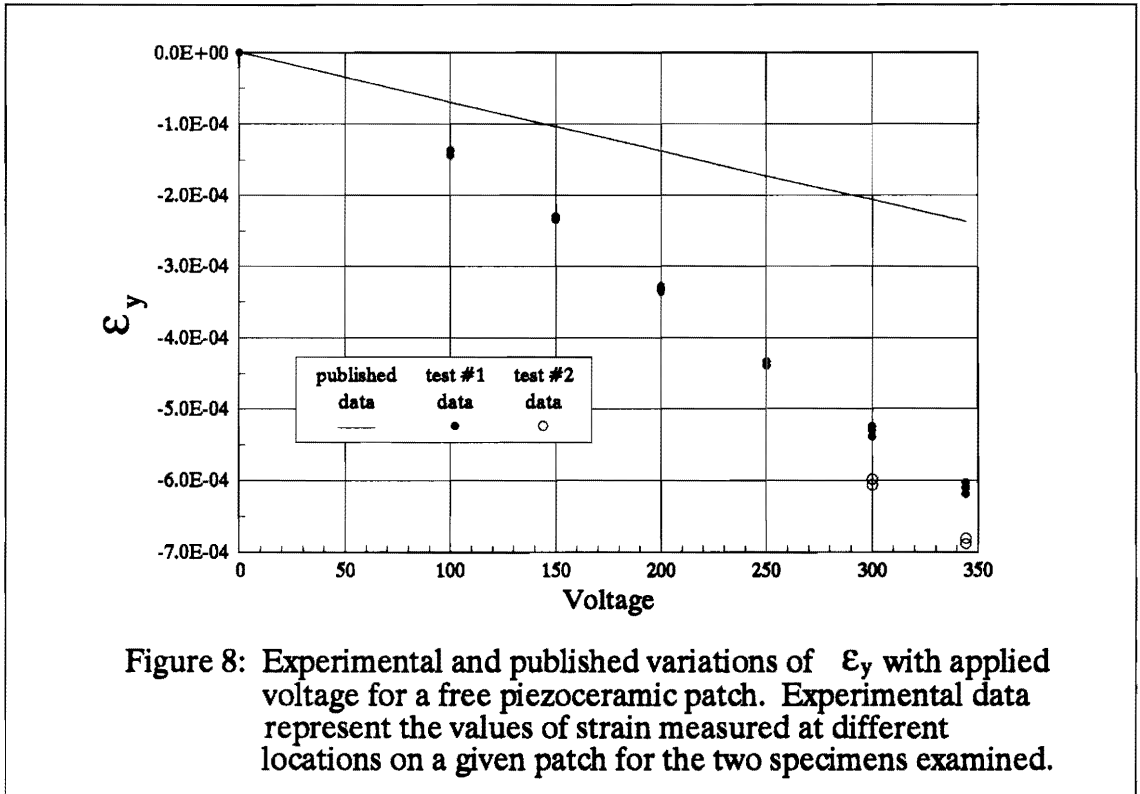
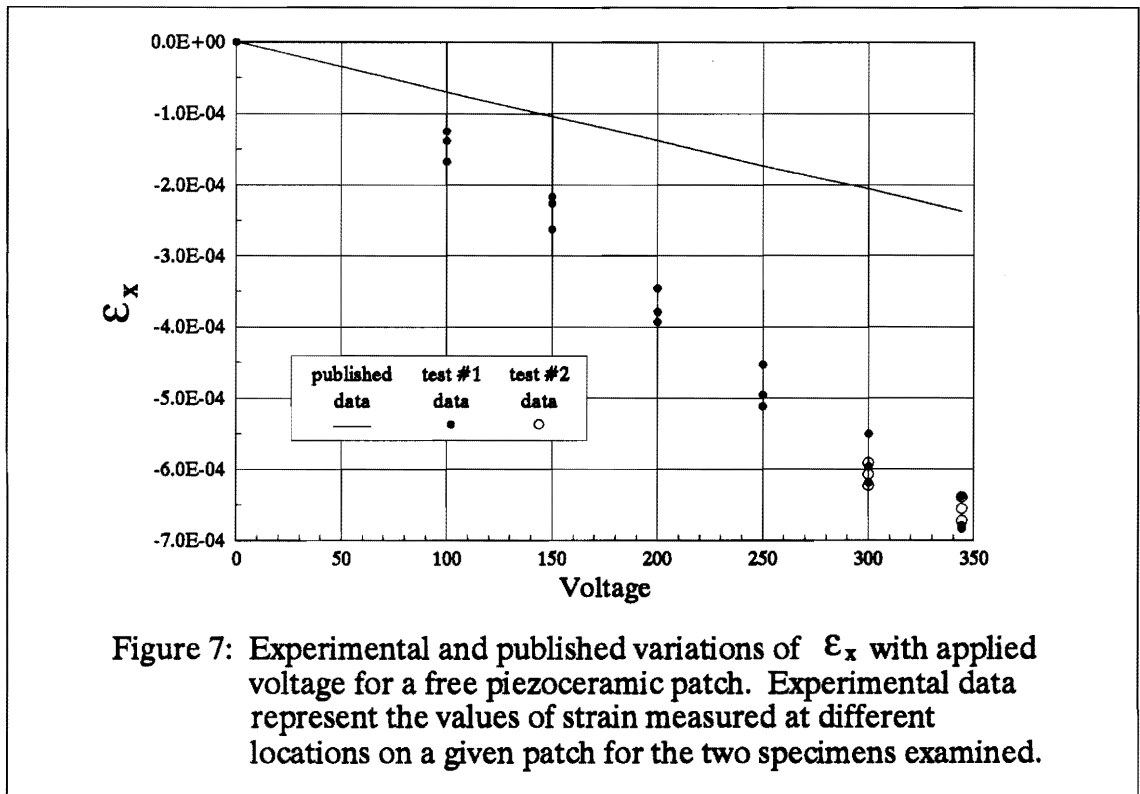
Figure 6: Displacement fringe patterns for the u- and v-fields at 0 and 300 volts. (a) and (b) are the initial and activated patterns requiring analysis and subtraction to yield proper values for 300 volt strain. (c) is the moiré-of-moiré fringe patterns obtained by superimposing the carrier-pattern-enhanced 0- and 300-volt fringe patterns.

(Guo, Post, and Czarnek 1989). The results of this manipulation can be the addition or subtraction of a small or large number of fringes representing either extensional displacements (caused by a change in reference grating frequency) or rotational displacements (caused by a rotation of the reference grating with respect to the specimen grating). After the carrier pattern was applied, the photographs for the initial, 0-volt patterns and subsequent higher voltage patterns were recorded. By superimposing the 0-volt film negative and, for example, the 300-volt film negative, the fringe pattern representing the difference in the two superimposed fringe patterns was produced. Although the contrast is not as good, the results, as indicated in Figure 6c, are much simpler to analyze than the previous method. In the case of the present study, a carrier of rotation of approximately 10 fringes per millimeter was applied by rotating the specimen about the z-axis. This "super-moiré" or "moiré-of-moiré" method has several benefits. The ease of analysis helps to eliminate the error prone nature of analyzing two complex patterns and subtracting to get the true strain. It also demonstrates the uniformity of the piezoceramic deformation across the face of the patch, a characteristic that would be difficult to evaluate from the initial and loaded fringe patterns individually.

The published in-plane voltage response of the patch material (Piezo Systems, 1991) is based on the following equation.

$$\epsilon_x = \epsilon_y = (V/T)d_{31} \quad (5)$$

Where V is the voltage, T is the patch thickness (0.0095 inches), and  $d_{31}$  is the in-plane piezoelectric charge coefficient ( $-6.535 \times 10^{-9}$  in/V). Published strain values are compared with the experimental values of  $\epsilon_x$  in Figure 7 and  $\epsilon_y$  in Figure 8. The data indicate a near linear response except at the lower voltages, but of a significantly higher magnitude than predicted. The average experimental values from all tests are compared with the



theoretical data in Table 1. The average values of in-plane free patch strain were later used in the finite element analyses of the surface bonded and embedded patch models.

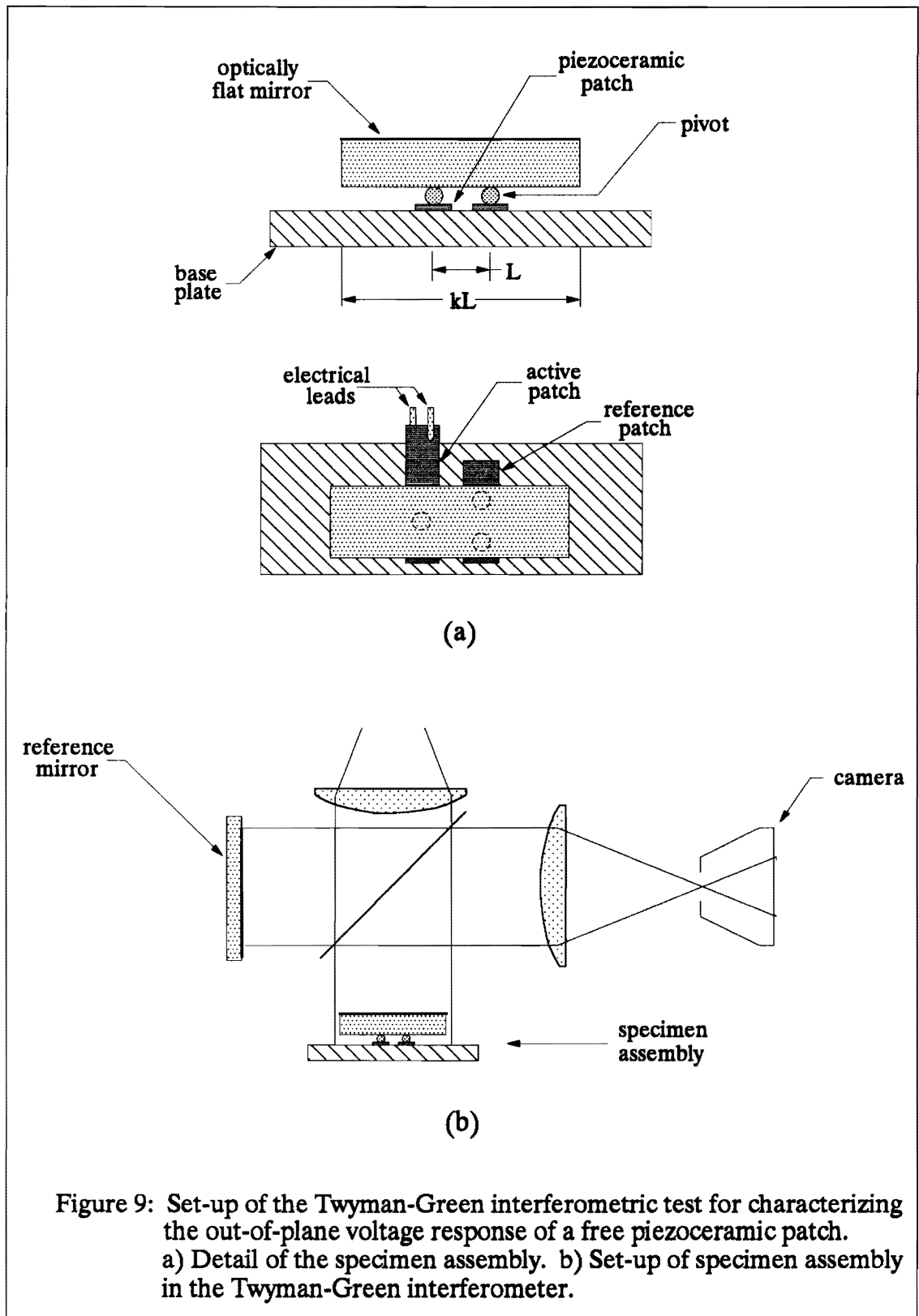
Table 1: Free piezoceramic patch in-plane voltage/strain response

Voltage	Average $\epsilon_x$ or $\epsilon_y$	$\epsilon_x$ or $\epsilon_y$
	Experimental	Published
100	-0.000142	-0.000070
150	-0.000233	-0.000104
200	-0.000352	-0.000138
250	-0.000462	-0.000173
300	-0.000560	-0.000206
343	-0.000639	-0.000237

## 2.2 Out-of-plane Voltage Response Characterization

### 2.2.1 Set-up of Twyman-Green Interferometry Experiment

The configuration of the Twyman-Green interferometric experiment is detailed in Figure 9. Upon examining the published data on the out-of-plane voltage response of a piezoceramic patch, it was found that the maximum deformations would be on the order of one wavelength of light. This would result in poor accuracy since the basic Twyman-Green interferometer has a sensitivity of half a wavelength of light per fringe. To increase the magnitude of the deformation, a specimen assembly as presented in Figure 9a was developed. With this assembly, an optically flat mirror with pivot points a known



distance apart was placed on top of two piezoceramic patches. One patch was active, while the other served only to level the mirror with respect to the interferometer. The mirror, also of a known length, amplified the deformation by 'k' times. The specimen assembly was then placed in the Twyman-Green interferometer as detailed in Figure 9b. In this experiment, the mirror length to pivot length ratio, k, was 8.47 with the mirror length being 2.5 inches.

### 2.2.2 Testing and Results

One piezoceramic patch was tested at 100, 200, 300, and 343 volts. The resulting fringe pattern progression is presented in Figure 10. The initial tuning of the interferometer was such that the active mirror pictured in Figure 9 had a slightly positive elevation difference from end to end. This alleviated any ambiguity in the sign of the subsequently induced out-of-plane expansions. The displacement results were evaluated in a manner similar to the first moiré experiment described above. The w-displacement for all patterns was determined by using equation 4 to calculate the apparent thickness change for all cases and then subtracting the initial, 0-volt value from the non-zero voltage results. The out-of-plane normal strain,  $\epsilon_z$ , was then calculated by dividing the actual thickness change by the original thickness. These results are plotted with respect to the published values in Figure 11 and presented in Table 2. The experimental data again indicate a much larger response than predicted with the published data. The published out-of-plane voltage response is based on the following equation.

$$\epsilon_z = w/T = (V/T)d_{33} \quad (6)$$

V is the voltage, T is the original patch thickness, and  $d_{33}$  is the published out-of-plane piezoelectric charge coefficient of  $14.170 \times 10^{-9}$  in/V. The experimental out-of-plane free



0 Volts



100 Volts



200 Volts



300 Volts



343 Volts

Figure 10: Fringe pattern results from the Twyman-Green interferometry experiment for characterization of out-of-plane voltage response (progression from 0 to 343 volts).



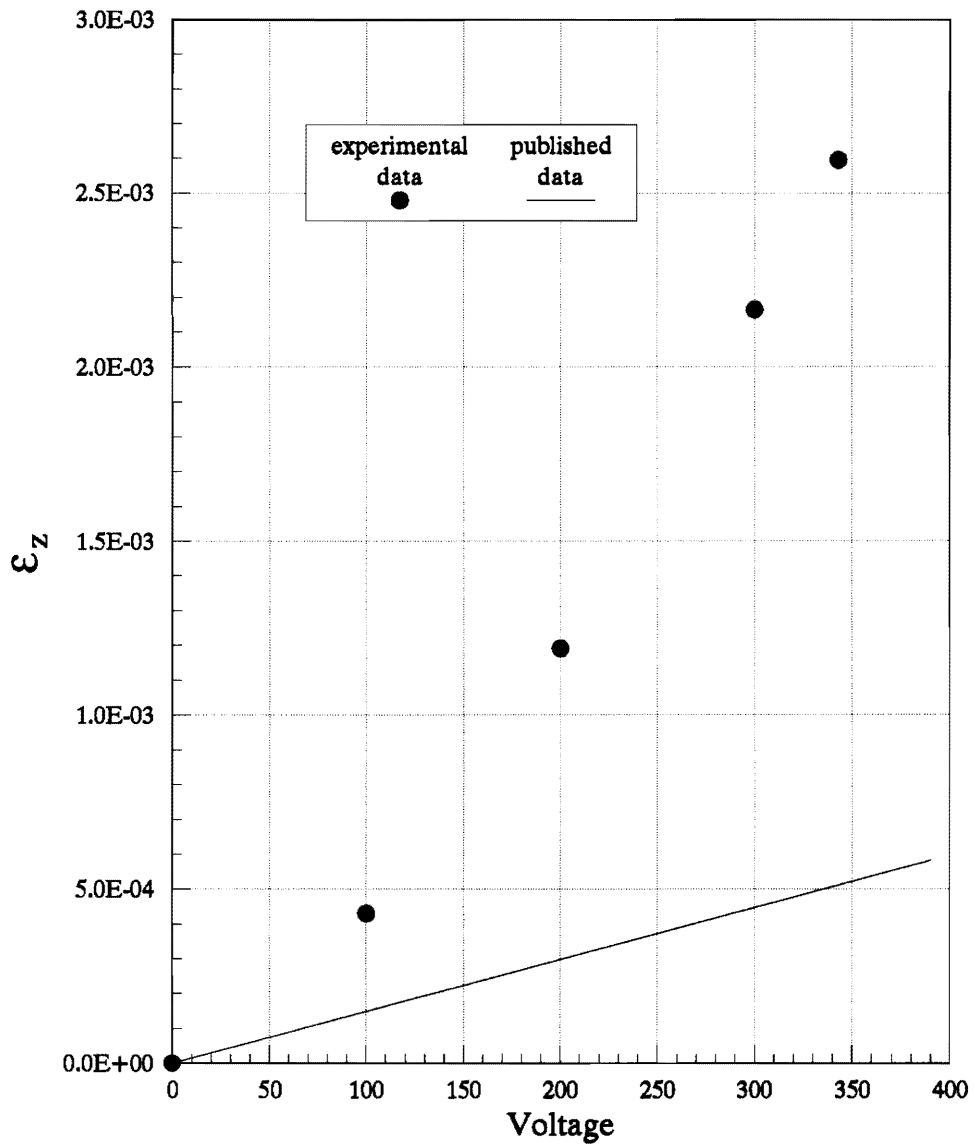


Figure 11: Experimental and published variations of  $\epsilon_z$  with applied voltage for a free piezoceramic patch.

patch strain data was later employed in the finite element analyses of the surface bonded and embedded patch models.

Table 2: Free piezoceramic patch out-of-plane voltage/strain response

<b>Voltage</b>	<b><math>\epsilon_z</math> Experimental</b>	<b><math>\epsilon_z</math> Published</b>
100	0.000430	0.000149
200	0.001190	0.000298
300	0.002165	0.000447
343	0.002595	0.000512

## **Chapter 3: Induced Strain of Actuation in a Flat Plate With Surface Bonded Piezoceramic Patches**

### **3.1 Moiré Interferometry Experiment**

#### **3.1.1 Specimen Geometry, Construction, and Materials**

The specimen examined in this experiment consisted of a plate, 2.87 inches square and 0.125 inches thick, cut from a sheet of PSM-5 epoxy generously provided by Prof. C. W. Smith of the Department of Engineering Science and Mechanics at VPI&SU. Piezoceramic patches, 0.94 inches square and provided by CIMSS, were bonded to the top and bottom center of the plate. The PSM-5 epoxy plate was saw cut to approximate size and then carefully sanded square. The desired dimensions of the plate and patch were 3 inches square and 1 inch square respectively, but by the time each was sanded to the proper square shape, the dimensions were slightly smaller. Thin strips of brass shim stock were soldered to the top and bottom surfaces of the patches to act as electrical leads. The patches were then bonded to the surface of the plate. A weight was placed on top of the patch while the adhesive cured, and care was taken to clean adhesive spew from around the patch edge. The adhesive used to bond the patches to the plate was PC-10C epoxy provided by Dr. D. Post, also of the Department of Engineering Science and Mechanics at VPI&SU. Both PSM-5 and PC-10C are products of the Photoelastic Division of Measurements Group/Vishay based in Raleigh, North Carolina. As a final step, a phase-type cross-line grating, suitable for moiré interferometry, was replicated over a rectangular area 2.49 by 0.94 inches, 0.02 inches from the top edge of the front patch. The material properties of PSM-5, PC-10C, and the G1195 piezoceramic patches

are presented in Table 3. The literature from the piezoceramic manufacturer provides only the in-plane and out-of-plane Young's moduli, while the piezoceramic in-plane Poisson's ratio was determined by Wang and Rogers (1991a). Although the published material indicates anisotropic behavior of the piezoceramic patches, this research considered the patches to behave isotropically. The stiffness of the plate material and the adhesive are the same, while the respective Poisson's ratios differ only slightly.

Table 3: Material properties of PSM-5 epoxy, PC-10C epoxy, and G1195 piezoceramic

<b>Material</b>	<b>Young's modulus</b>	<b>Poisson's Ratio</b>
PSM-5 epoxy	0.45 Msi	0.36
PC-10C epoxy	0.45 Msi	0.38
G1195 Piezoceramic	in-plane: 9.1 Msi out-of-plane: 7.1 Msi	in-plane: 0.28

### 3.1.2 Test Set-up and Experimental Procedure

The specimen described above was mounted to an adjustable mirror mount as shown in Figure 12. As with the free patch testing described in the previous chapter, the mounting was achieved through compliant foam posts constructed with multiple layers of double-stick foam-core tape. The piezoceramic patches were connected in parallel to a DC power supply and voltmeter in such a way that the applied voltage had the same sign as the poling voltage. The parallel connection guaranteed the same applied voltage for each patch. Due to limitations in the optical set-up and the inexperience of the author, the entire specimen diffraction grating was not illuminated. A 2.37 by 0.94 inch area

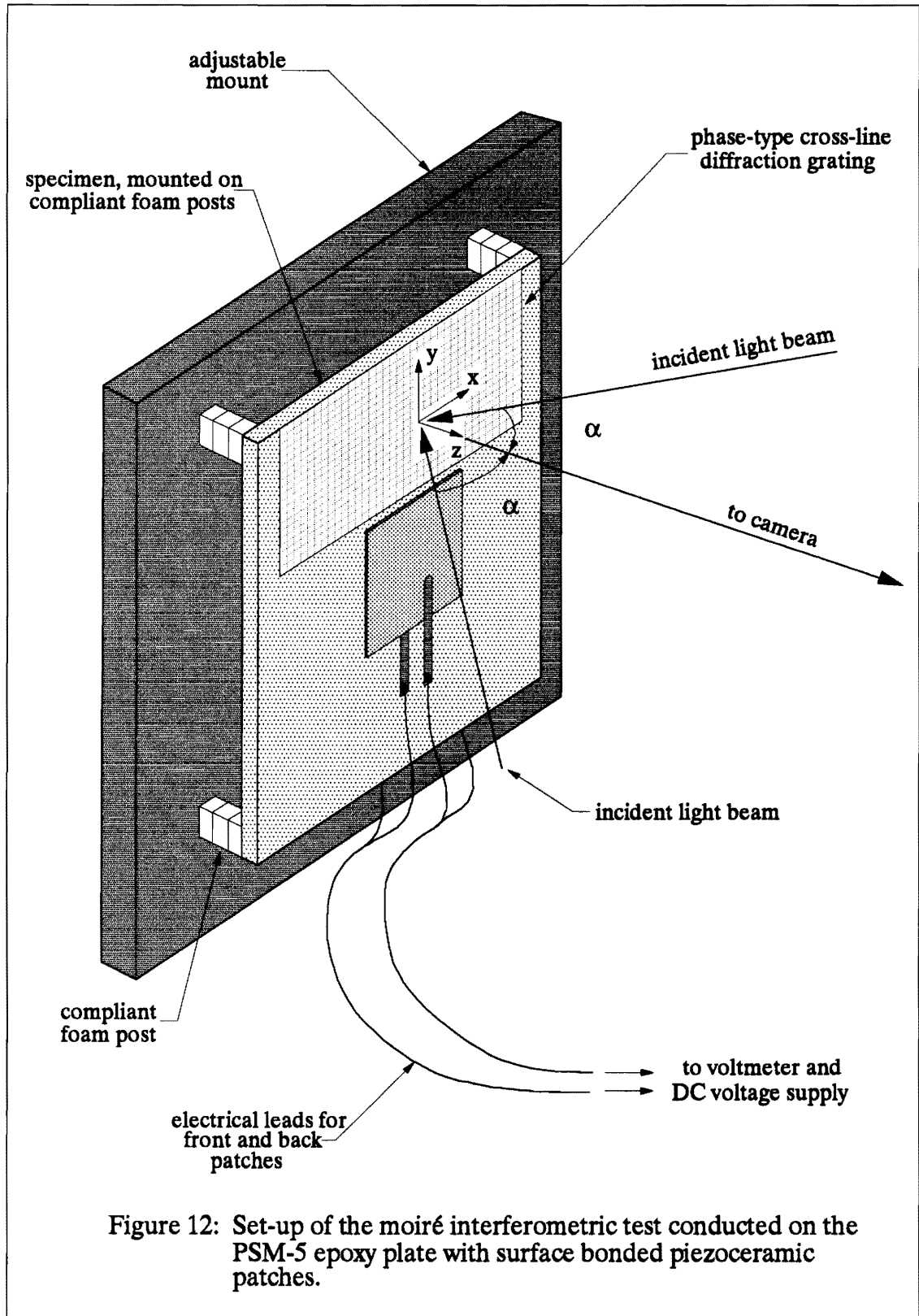


Figure 12: Set-up of the moiré interferometric test conducted on the PSM-5 epoxy plate with surface bonded piezoceramic patches.

was illuminated for the u-field set-up (pictured in Figure 12), while for the v-field set-up, a 1.47 by 0.94 inch area was illuminated.

The voltage levels proposed for testing were 100, 200, 300, and 343 volts. When voltage was applied to the piezoceramic patches for the first time, the patch bonded to the back of the plate shorted out. It is believed that a crack was induced in the patch when the electrical leads were attached. Solder evidently wicked into the crack, creating a path through which current could flow from the front face of the patch to the back face. This resulted in the inability of the patch to hold a charge. To solve this problem, the nickel coating was removed from around the exposed electrical lead. The lead was reattached to another portion of the patch and the patch was tested to see if it could hold a charge. The patch did not hold a charge, and more of the nickel coating was removed along the bottom edge of the patch. Eventually, the short was eliminated, but as a result, approximately the bottom 1/4 of the patch was rendered ineffective. The influence of this with respect to the test results are not known, but is believed to be minimal due to the location of the moiré grating on the top part of the opposite side of the plate.

The test was started again, and the proposed levels of voltage were examined. Due to the poor null field, it was decided to employ the moiré-of-moiré method again as described in the previous chapter. A carrier pattern of rotation of approximately 10 fringes per millimeter was applied to the specimen before the desired voltage levels were examined. The recorded fringe patterns (u- and v-fields) at 100, 200, 300, and 343 volts were then superimposed individually with the 0-volt fringe patterns to produce the true induced displacement fields.

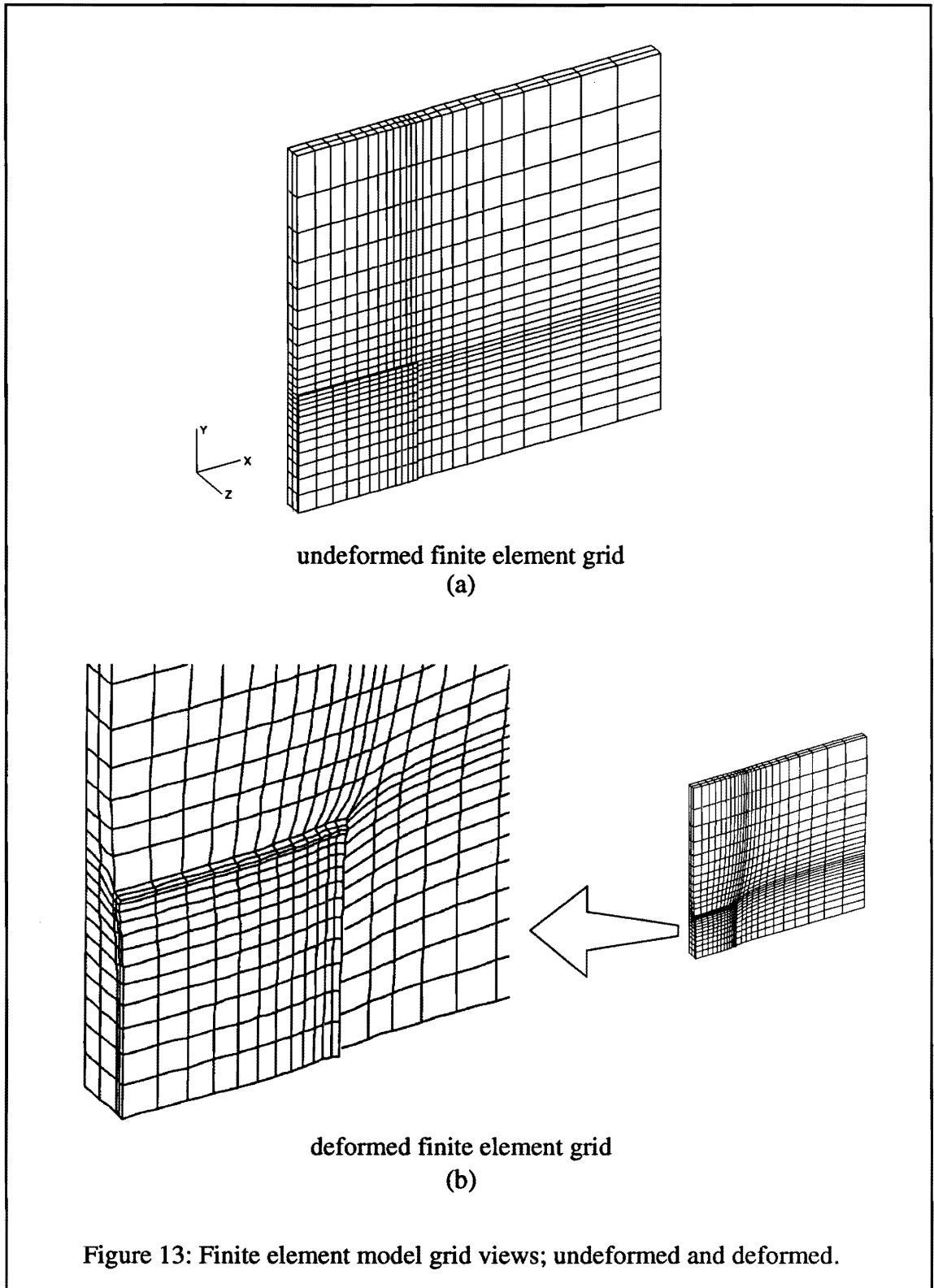
## **3.2 Finite Element Modeling**

### **3.2.1 The Finite Element Model**

Pre-processing of the finite element model for this research was accomplished using the finite element program PATRAN. The model was constructed of three-dimensional, 20-node brick elements designated as type C3D20R within ABAQUS, the program used to analyze the finite element model. These elements are standard isoparametric serendipity elements with reduced integration. The plate and patch were modeled using two elements through their respective thicknesses. A coordinate system was chosen with an origin at the center, mid-plane of the plate, with the x and y axes in the plane of the plate and parallel to its edges. The symmetric placement of the piezoceramic patches at the center of the top and bottom faces of the plate and the isotropic properties of the plate ensured that there would be no out-of-plane bending. Because of this and the fact that the structure was symmetric about the x and y axes, only one eighth of the structure was modeled. All displacements normal to their respective symmetry planes were specified to be zero. The resulting finite element grid is presented in Figure 13a. Note, however, that the coordinate system origin is displaced from the center, mid-plane of the plate for ease of viewing. The final model contained 8025 nodes and 1440 elements and matched the experimentally tested specimen geometry except for the omission of the adhesive bond line.

### **3.2.2 Finite Element Analysis**

A linear analysis of the above model was conducted using ABAQUS on the Apollo DN10000 computer in the Department of Engineering Science and Mechanics. The elements modeling the plate were specified to have a 0.45 Msi Young's modulus, a





0.36 Poisson's ratio, and a coefficient of thermal expansion (CTE) of 0.0, while the elements modeling the patch were specified to have a 9.1 Msi Young's modulus and a 0.28 Poisson's ratio. To actuate the patch, and match the ratio of thru-the-thickness expansion to in-plane contraction, the coefficient of thermal expansion for the patch elements was different for the in-plane and out-of-plane directions. These CTE values correspond with the in-plane and out-of-plane free patch strain data presented in the previous chapter. The in-plane coefficient of thermal expansion for the patch elements was defined to be  $-0.000560/\text{degree } (^{\circ}\text{C or } ^{\circ}\text{F})$  while the out-of-plane CTE was defined to be  $0.002165/\text{degree } (^{\circ}\text{C or } ^{\circ}\text{F})$ . The application of a one degree ( $^{\circ}\text{C or } ^{\circ}\text{F}$ ) temperature change to the model simulated the application of 300 volts to both the top and bottom patches in the real specimen. This analysis returned displacement data at the nodes and strain data at the Gaussian integration points.

### **3.3 Results and Comparisons**

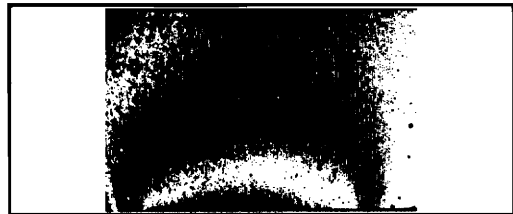
#### **3.3.1 Discussion of Moiré Fringe Pattern Results**

The u- and v-field fringe patterns recorded during the above testing are presented in Figure 14. In each fringe pattern, the patch was located just below the view spanning slightly more than the middle third of each picture. Note that the v-field illumination was not as extensive as that of the u-field. The smaller area of coverage affected the analysis of  $\epsilon_y$  and  $\gamma_{xy}$  as detailed in the following sections. Also note that the upper left part of the diffraction grating was damaged as indicated by the narrow, fringe-like mark at the upper left of the grating, extending along the top of the specimen. This feature, particularly visible in the first three u-field fringe patterns, did not affect the analysis.

Visible in Figure 14 is the lack of symmetry about the vertical axis of the recorded fringe patterns. The u-field patterns are slightly asymmetric with the fringes in



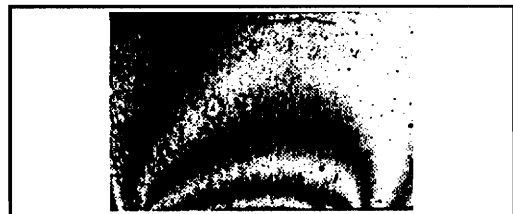
100 volts, U-field



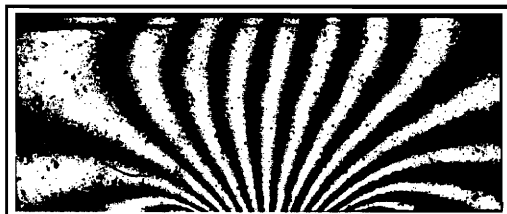
100 volts, V-field



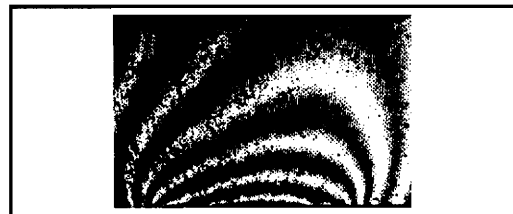
200 volts, U-field



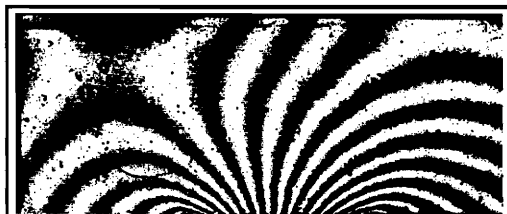
200 volts, V-field



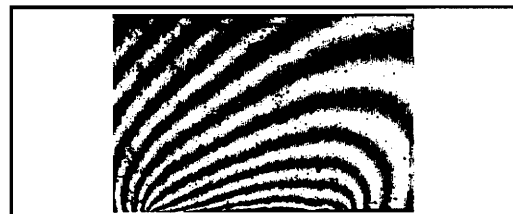
300 volts, U-field



300 volts, V-field



343 volts, U-field



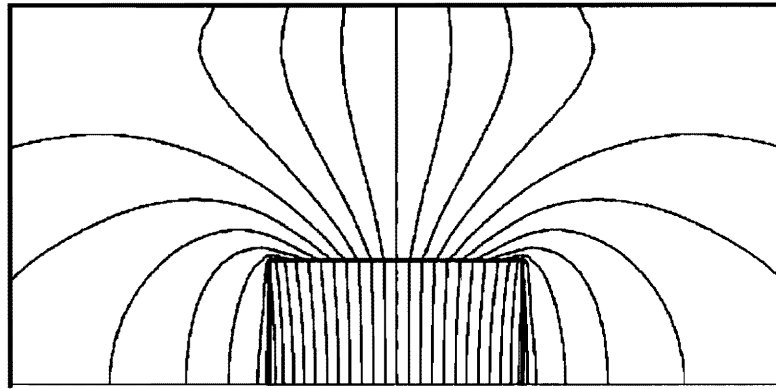
343 volts, V-field

Figure 14: U- and v-field fringe pattern results from the moiré interferometry experiment conducted on the surface bonded piezoceramic patch specimen. The top edge of the patch is centered below the bottom border of each picture.

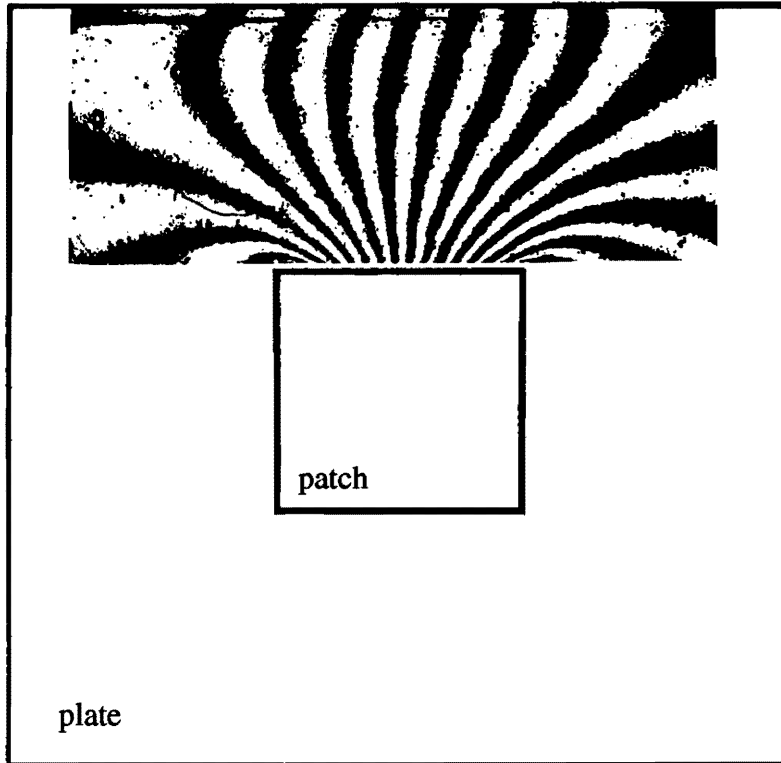
the vicinity of the patch having a tendency to slope more to the left of symmetry. Near the top of the plate, the u-field fringes slope more to the right of the symmetry plane. The v-field patterns show a more significant asymmetry, with the fringe density being larger on the left half of the specimen. A misalignment of the patches with respect to the plate edges is a possible contributor to the asymmetric behavior. Another possible cause of the asymmetric response is the fact that the back patch was only 3/4 active. The nickel coating was roughly removed across the bottom 1/4 of the patch, but not parallel to the bottom edge of the patch. Slightly more of the nickel coating was removed from the right side of the patch as viewed from the front.

### **3.3.2 Comparison of Moiré Fringe Patterns to Finite Element Displacement Contours**

The finite element deformed grid is pictured in Figure 13b with the deformations exaggerated. Another way to display the same information is with displacement contours. The x-displacement contours generated by PATRAN from nodal displacement data are displayed in Figure 15a. The fringes represent lines of constant x-displacement on the surface of the plate with respect to the origin. Note that this data has been mirrored about the y-axis for a clear comparison with the moiré fringe pattern presented in Figure 15b. The amount of x-displacement per contour was specified in PATRAN to be the same as the x-displacements per fringe order in moiré interferometry, 0.000016 inches per contour. One important point to note is that the displacements are all negative on the right side of the specimen and positive on the left side of the specimen. That is, the plate became smaller as a whole due to the patch shrinking within its plane. The two patterns are clearly quite similar. Across the top edge there are approximately 7 contours in the finite element results, while the moiré fringe pattern yields approximately 7.5 fringes.



finite element displacement contours  
(a)



moiré displacement fringe pattern  
(b)

Figure 15: Comparison of a moiré interferometric fringe pattern (u-field, 300 volts) and finite element displacement contours (x-displacement, -0.000560 in-plane patch free strain).

### 3.3.3 Comparison of Experimental and Finite Element Surface Strain Data

Experimentally and numerically obtained variations of  $\epsilon_x$ ,  $\epsilon_y$ , and  $\gamma_{xy}$  on the surface of the plate are examined in this section. Specifically, the strain variation was compared across four horizontal lines at various  $y$  locations. The experimental data was analyzed in the standard manner as described in the previous chapter. The only difference came about in the calculation of the shearing strains. Calculation of the individual shear strain components at specific points was necessary. These components were then added together to yield  $\gamma_{xy}$ . Usable data was gathered from the  $u$ -field fringe patterns over a range from approximately  $x = -1.1$  to  $x = 1.0$  inches. The usable range of  $v$ -field fringe pattern had the approximate boundaries of  $x = -0.6$  and  $x = 0.8$  inches. This smaller usable  $v$ -field range limited the calculation of the strains dependent on  $y$ -displacements, namely  $\epsilon_y$  and  $\gamma_{xy}$ . Note that the patch edges were located at  $x = \pm 0.47$  and  $y = \pm 0.47$  inches and the plate edges were located at  $x = \pm 1.435$  and  $y = \pm 1.435$  inches

Since the strains were desired on the surface of the plate, the finite element nodal displacement data was used to calculate strain in a manner analogous to the method used to calculate strain from the experimental data. In a finite element model, the strain data is returned most accurately at the Gauss points and is commonly extrapolated to the nodes. In order to eliminate potential errors due to extrapolation, a simple program was written to extract the strains along desired horizontal lines using the nodal displacement data. This program, when given the coordinates of a node, takes the displacement values ( $u$  and  $v$ ) of the four surrounding nodes and their respective coordinates and divides the proper displacement difference by the proper coordinate difference. In this way,  $\delta u/\delta x$ ,  $\delta v/\delta y$ ,  $\delta u/\delta y$ , and  $\delta v/\delta x$  and subsequently,  $\gamma_{xy}$ , can be calculated for any desired node.

Experimental and numerical strain data are presented in the following sections for the horizontal lines  $y = 0.5147$ ,  $0.6432$ ,  $0.9486$ , and  $1.3500$  inches. The choice of these values was made to examine the strain variations both near to and far from the patch edge. These lines of analysis were also chosen to correspond to the locations of lines of nodes across the finite element model.

### **3.3.3.1 $\epsilon_x$ strain data**

The experimentally and numerically obtained variations of  $\epsilon_x$  across the specimen, starting with  $y = 0.5147$  inches and ending with  $y = 1.3500$  inches are shown in Figures 16-19, respectively. In these figures, a schematic of the specimen with the respective line of analysis is sketched at the right, while the projected patch edge locations are plotted with the strain data. At  $y = 0.5147$  inches, the maximum compressive strain occurred at  $x = 0.0$  and was approximately  $-0.000290$ . This is approximately 52% of the applied in-plane patch free strain of  $-0.000560$ . The experimental data, although a bit erratic near the patch edge, match the numerical results fairly well. It is interesting to note that although the plate became smaller overall, the strain was not compressive everywhere. Within the projected limits of the patch edges,  $\epsilon_x$  is compressive. As the patch boundaries are approached, the strain increases rapidly and becomes positive just outside of these boundaries. Plate material outside of the patch boundaries resists the actuation of the patch by pulling against its contraction. The result is a tensile strain. This effect is less pronounced with increasing distance from the patch, as seen in Figures 17 and 18.  $\epsilon_x$  in Figure 19 never becomes tensile, but instead approaches zero near the plate edges. Along the lines  $y = 0.9486$  inches and  $y = 1.3500$  inches, the experimental strains are more compressive on the right side of the specimen than they are on the left. This is an indication of the asymmetry discussed previously and is likely due to a combination of patch misalignment and rear patch damage.

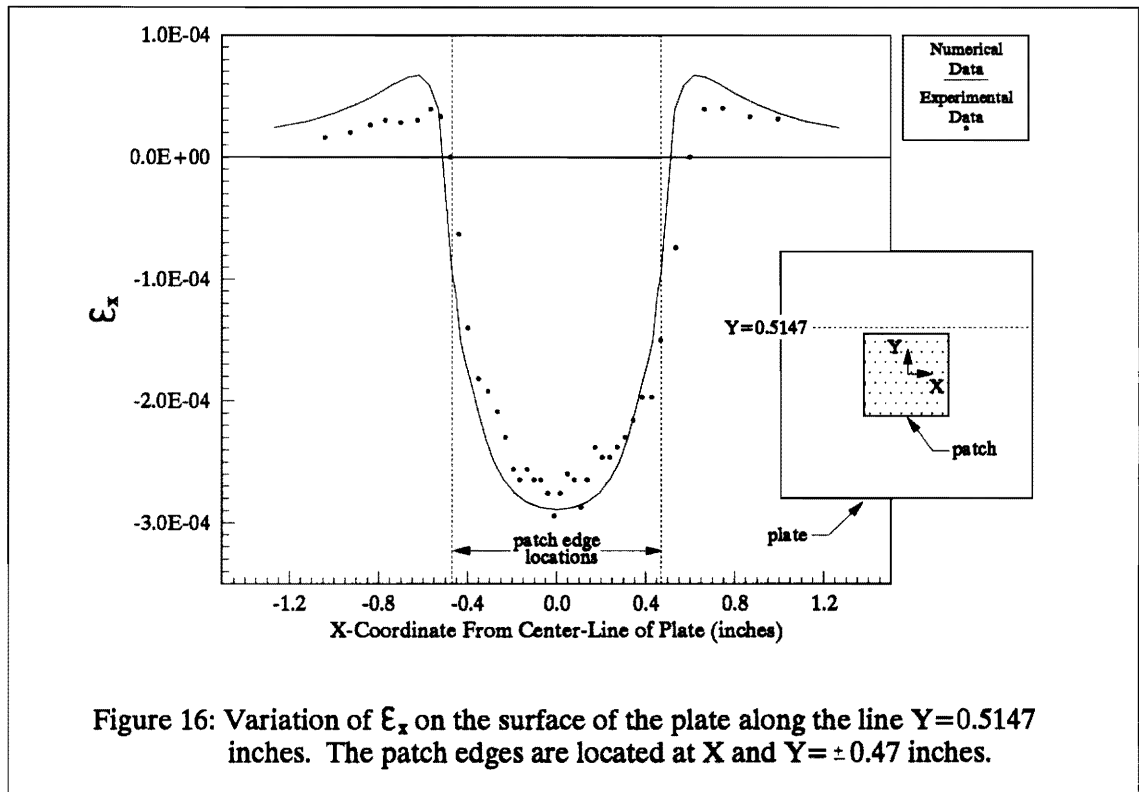


Figure 16: Variation of  $\epsilon_x$  on the surface of the plate along the line  $Y=0.5147$  inches. The patch edges are located at  $X$  and  $Y = \pm 0.47$  inches.

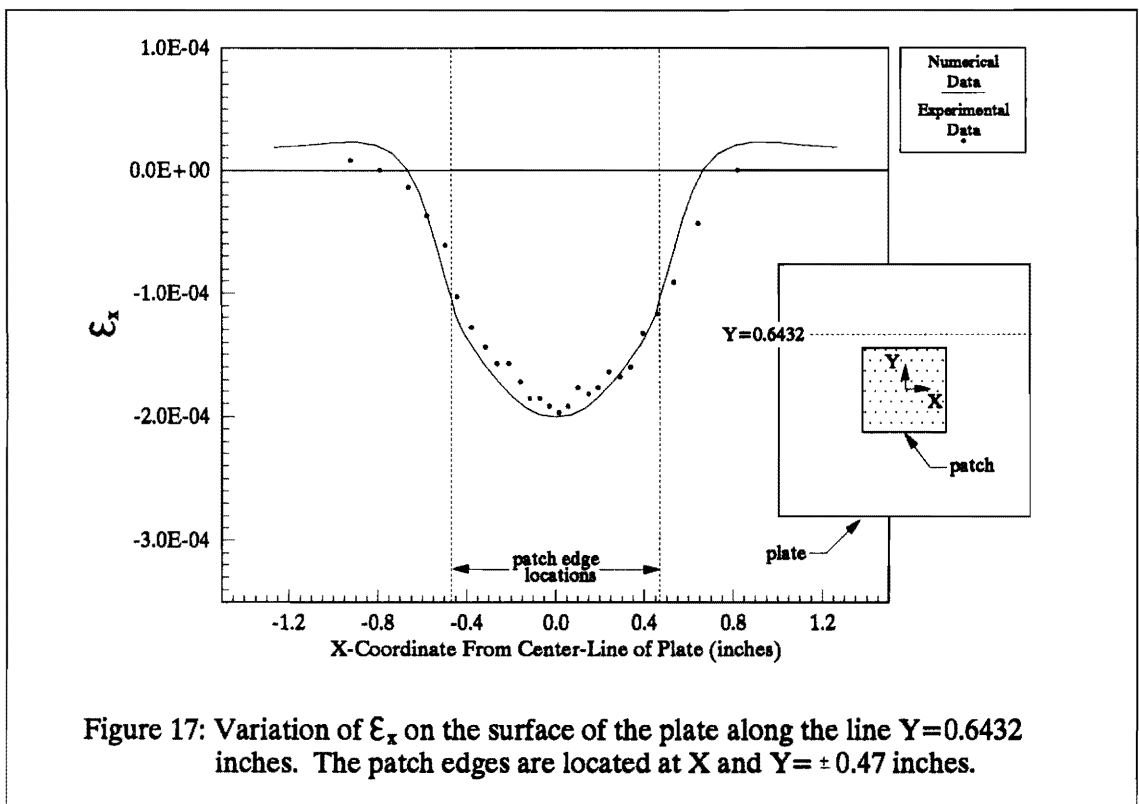


Figure 17: Variation of  $\epsilon_x$  on the surface of the plate along the line  $Y=0.6432$  inches. The patch edges are located at  $X$  and  $Y = \pm 0.47$  inches.

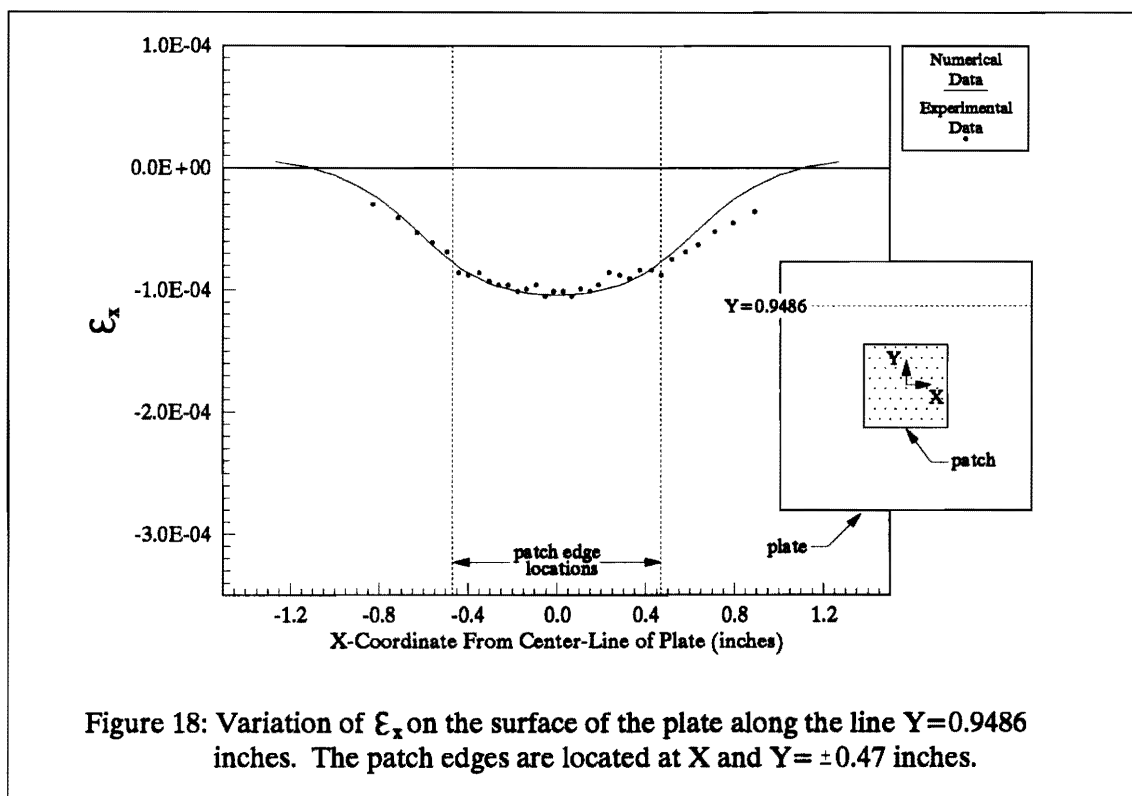


Figure 18: Variation of  $\epsilon_x$  on the surface of the plate along the line  $Y=0.9486$  inches. The patch edges are located at  $X$  and  $Y = \pm 0.47$  inches.

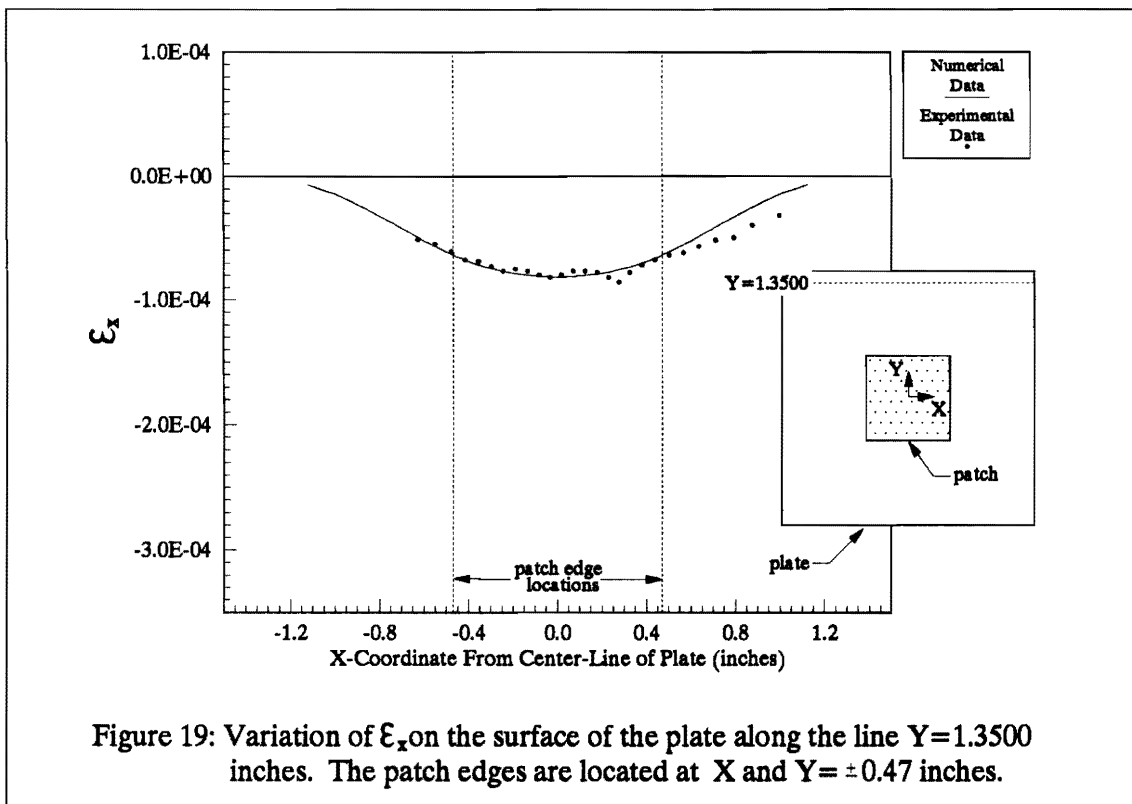


Figure 19: Variation of  $\epsilon_x$  on the surface of the plate along the line  $Y=1.3500$  inches. The patch edges are located at  $X$  and  $Y = \pm 0.47$  inches.



### **3.3.3.2 $\epsilon_y$ strain data**

Numerical and experimental  $\epsilon_y$  variations along the lines  $y = 0.5147, 0.6432, 0.9486, \text{ and } 1.3500$  inches are plotted in Figures 20-23, respectively. The numerical data presented in Figure 20 indicate a maximum  $\epsilon_y$  of approximately 0.000220 at  $x = 0.0$ . The experimental data shows the same trends, but is neither smooth nor particularly close to the numerical data. Analysis of the moiré fringe patterns in this area was extremely difficult due primarily to the proximity of the bottom extent of the usable fringe data. As seen in the subsequent figures, the experimental data is smoother and more closely matches the numerical data. Within the projected patch boundaries,  $\epsilon_y$  is tensile for all cases, supporting the previous conclusion about the material around the patch resisting the patch contraction by pulling against it. Strain becomes compressive outside the projected patch edges in Figures 20, 21, and 22 and approaches zero for Figure 23. No conclusive evidence of asymmetric behavior is displayed by the variations of  $\epsilon_y$  as might have been expected given the asymmetric nature of the v-field fringe pattern.

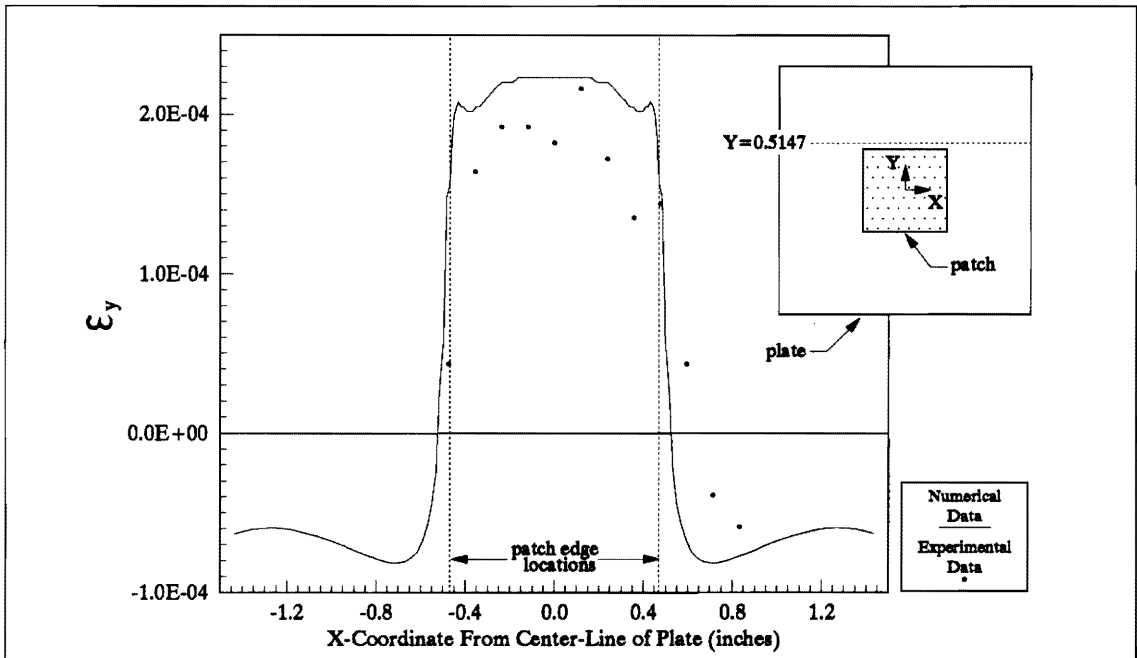


Figure 20: Variation of  $\epsilon_y$  on the surface of the plate along the line  $Y=0.5147$  inches. The patch edges are located at  $X$  and  $Y = \pm 0.47$  inches.

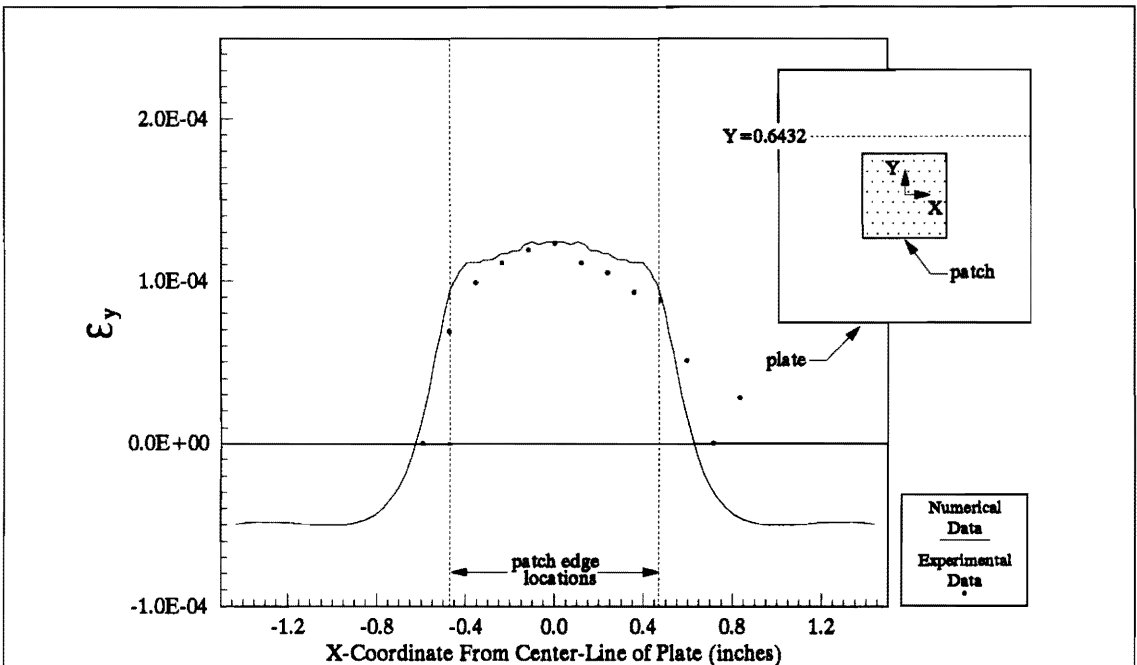


Figure 21: Variation of  $\epsilon_y$  on the surface of the plate along the line  $Y=0.6432$  inches. The patch edges are located at  $X$  and  $Y = \pm 0.47$  inches.

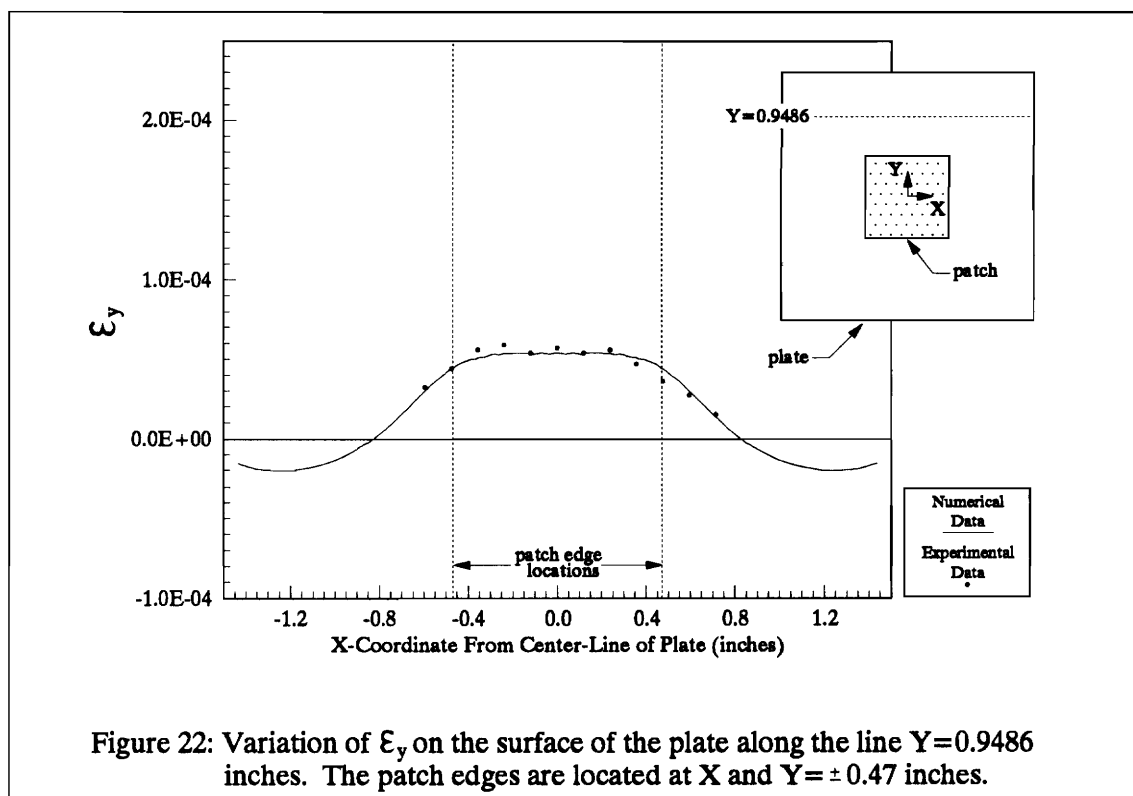


Figure 22: Variation of  $\epsilon_y$  on the surface of the plate along the line  $Y=0.9486$  inches. The patch edges are located at  $X$  and  $Y = \pm 0.47$  inches.

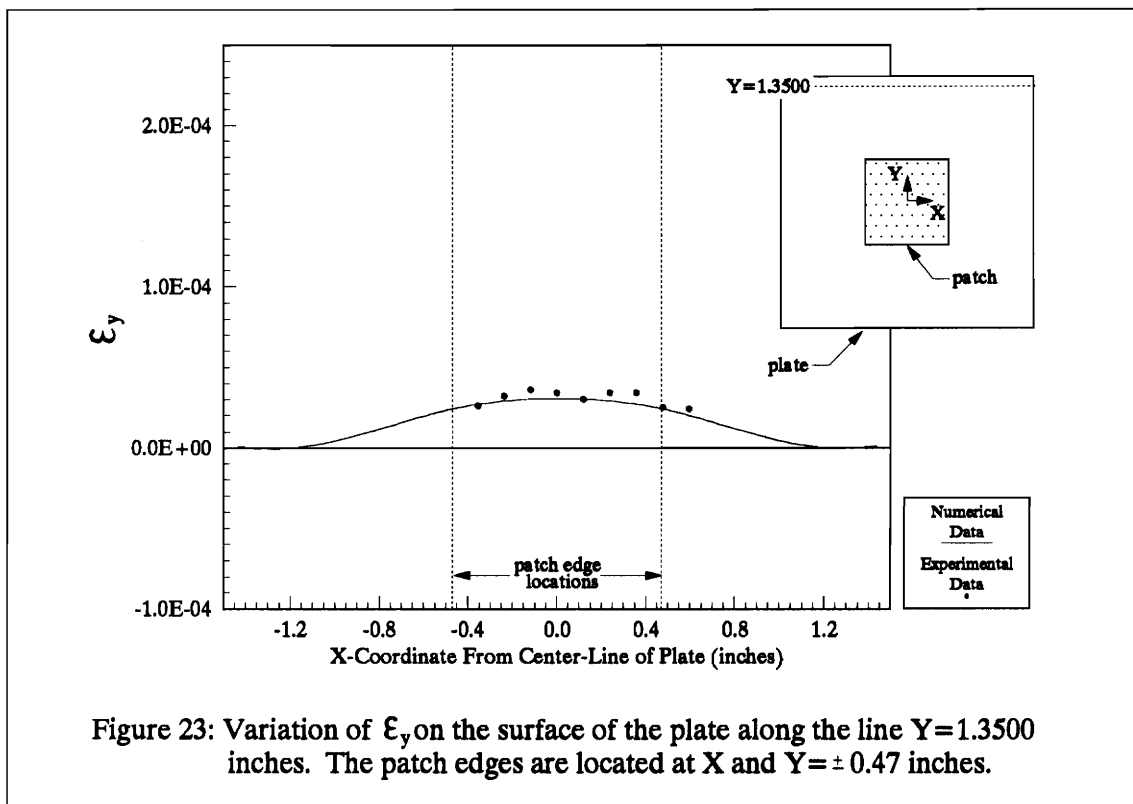
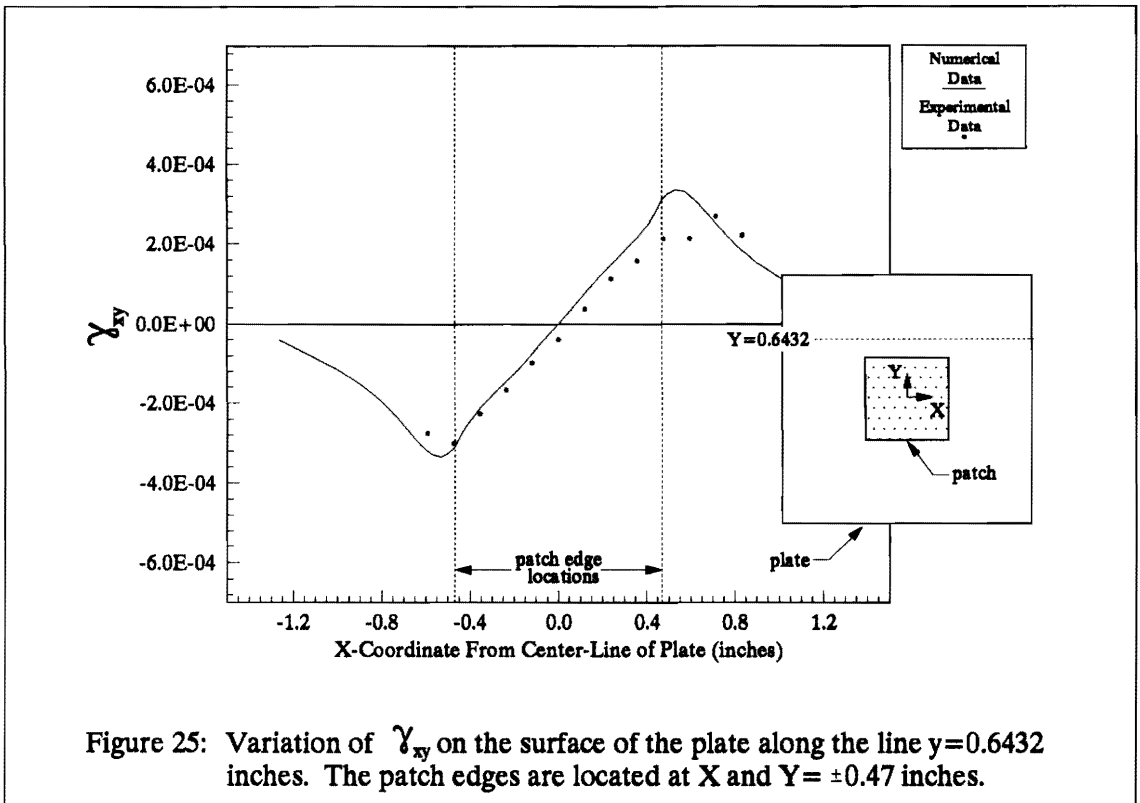
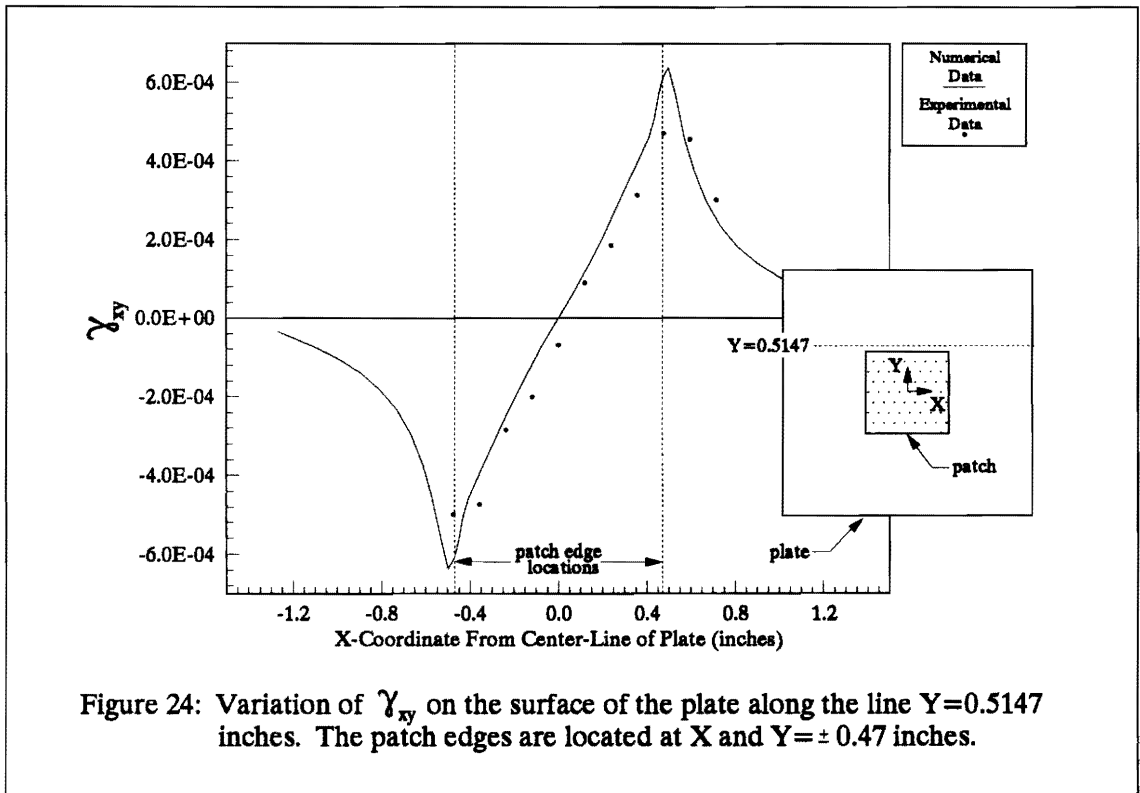


Figure 23: Variation of  $\epsilon_y$  on the surface of the plate along the line  $Y=1.3500$  inches. The patch edges are located at  $X$  and  $Y = \pm 0.47$  inches.

### **3.3.3.3 $\gamma_{xy}$ strain data**

The variation of  $\gamma_{xy}$  across the lines  $y = 0.5147, 0.6432, 0.9486,$  and  $1.3500$  is shown in Figures 24-27. In all cases, the experimental data appear to match the numerical data well except for a shift in the data toward the right. This is a clear indication of the asymmetries caused by patch misalignment and damage. Note that the scale of this plotted data is much larger than in the previous eight figures. Large peaks in the shear strain are present just outside of the projected patch boundaries in Figures 24 and 25. The numerical data presented in Figure 24 indicate a peak value of  $\pm 0.00064$  while the experimental data indicate a maximum shear strain of approximately  $\pm 0.0005$ .



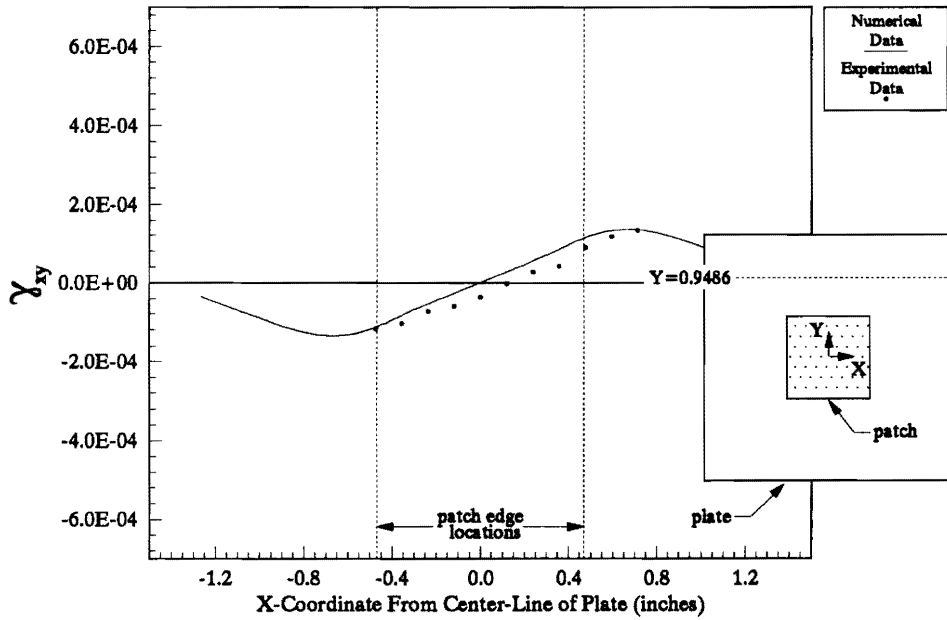


Figure 26: Variation of  $\gamma_{xy}$  on the surface of the plate along the line  $Y=0.9486$  inches. The patch edges are located at  $X$  and  $Y = \pm 0.47$  inches.

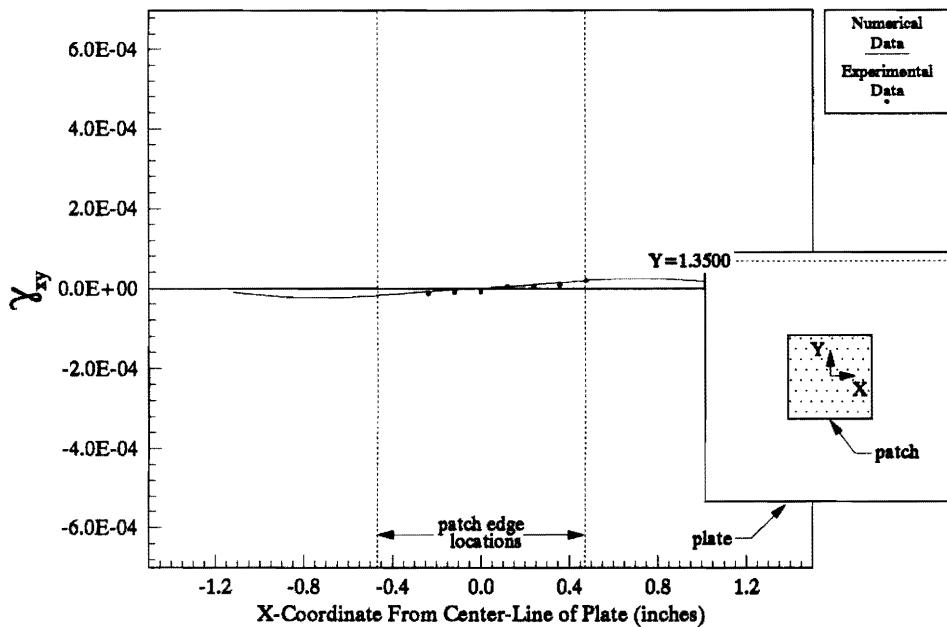


Figure 27: Variation of  $\gamma_{xy}$  on the surface of the plate along the line  $Y=1.3500$  inches. The patch edges are located at  $X$  and  $Y = \pm 0.47$  inches.

### 3.3.4 Finite Element Strain Results Near the Surface and Mid-Plane of the Plate

As stated previously, the finite element analysis program, ABAQUS, computed the strain data at the points of integration. For each 20-node brick element with reduced order integration, there are eight Gaussian integration points. If the element is rectangular with no skewing, warping, or tapering, the Gauss points are distributed near each of the corners as follows. Consider a rectangular brick element with a local coordinate system at the element center and axes parallel to the element edges. If the element sides are located at  $x = \pm a$ ,  $y = \pm b$ , and  $z = \pm c$ , then the Gauss points are located at the eight combinations of  $x = \pm 0.577a$ ,  $y = \pm 0.577b$ , and  $z = \pm 0.577c$ . The finite element model constructed for this research consisted of rectangular brick elements, two elements through the thickness of the plate and two through the patch. This resulted in eight distinct planes of Gauss points parallel to the plane  $z = 0$  at various locations through the plate and patch thicknesses. The variations of strain on two of these of Gauss point planes within the plate are examined in the following sections. These planes are located near the plate mid-plane at  $z = 0.0066$  inches ( $z/t = 0.0528$ ) and near the plate surface at  $z = 0.0559$  inches ( $z/t = 0.04472$ ).

#### 3.3.4.1 In-Plane Strains

The variations of  $\epsilon_x$  near the plate surface and mid-plane are plotted in Figures 28 and 29, respectively. Due to the symmetry of the specimen examined, the variation of  $\epsilon_y$  is identical to the variation of  $\epsilon_x$  rotated ninety degrees about the z-axis. The most striking feature of these plots is the large peak values of extensional strain near the plate surface at the patch edge. Recalling that the patch edges are located at  $x$  or  $y = \pm 0.47$  inches, this peak ridge occurs at the first row of Gauss points outside the patch edge. Toward the plate boundary, the in-plane normal strains drop off rapidly, but remain

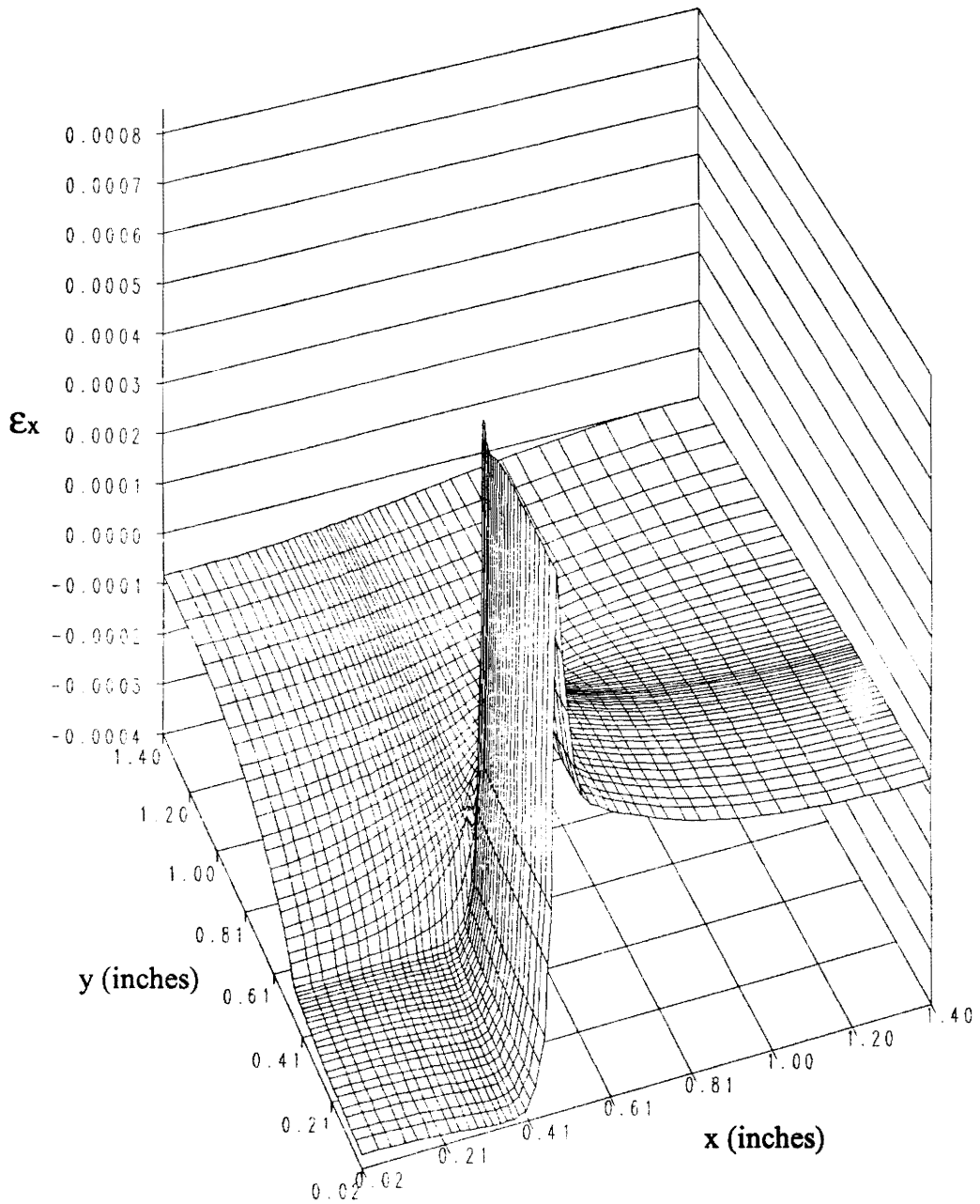


Figure 28: Variation of  $\epsilon_x$  on the plane of Gauss points nearest the plate surface of the surface bonded piezoceramic patch specimen.



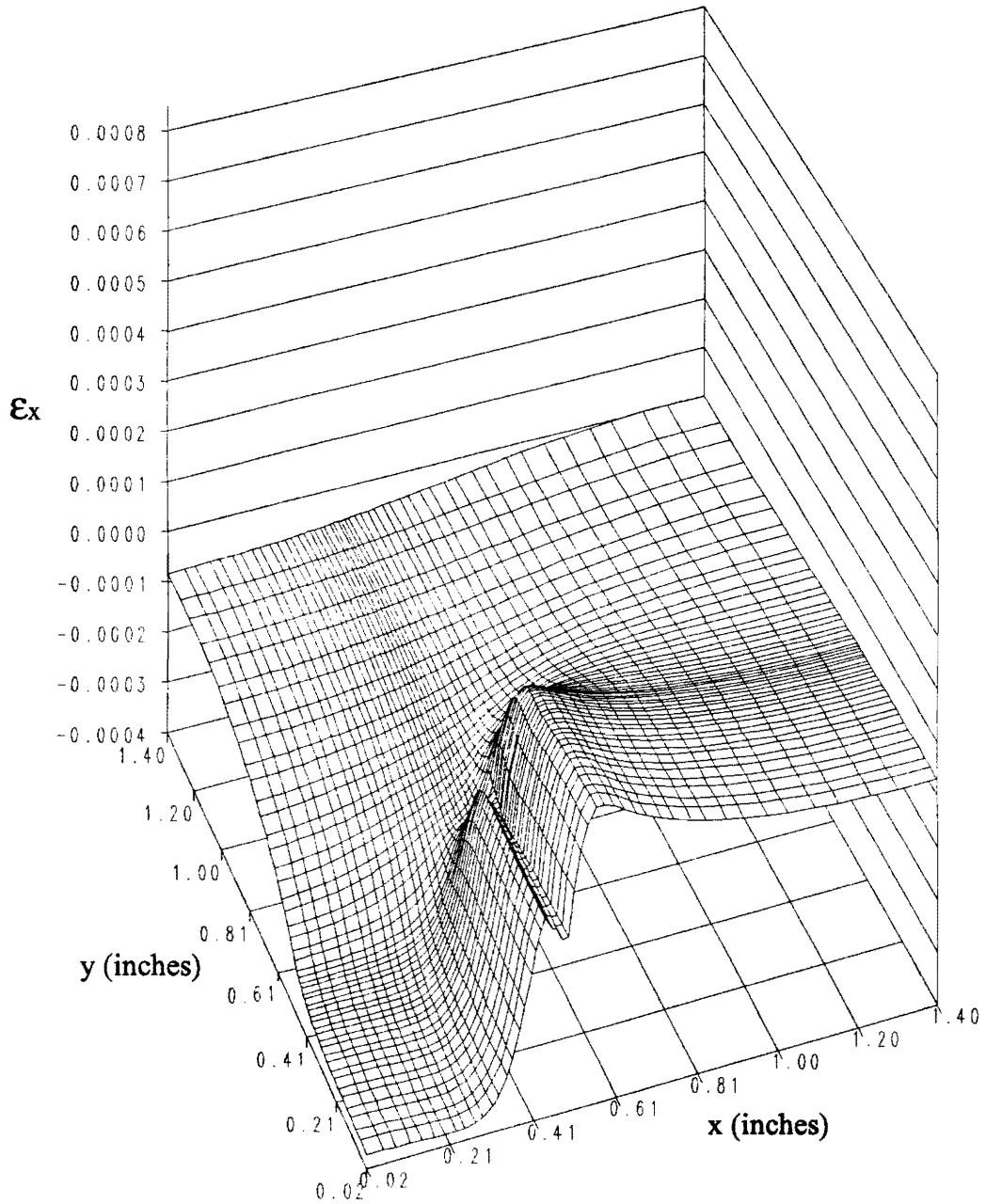


Figure 29: Variation of  $\epsilon_x$  on the plane of Gauss points nearest the plate mid-plane of the surface bonded piezoceramic patch specimen.

tensile, while toward the patch, the strains drop even more rapidly and become compressive. The peak tensile strain values along the ridge average approximately 0.000620, while the peak value of 0.000648 occurs at the patch corner. The minimum value of  $\epsilon_x$ , -0.000391, occurs inside the patch boundary at coordinates  $x = 0.346$  and  $y = 0.015$  inches, while the corresponding value of  $\epsilon_y$  occurs at  $x = 0.015$  and  $y = 0.346$ . Near the mid-plane, the behavior is almost identical, except for the magnitude of the large tensile ridge. The largest tensile strains at the mid-plane are approximately 0.000200.

Another feature visible in Figure 28 is the roughness of the strain variation near the peak tensile strain value. Although the variations are quite small, this behavior indicates that the finite element model may not have enough elements in the area of the patch corner. An oscillatory behavior of the normal strains near the patch edge is indicated in Figure 29. It is not clear at this time whether this behavior is real or whether it is due to the lack of mesh refinement in the area of the patch edge.

The variations of  $\gamma_{xy}$  near the plate surface and mid-plane are shown in Figures 30 and 31, respectively. Again, the most prominent feature is a large peak located near the patch corner in Figure 30. This peak, and the ridges accompanying it, occur at the first set of Gauss points outside the patch boundary. The maximum indicated value is 0.002179, while the minimum value is zero. The magnitude of the shear strain is roughly 3.9 times the magnitude of the applied in-plane patch free strain value of -0.000560. Slight fluctuations of the strain near the patch corner again indicate the need for mesh refinement. The shear strain behavior near the mid-plane is almost identical to the shear strain behavior near the surface. However, the magnitude of the peak is significantly lower.

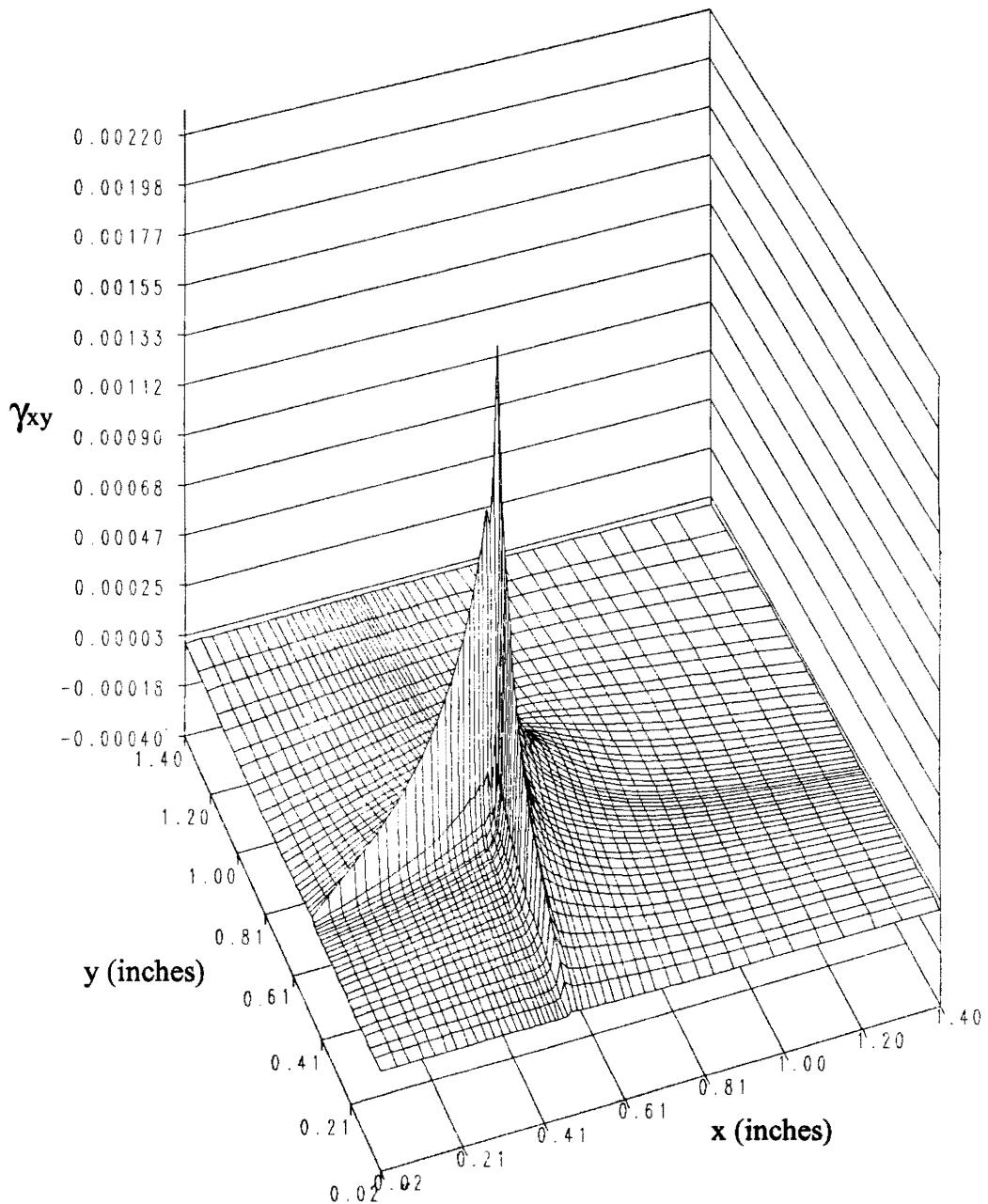


Figure 30: Variation of  $\gamma_{xy}$  on the plane of Gauss points nearest the plate surface of the surface bonded piezoceramic patch specimen.

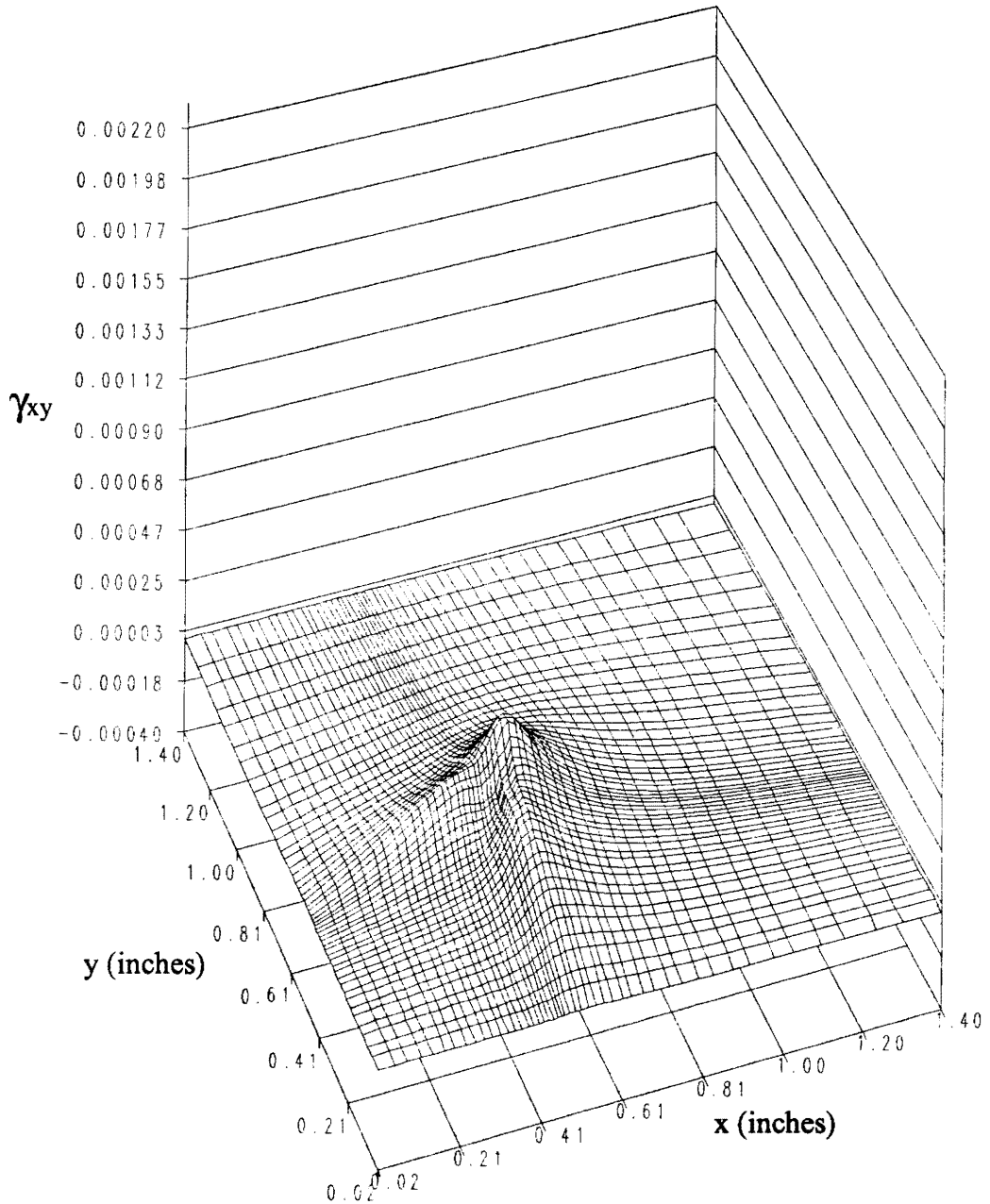


Figure 31: Variation of  $\gamma_{xy}$  on the plane of Gauss points nearest the plate mid-plane of the surface bonded piezoceramic patch specimen.

The large peaks seen in Figures 28 and 30 are indications of a singularity. The geometry of the specimen causes the patch edge to act as a singularity much as a crack tip or a notch is a singularity. The 90 degree intersections of patch edge with plate surface creates, in effect, a crack tip. Also, the drastically different material stiffnesses of the patch and plate will cause singularities to arise. Many factors in the real situation interact to relieve the severity of a singularity. Plastic deformations of the material immediately surrounding the singularity can reduce the levels of stress experienced by material still further from the singularity. The geometry in the real case was certainly not as precise as the finite element model geometry. The patch edges were probably slightly rounded due to sanding, and the adhesive spew was probably not cleaned to the point where the joint formed a right angle with the plate surface. The peak experimental values of in-plane strain presented in Figures 16, 20, and 24 are consistently lower than the corresponding numerical predictions, while the far field experimental strains match quite well. This indicates that the peak values of strain predicted by the finite element model were not attained in the real specimen.

#### **3.3.4.2 Out-of-Plane Strains**

The variations of  $\epsilon_z$  near the plate surface and mid-plane are plotted in Figure 32 and 33, respectively. The peak tensile value is 0.000420 spread over a broad, plateau-like area within the patch boundary. Near the patch boundary, the strain drops off and becomes negative just outside of the patch boundary and then becomes positive again. The peak compressive value of -0.000131 occurs near the corner of the patch. Note again the roughness of the values in the patch corner areas. Near the mid-plane, the resulting variation of strain is, as before, nearly identical to the strain variation near the plate surface, except in the region of the patch boundary. The peak tensile value, 0.000420, is the same but occurs over a smaller plateau region. Larger oscillations in  $\epsilon_z$

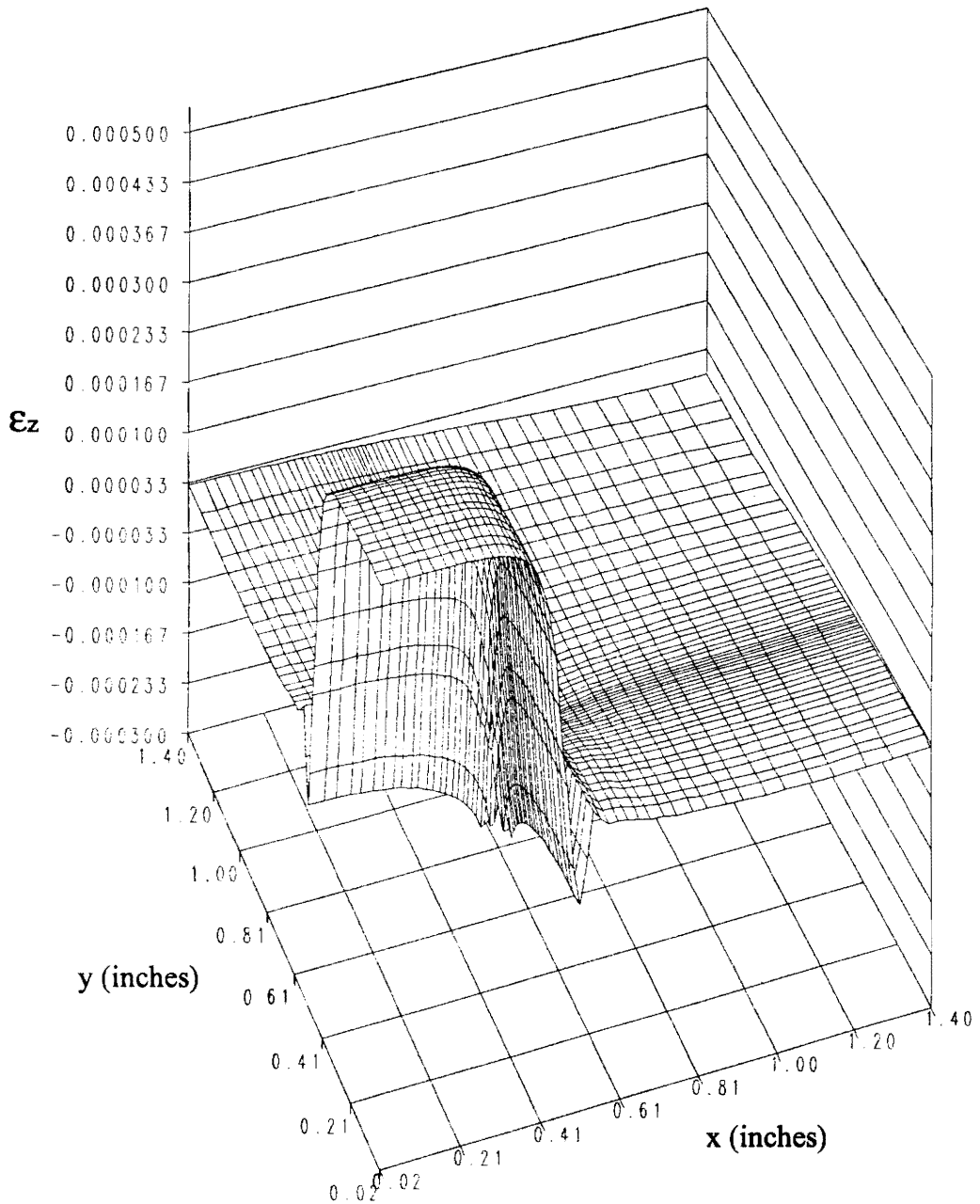


Figure 32: Variation of  $\epsilon_z$  on the plane of Gauss points nearest the plate surface of the surface bonded piezoceramic patch specimen.

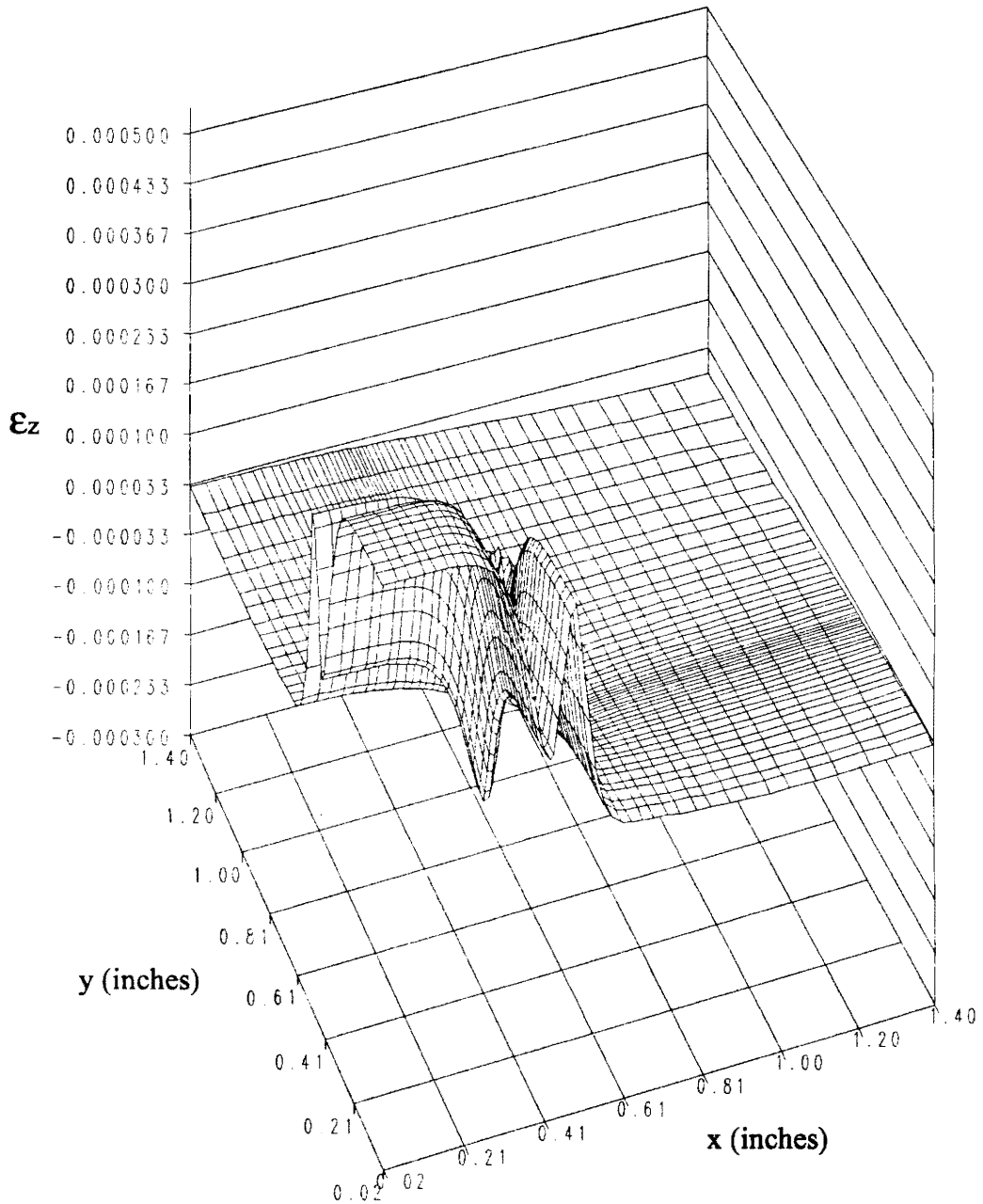


Figure 33: Variation of  $\epsilon_z$  on the plane of Gauss points nearest the plate mid-plane of the surface bonded piezoceramic patch specimen.

are seen near the patch boundary, with a slightly compressive peak occurring near the patch corner, but within the patch boundaries. No appreciable difference in the strain variation occurs past  $x$  or  $y = 0.7$  inches.

As with the in-plane normal strains, the variations of  $\gamma_{xz}$  and  $\gamma_{yz}$  are identical except for a ninety degree rotation about the  $z$ -axis. The variations of  $\gamma_{xz}$  near the plate surface and mid-plane are shown in Figures 34 and 35. A steep negative strain valley is visible in Figure 34 near the patch edge. The maximum value again occurred at the patch corner slightly outside the patch boundary and had a value of  $-0.001702$ . The out-of-plane shear across both Gauss point planes was nearly zero except in the neighborhood of the patch edge. Rough and oscillatory behavior is noticeable at the patch edge both near the plate surface and mid-plane.



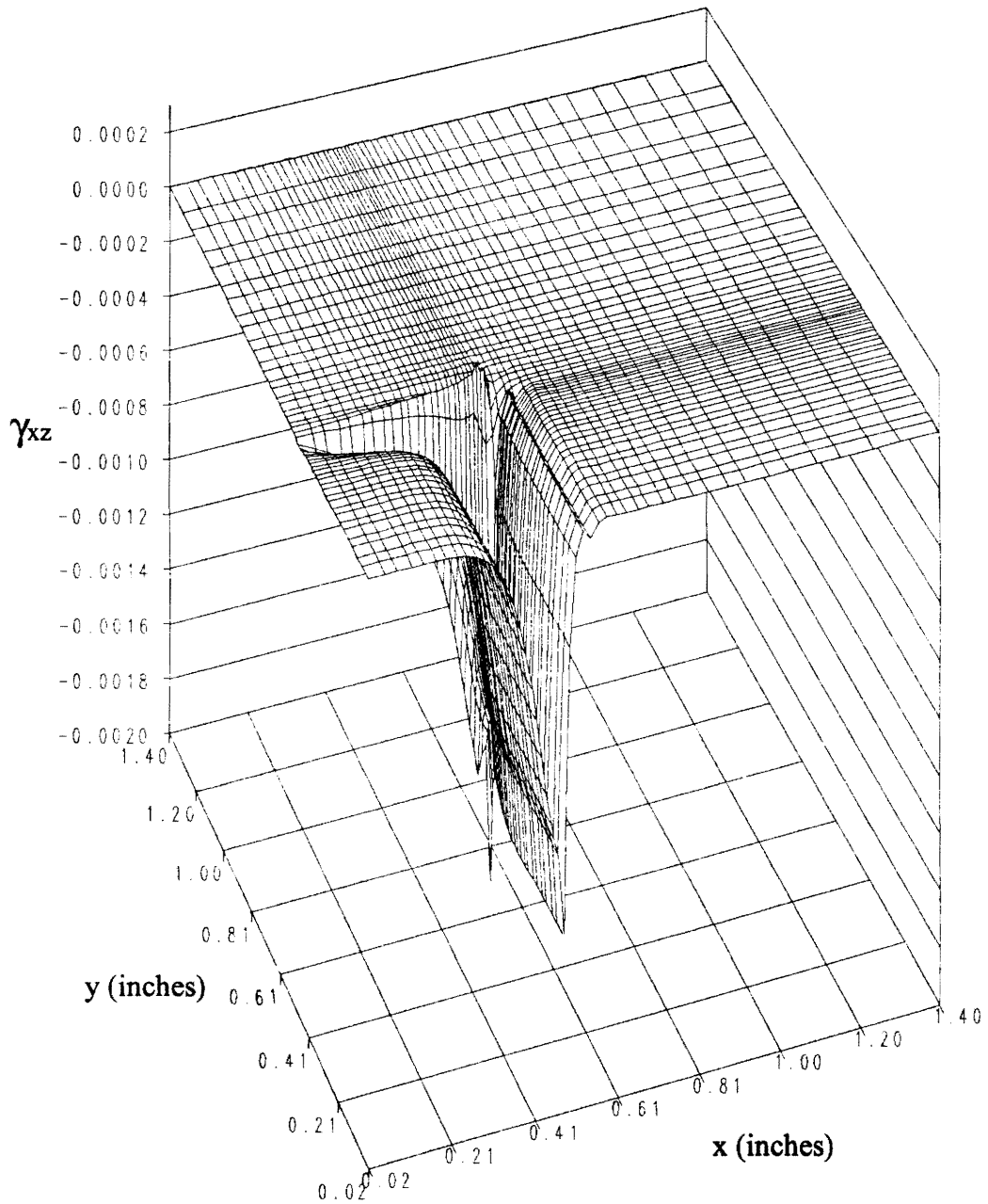


Figure 34: Variation of  $\gamma_{xz}$  on the plane of Gauss points nearest the plate surface of the surface bonded piezoceramic patch specimen.

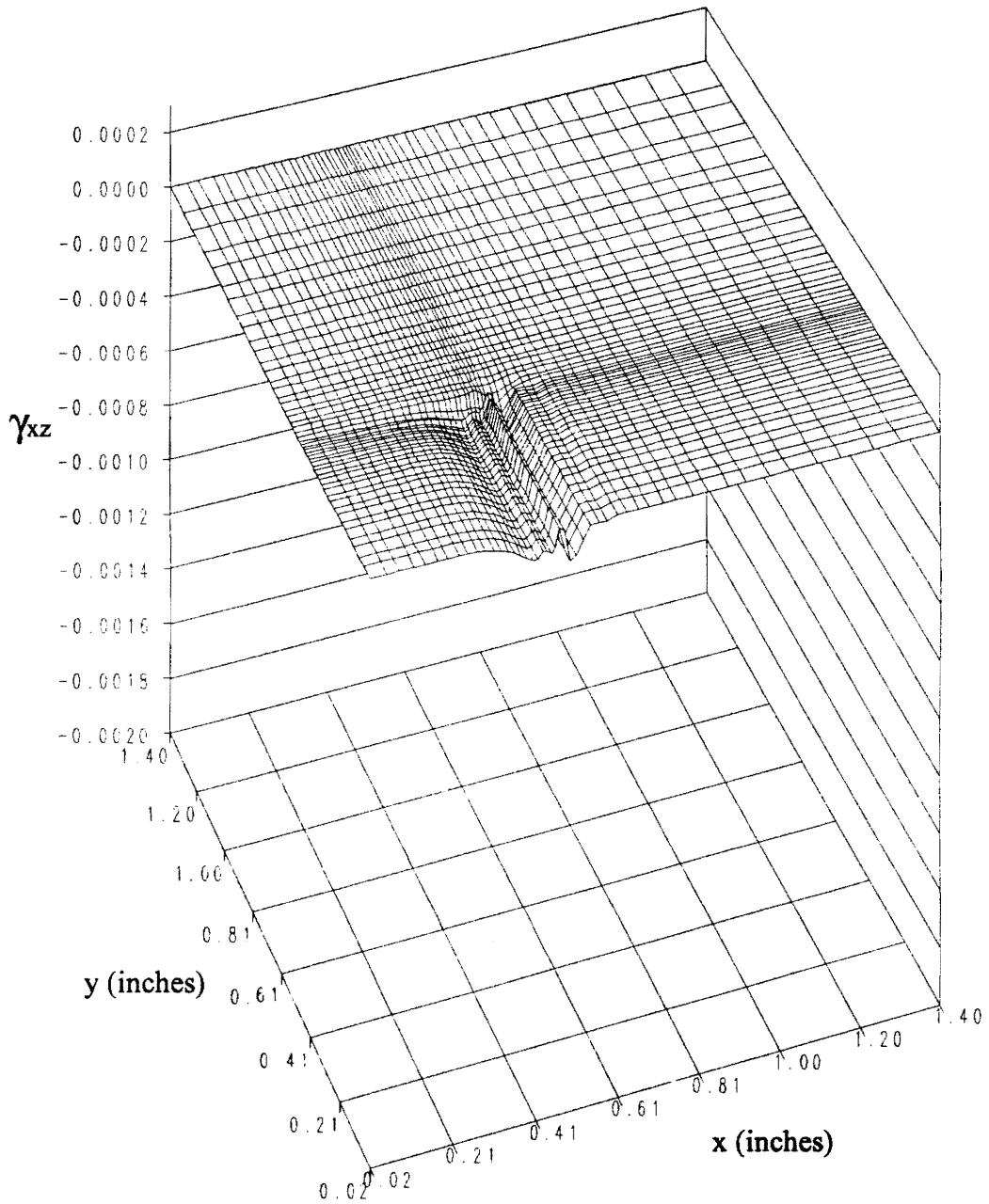


Figure 35: Variation of  $\gamma_{xz}$  on the plane of Gauss points nearest the plate mid-plane of the surface bonded piezoceramic patch specimen.

### 3.3.5 Stress Results Near the Plate Surface

Representative stress component variations on the layer of Gauss points nearest the plate surface are plotted in Figures 36-39. These stresses were calculated with Hooke's Law using the finite element determined strains. The variation of  $\sigma_x$ , plotted in Figure 36, is identical to the variation of  $\sigma_y$  except for a 90 degree rotation about the z-axis. A ridge of tensile stress occurs at the first row of Gauss points outside of the projected patch edges. The maximum tensile value of  $\sigma_x$  on this ridge occurs at the patch corner and has a value of 450 psi. The stress within the projected patch boundaries is essentially constant, with a value near 270 psi except near the patch boundaries where it increases rapidly. Outside of the top patch edge,  $\sigma_x$  drops to approximately -100 psi, increasing to a value of approximately -40 psi at the top plate edge. As expected,  $\sigma_x$  drops to zero at the right plate edge. At this edge,  $\sigma_x$  theoretically must be zero to satisfy the traction-free boundary condition existing on that edge.

The variation of  $\sigma_z$  near the surface of the plate is plotted in Figure 37. The most prominent feature is the sharp ridge of tensile stress surrounding the patch, which peaks at 227 psi. Outside this ridge, the stress is nearly zero, as it should be since the surface of the plate is a traction-free boundary. Slight oscillations on either side of the tensile ridge indicate lack of mesh refinement, but the oscillations on the outside of the ridge, and the ridge itself, demonstrate that the top layer of Gauss points is slightly below the surface of the plate.

The variation of  $\tau_{xy}$  is shown in Figure 38. At the coordinate system origin, the shear is zero. It stays zero as the projected patch edges are approached along the coordinate axes, but increases as the corner of the patch is approached. At the patch

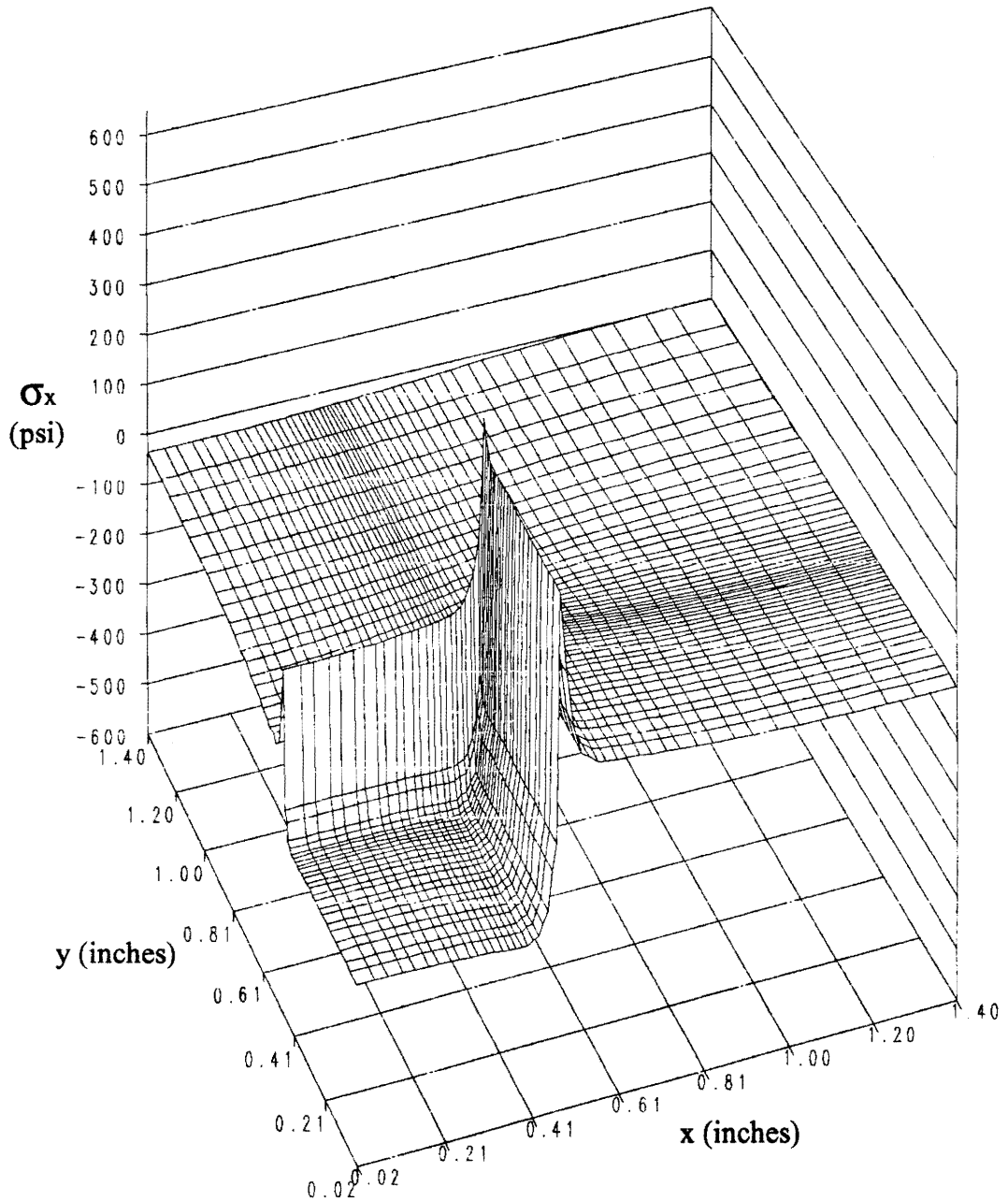


Figure 36: Variation of  $\sigma_x$  on the plane of Gauss points nearest the plate surface of the surface bonded piezoceramic patch specimen.

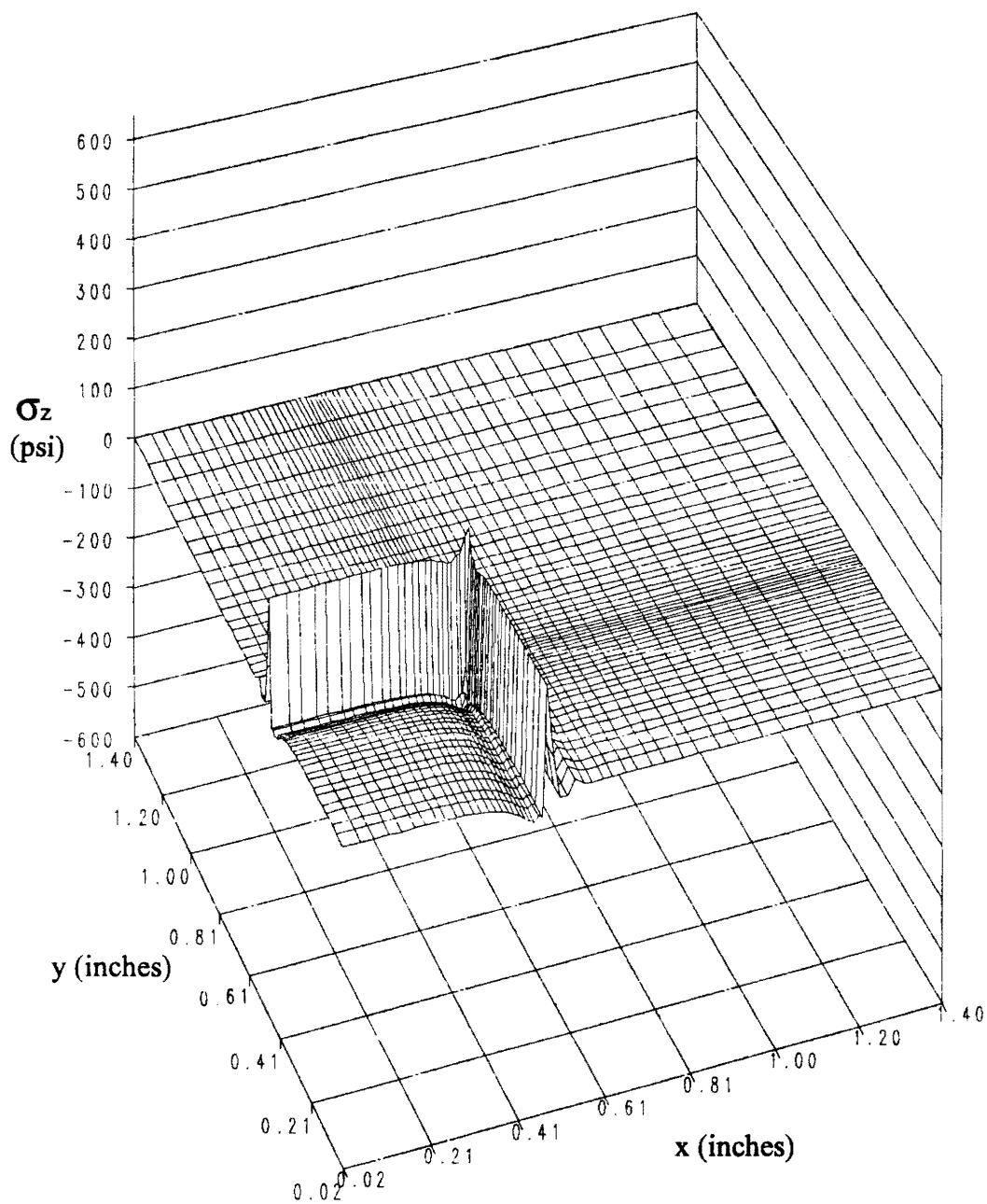


Figure 37: Variation of  $\sigma_z$  on the plane of Gauss points nearest the plate surface of the surface bonded piezoceramic patch specimen.

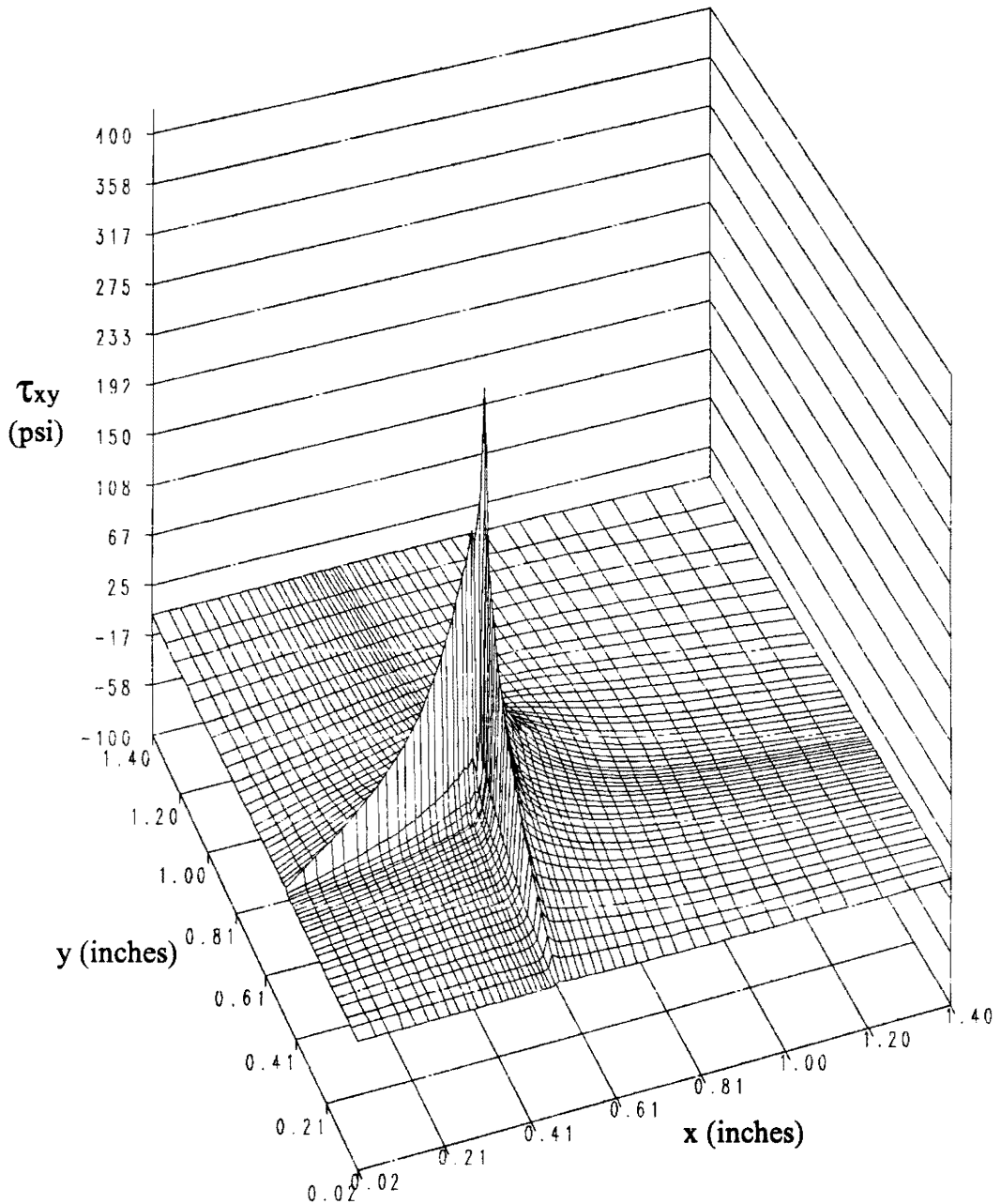
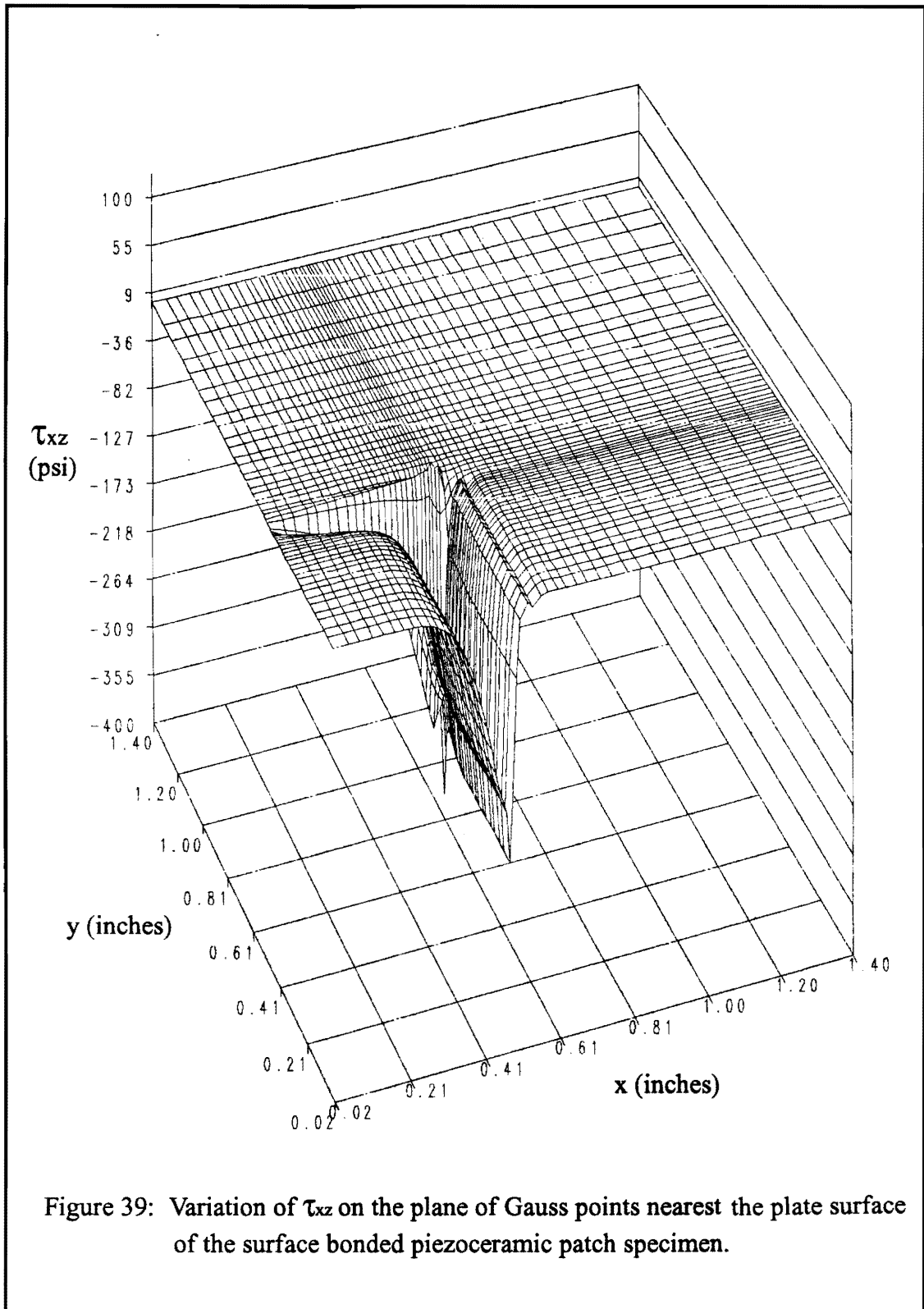


Figure 38: Variation of  $\tau_{xy}$  on the plane of Gauss points nearest the plate surface of the surface bonded piezoceramic patch specimen.



edge,  $\tau_{xy}$  rapidly increases, jumping to a peak value of 721 psi just outside the patch corner. The shear stress then rapidly decreases, approaching zero at the plate edges.

The variation of  $\tau_{xz}$  is the same as  $\tau_{yz}$  except for a 90 degree rotation about the z-axis. Variations of  $\tau_{xz}$  are plotted in Figure 39.  $\tau_{xz}$  has a value of zero at the patch center, remaining zero in the central portion of the projected patch boundaries. As the right side of the patch is approached the shear begins to drop with increasing slope. Just outside the patch corner,  $\tau_{xz}$  reaches its maximum value of -563 psi.  $\tau_{xz}$  also decreases as the top edge of the patch is approached.

The stress levels found in this analysis are not statically significant in the sense that the plate material, or adhesive material, is not likely to fail under these conditions. Since both of the normal stress maxima are tensile, the concern about a fatigue failure of the adhesive bond line becomes real. The actuation of a patch induces relatively large peel stresses around the patch edge, especially at the patch corner. This peel tendency is apparent in Figure 13b of the deformed finite element grid. Depending on the failure loads and fatigue characteristics of the adhesive used to bond the patch to the plate surface, these peel stresses could present serious problems.



## **Chapter 4: Induced Strain of Actuation in a Flat Plate With an Embedded Piezoceramic Patch**

### **4.1 Moiré Interferometry Experiment**

#### **4.1.1 Specimen Geometry, Construction, and Materials**

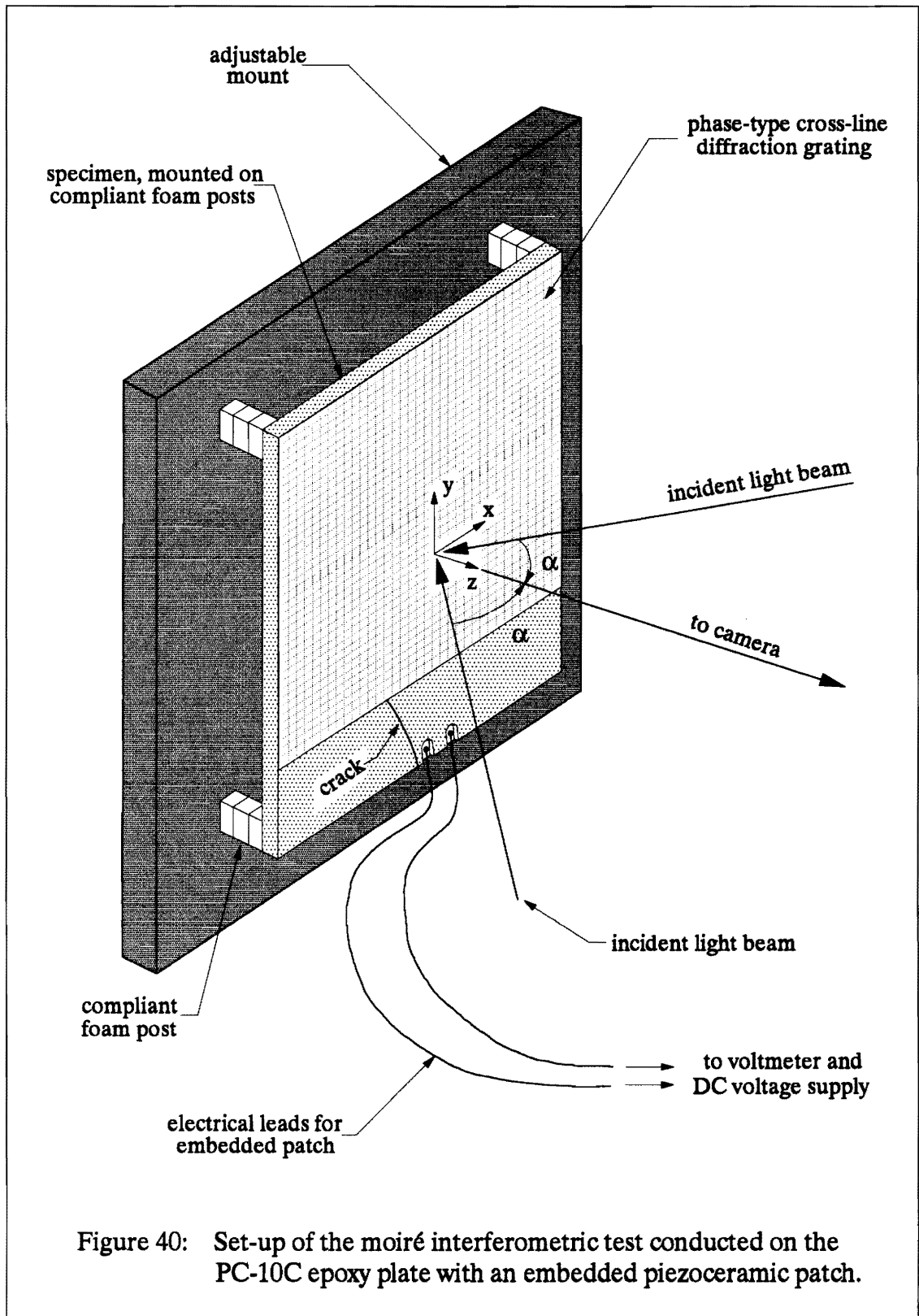
The specimen examined in this experiment consisted of a PC-10C epoxy plate, 2.43 inches long, 2.36 inches wide, and 0.1 inches thick with a piezoceramic patch embedded at the plate mid-plane. The patch, centered with respect to the plate width and length, was 1.03 inches long and 0.87 inches wide with the standard thickness of 0.0095 inches. This specimen was manufactured in several steps. A mold was constructed of a flat sheet of plexiglass with plexiglass walls bonded to the surface, forming a 2.5 inch square open-ended box. A thin layer of PC-10C epoxy was poured into the mold and allowed to cure. The walls of the mold were then removed, this being possible due to poor adhesion of epoxy to plexiglass. The thin layer of epoxy was then sanded to a thickness of 0.045 inches. A piezoceramic patch was prepared by cutting and sanding to the above dimensions and soldering brass electrical leads to the resulting patch. This patch was then bonded to the thin layer of cured PC-10C using the procedure described in the previous chapter. The electrical leads were also bonded to the surface of the cured epoxy and were allowed to overhang the edges where the mold walls were located. After the plexiglass walls were reattached, another layer of epoxy was poured over this assembly and allowed to cure. Upon cure, when the walls were removed, the overhanging part of each electrical lead broke and was removed with the walls. The newly cured epoxy was then sanded so that the overall thickness was 0.1 inches. After

removal from the plexiglass base, the edges of the plate/patch assembly were smoothed to the above dimensions by sanding. The bottom edge of the plate where the electrical leads had projected was also sanded since there were no longer any projecting electrical leads. The leads were re-exposed by removing small portions of epoxy at the bottom edge until the leads were adequately exposed. During the removal of epoxy, a small crack was inadvertently started near this edge, extending toward the nearest patch corner. An attempt was made to fill the crack with a low viscosity adhesive, resulting in the crack being partially filled near the front and back surfaces of the plate. As a final step in the specimen construction, a phase-type cross-line diffraction grating, 2.36 inches wide and 1.80 inches long, was replicated on the top portion of the plate. This resulted in complete coverage of the surface over the embedded patch with coverage extending to the top edge of the plate.

The material properties of PC-10C epoxy and G-1195 PZT are listed in Table 3 in the previous chapter. The adhesive used to bond the patch to the first half of the epoxy plate was PC-10C epoxy, so material properties of the bond line should not be an issue. A cyanoacrylate adhesive with unknown properties was used in the attempted crack repair.

#### **4.1.2 Test Set-up and Experimental Procedure**

The set-up of the experiment conducted on the specimen described above is shown in Figure 40. The specimen was mounted to an adjustable mirror mount using compliant posts constructed of multiple layers of foam-core double-stick tape. It was connected to a voltmeter and DC voltage supply such that the applied voltage was the same sign as the poling voltage of the patch. Due to optical limitations, the entire diffraction grating was not illuminated. A 2.11 inch wide by 1.42 inch long area



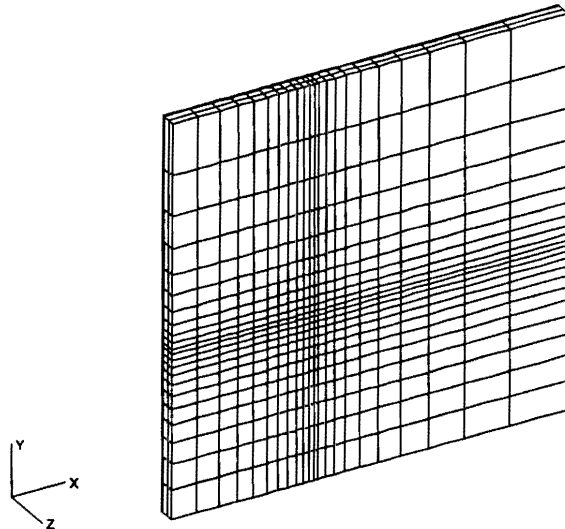
centered on the upper portion of the plate was illuminated for the u-field, while a 1.30 inch wide by 1.74 inch long area was illuminated for the v-field.

Only one level of applied voltage was examined in this experiment, 343 volts, the maximum output of the DC voltage supply. The null field was quite poor so the moiré-of-moiré method was again employed. A carrier pattern of rotation of approximately 8 fringes per millimeter was applied to the 0-volt and 343-volt patterns. The 0-volt and 343-volt u- and v-fields were viewed and photographed, and the resulting negatives were overlaid to yield the true 343-volt displacement fields.

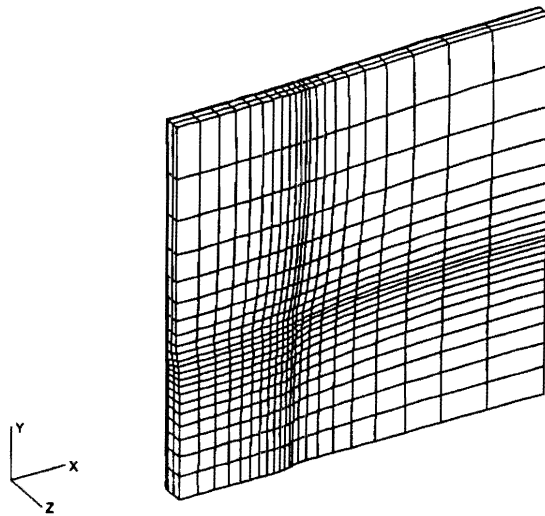
## **4.2 Finite Element Modeling**

### **4.2.1 The Finite Element Model**

The finite element model of the embedded patch/plate hybrid structure was very similar to the model of the surface bonded patch/plate model described in the previous chapter. As for the surface bonded patch model, pre-processing was accomplished with PATRAN, the element types were 20-node, reduced integration brick elements, the coordinate system origin was placed at the mid-plane center of the model, one eighth of the actual specimen was modeled, and the proper displacements on the planes of symmetry were specified to be zero. The y-axis of the coordinate system was aligned to point in the direction of the longest plate and patch dimensions. The patch was modeled using two elements through its thickness. The plate material over the patch was also modeled using two elements through the thickness, while the plate material surrounding the patch was modeled with four elements through its thickness. These four layers of elements were spaced through the plate thickness so as to correspond with the spacing of the patch and remaining plate elements. The resulting finite element grid contained 9821 nodes and 1936 elements and is pictured in Figure 41 along with the deformed grid. The



undeformed finite element grid  
(b)



deformed finite element grid  
(b)

Figure 41: Finite element model grid views; undeformed and deformed.

model geometry matched that of the actual specimen and did not suffer from the lack of an adhesive bond line as with the previous model.

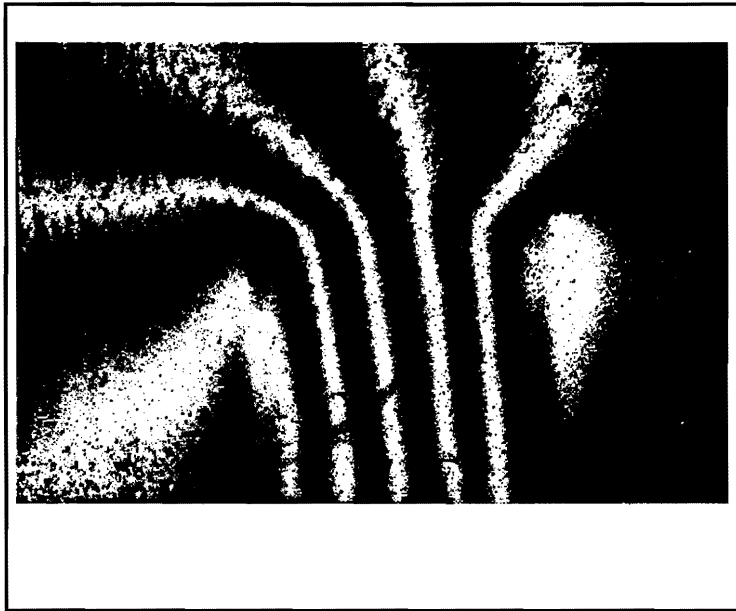
#### **4.2.2 Finite Element Analysis**

A linear analysis was performed on the above model using ABAQUS on the APOLLO DN10000 computer. The elements modeling the plate were specified to have a 0.45 Msi Young's Modulus and a 0.38 Poisson's ratio, while the coefficient of thermal expansion was specified to be zero. The elements modeling the patch were specified to have a 9.1 Msi Young's Modulus and a 0.28 Poisson's ratio. As before, to adequately model the in-plane and out-of-plane piezoceramic deformation, the in-plane and out-of-plane CTEs were different. The in-plane CTE was specified to be  $-0.000639/\text{degree}$  while the out-of-plane CTE was specified to be  $0.002595/\text{degree}$ , in correspondence with the in-plane and out-of-plane free patch strain presented in chapter 2. With the application of a one degree temperature change, the finite element model described simulates the application of a 343 volt charge across the embedded patch in the actual specimen. The analysis of this model calculated displacement data at the nodes and strain data at the Gauss points.

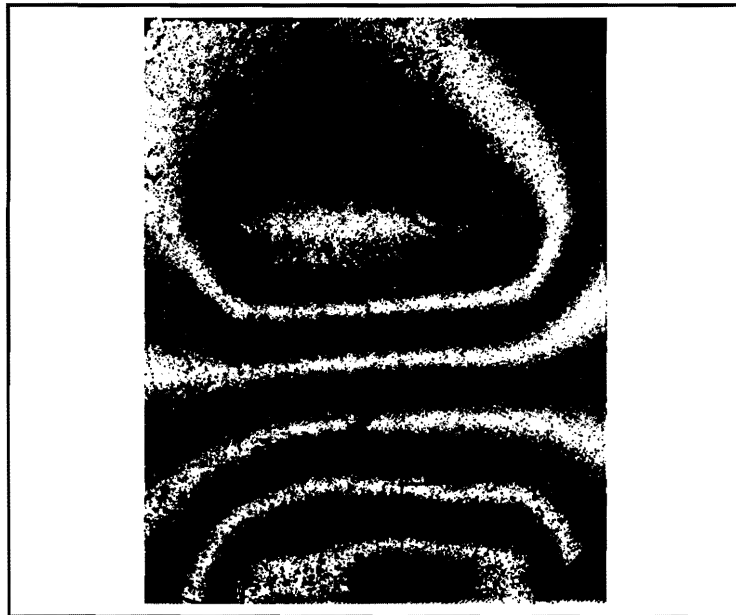
### **4.3 Results and Comparisons**

#### **4.3.1 Moiré Fringe Pattern Results**

The moiré-of-moiré fringe pattern results obtained from the above testing are shown in Figure 42. The u-field fringe pattern, pictured in Figure 42a, is clearly not symmetric. The fringes lean to the left noticeably. This asymmetry can be seen, to a lesser degree, in Figure 42b of the v-field where the fringes tilt down more at the left side



(a)



(b)

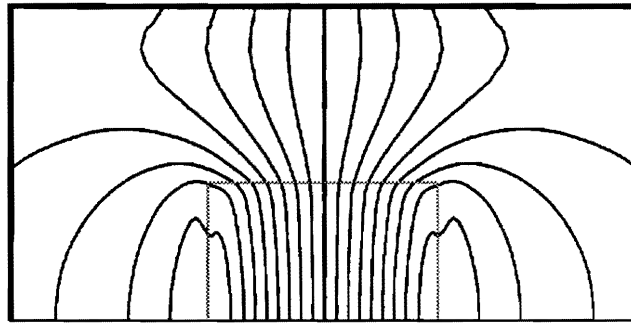
Figure 42: U- and v-field fringe pattern results from the moiré interferometry experiment conducted on the embedded piezoceramic patch specimen. (a) is the u-field fringe pattern. (b) is the v-field fringe pattern.

of the specimen. Again, a misalignment of the patch with respect to the plate edges is a possible contributor to this asymmetric behavior. Other possible causes of the asymmetric behavior include variations of plate thickness or mechanical properties. Since the plate was cast from a liquid adhesive, the possibilities of uneven mixing or curing are quite real, whereas the plate examined in the previous chapter was cut from a professionally manufactured sheet of high quality epoxy.

### **4.3.2 Comparison of Moiré Fringe Patterns to Finite Element Displacement Contours**

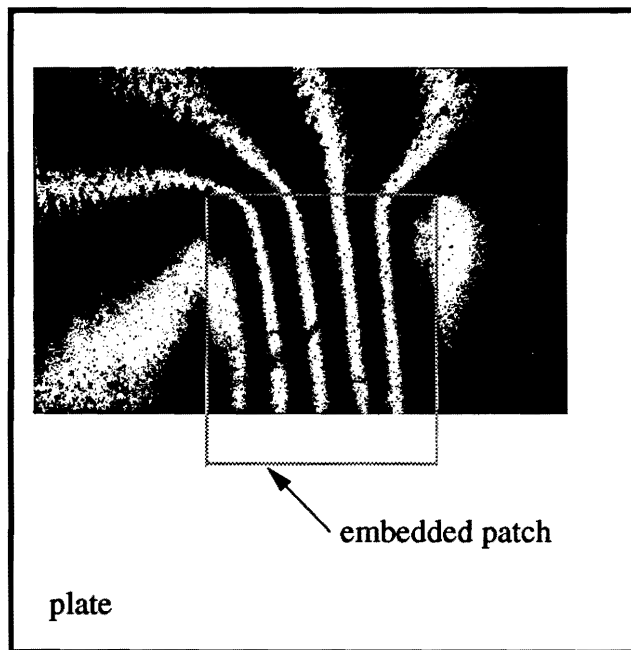
Finite element generated x-displacement contours and the moiré interferometry u-field fringe pattern is presented in Figure 43. The finite element displacement contours have been mirrored about the y-axis for this comparison. It is clear from this comparison that the finite element modeling and experimental results are very different in magnitude. Patch disbonding or partial depoling as well as the patch location were considered as possible causes of this poor match. After sectioning and close examination, disbonding of the patch with respect to surrounding material was not found, but the patch was found to be located slightly closer to the back surface of the plate than to the front surface of the plate. This off centered patch location and the possible partial depoling of the piezoceramic patch were the likely causes of the poor correlation. Crawley and Anderson (1990) caution the user of piezoceramics about the possibility of partial or full depoling of piezoceramic materials during use. The charge holding capabilities of the embedded patch were tested before the moiré fringe data was recorded. The depoling could have occurred at that time. A further recommendation suggests the repoling of the piezoceramic *in situ* through the application of a large electric field across the patch. It was decided that the repoling of the patch was unwise due to the unknown nature of the voltage/strain characteristics of the newly repoled patch.





finite element displacement contours

(a)



moiré displacement fringe pattern

(b)

Figure 43: Comparison of a moiré interferometric fringe pattern (u-field, 343 volts) and finite element displacement contours (x-displacements, -0.000639 in-plane patch free strain).

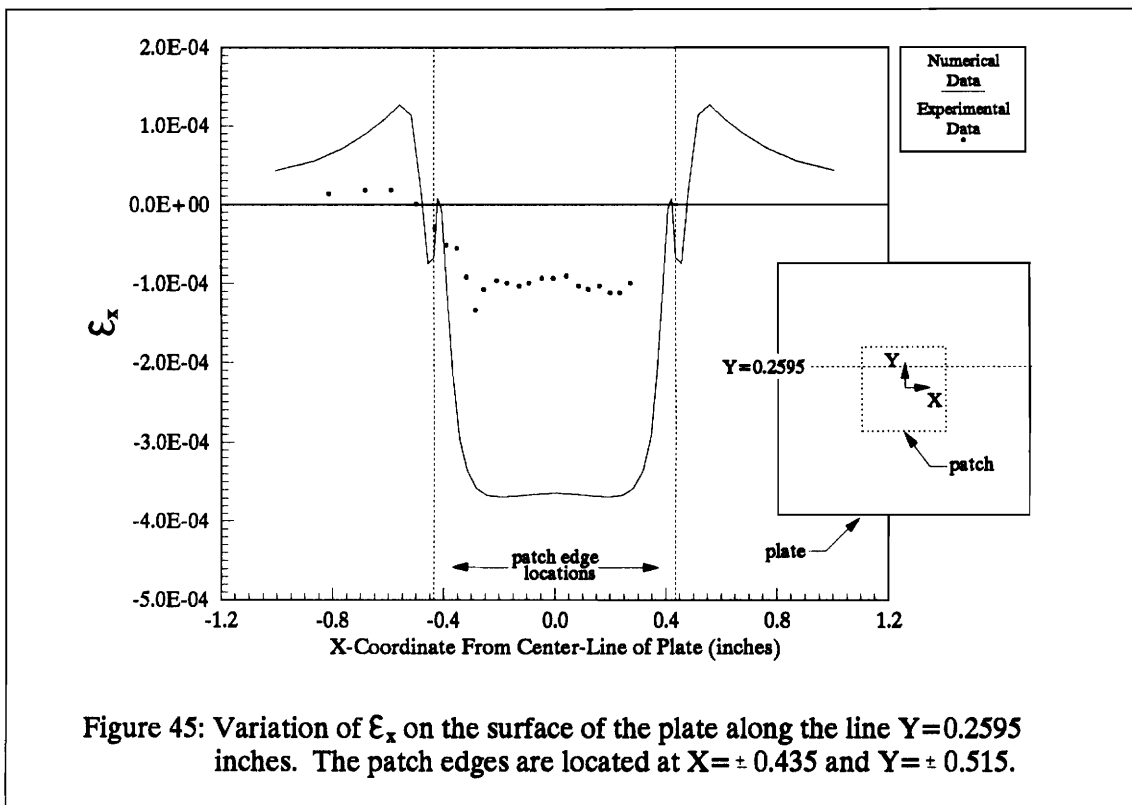
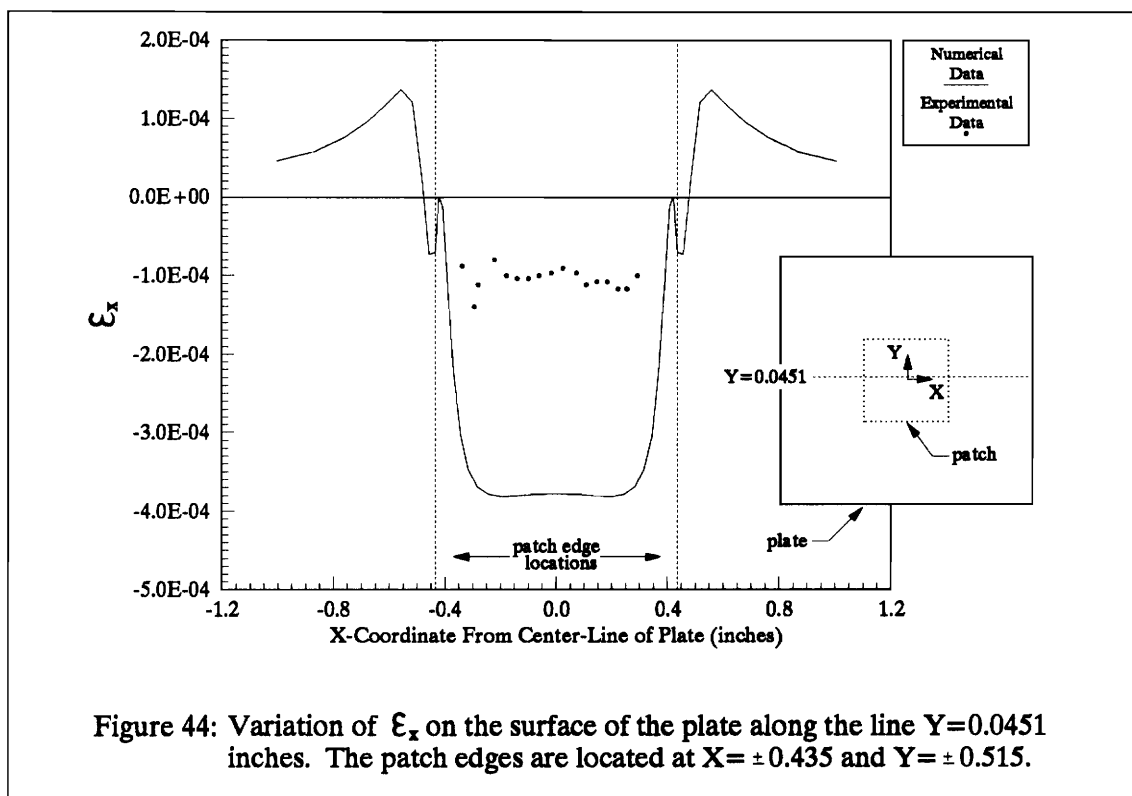
In spite of the magnitude mismatch, the general shape of the moiré fringe pattern is similar to the finite element generated displacement contours. A slight bump in the fringes along the right and particularly the left patch edge is similar to the bump experienced in the finite element displacement contours that cross the left and right patch boundaries. The qualitative similarity to the numerical displacement contours is reassuring.

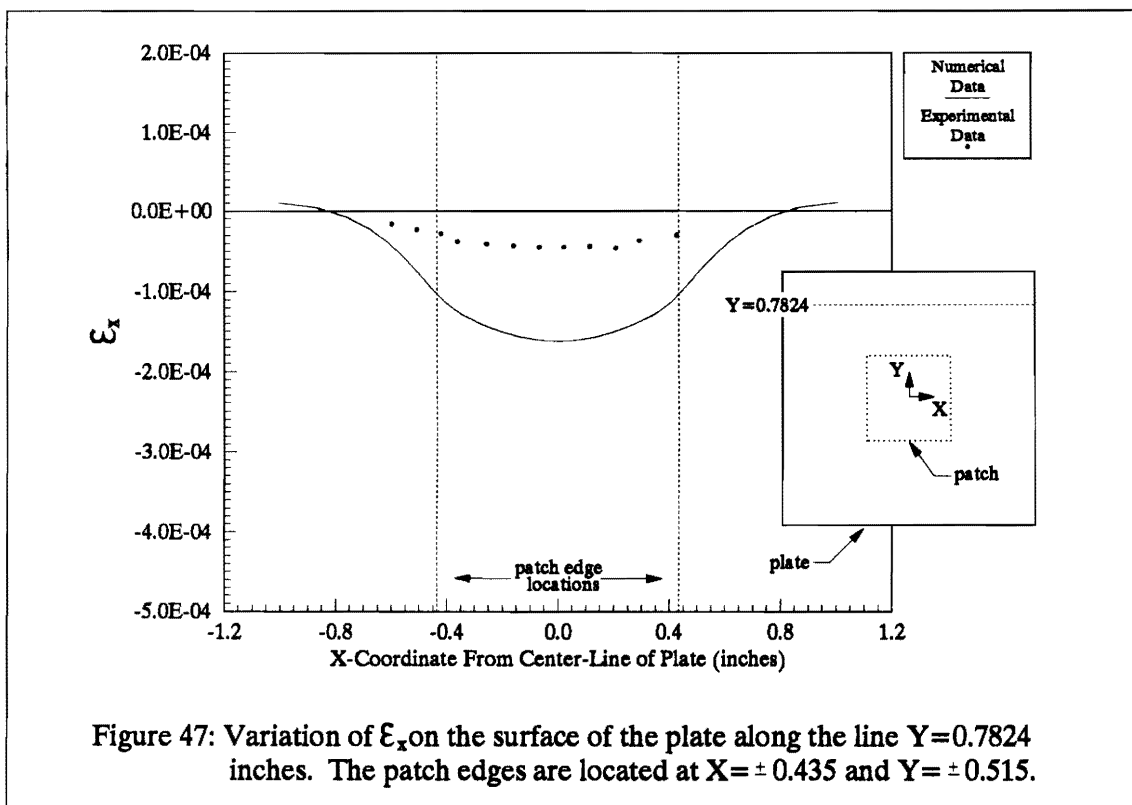
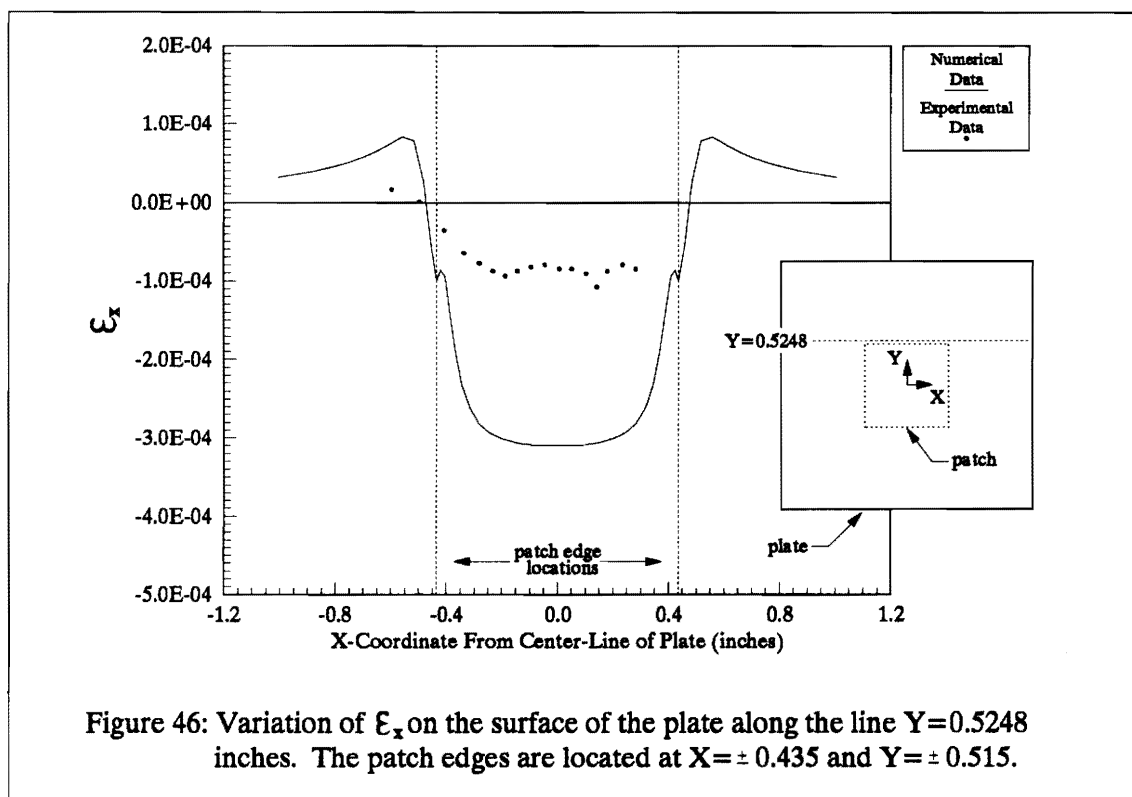
### **4.3.3 Comparison of Experimental and Finite Element Surface Strain Data**

Experimental and numerical variations of  $\epsilon_x$ ,  $\epsilon_y$ , and  $\gamma_{xy}$  on the surface of the plate at various locations are examined in the following sections. The strains were evaluated along four horizontal lines at locations  $y = 0.0451, 0.2595, 0.5248, \text{ and } 0.7824$  inches. Recall that the top and bottom patch edges are located at  $y = \pm 0.515$  inches and the left and right patch edges are located at  $x = \pm 0.435$  inches. The numerical strains were determined using the nodal displacement data as described in the previous chapter.

#### **4.3.3.1 $\epsilon_x$ strain data**

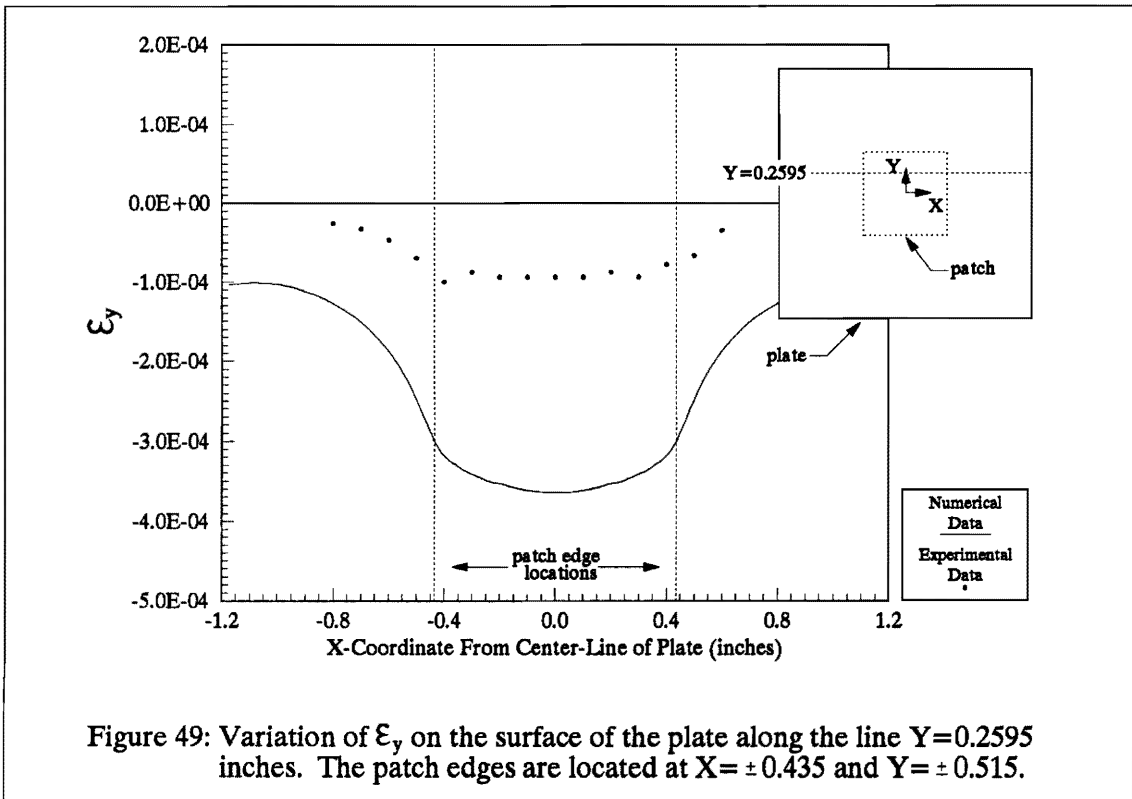
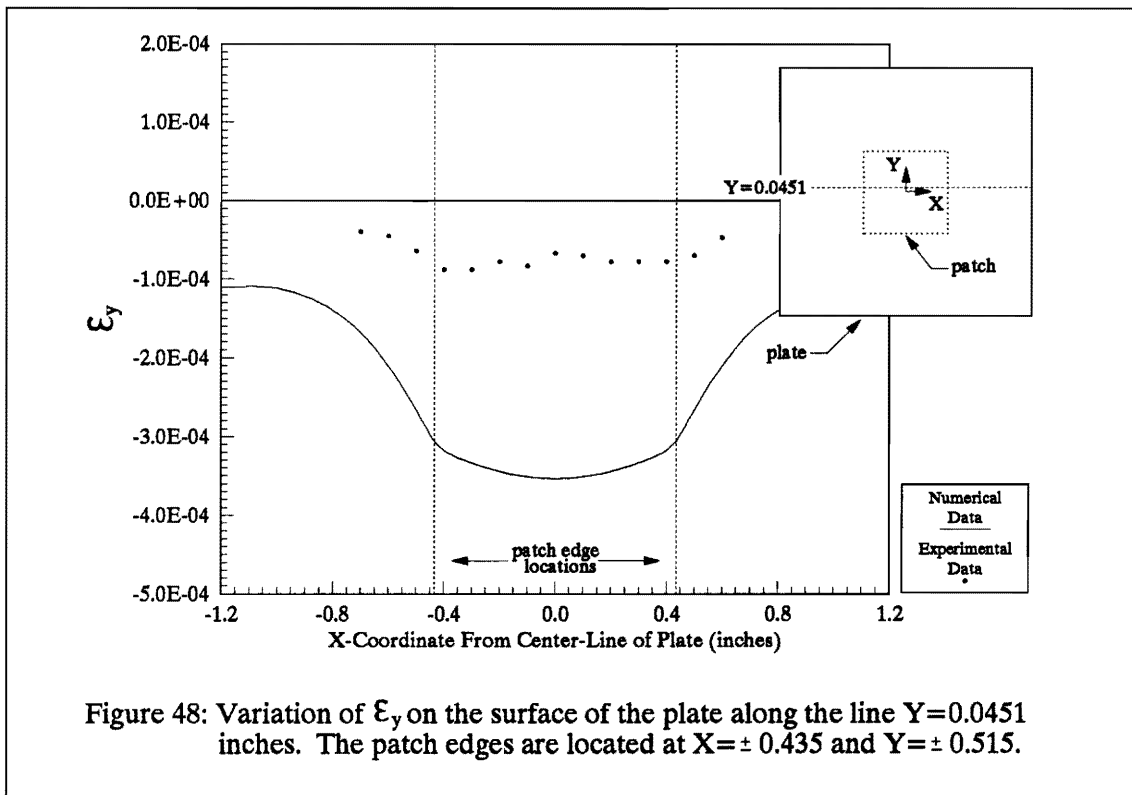
Comparisons of the numerical and experimental variations of  $\epsilon_x$  on the plate surface are shown in Figures 44-47. Clearly, the magnitude of the numerical and experimental data are quite different, as discussed previously. The experimentally induced strains generally follow the same trends as predicted by the finite element analysis, but are of approximately 1/3 the magnitude. The numerical variations of  $\epsilon_x$  are very similar to the variations of  $\epsilon_x$  presented in the previous chapter, except for the oscillations located over the patch edges and the flatness of the strain variations between the patch boundaries. The maximum predicted compressive strain of  $-0.000380$  occurs over the patch and is approximately 60% of the applied free patch strain of  $-0.000639$ .





#### **4.3.3.2 $\epsilon_y$ strain data**

Numerical and experimental variations of  $\epsilon_y$  on the surface of the plate are presented in Figures 48-51. The variations of experimentally induced strain in Figures 48 and 49 follow the same trends as the numerical data, but are of a much lower magnitude. The sporadic nature of the both the numerical and experimental strain variations seen in Figure 50 is evident. In the case of the numerical data, the strains are calculated over an area where oscillations are prevalent due to the proximity of the underlying patch edge. In the experimental case, the sporadic poorly matching results are due to the difficulty in analyzing a fringe pattern along the border of a closed loop fringe. The closed loop fringe is visible in the top half of the fringe pattern in Figure 42b. The sparseness of fringes across the line at  $y = 0.7824$  leads to only a few data points, but these follow the same trends as the numerical data and are of a lesser magnitude. Note that within the projected patch boundaries, the strain is tensile. As discussed before, this is caused by the plate material resisting the patch contraction by pulling against it, resulting in tensile strain.



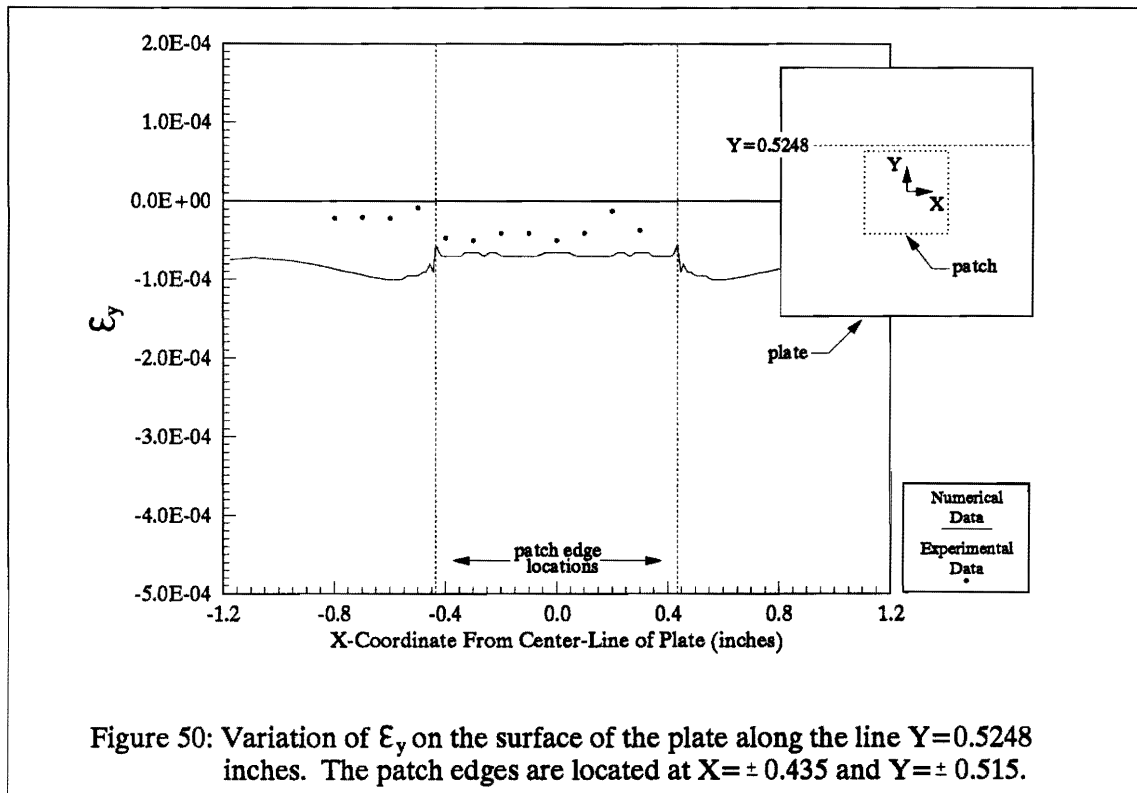


Figure 50: Variation of  $\epsilon_y$  on the surface of the plate along the line  $Y=0.5248$  inches. The patch edges are located at  $X=\pm 0.435$  and  $Y=\pm 0.515$ .

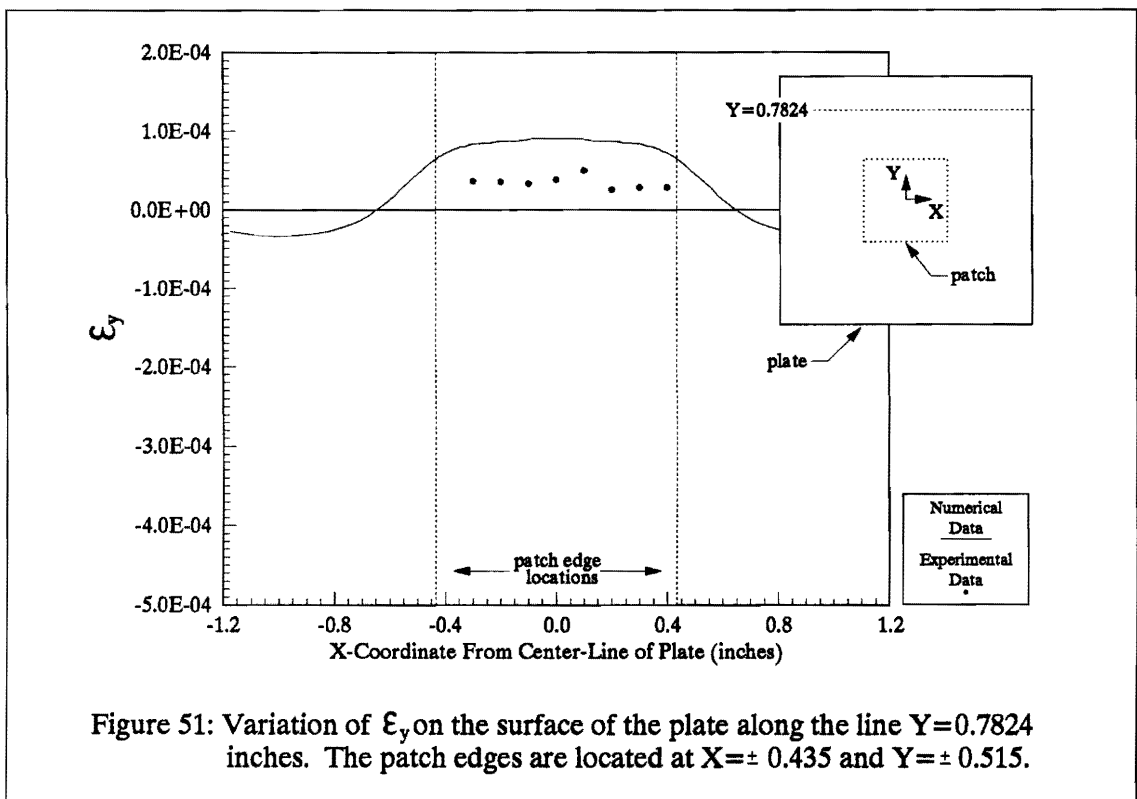
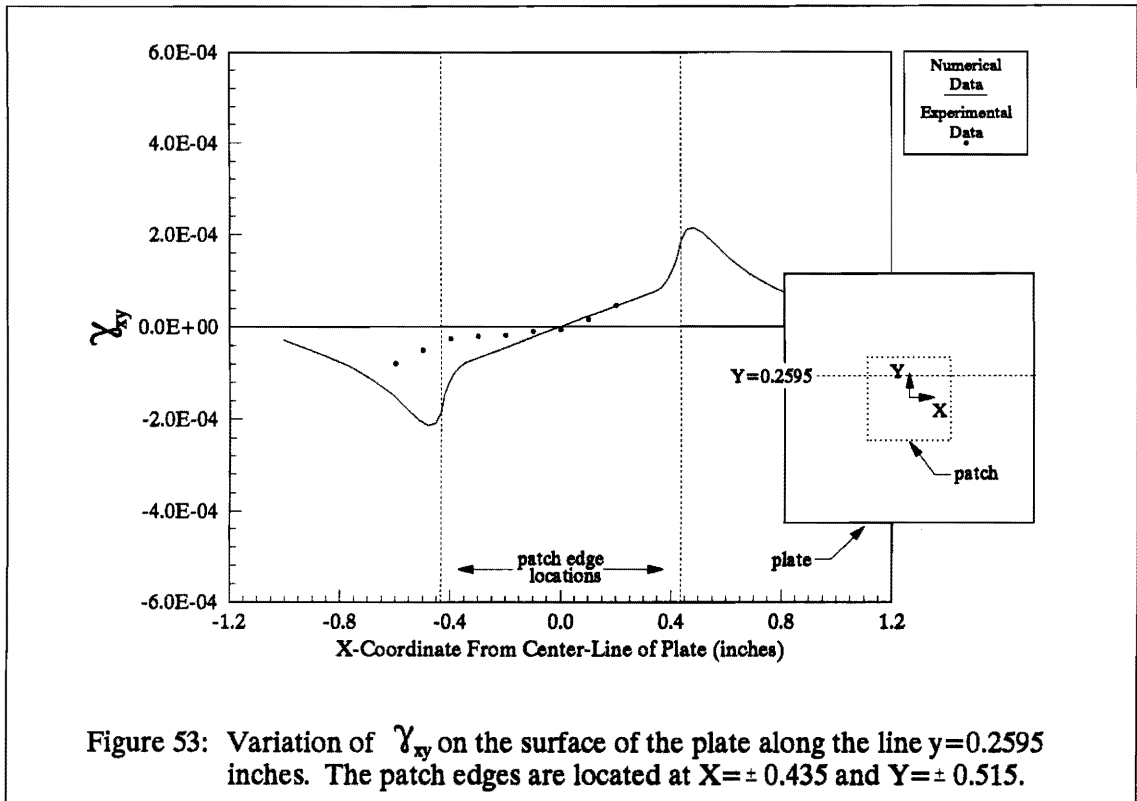
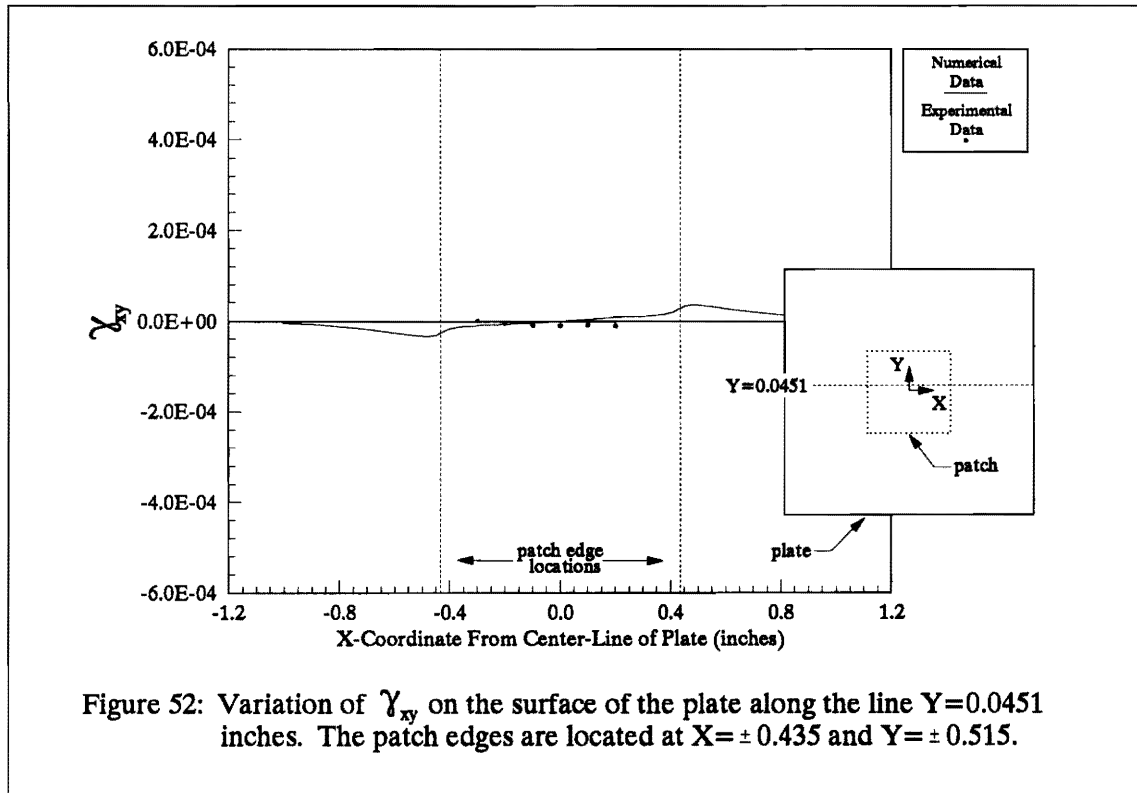


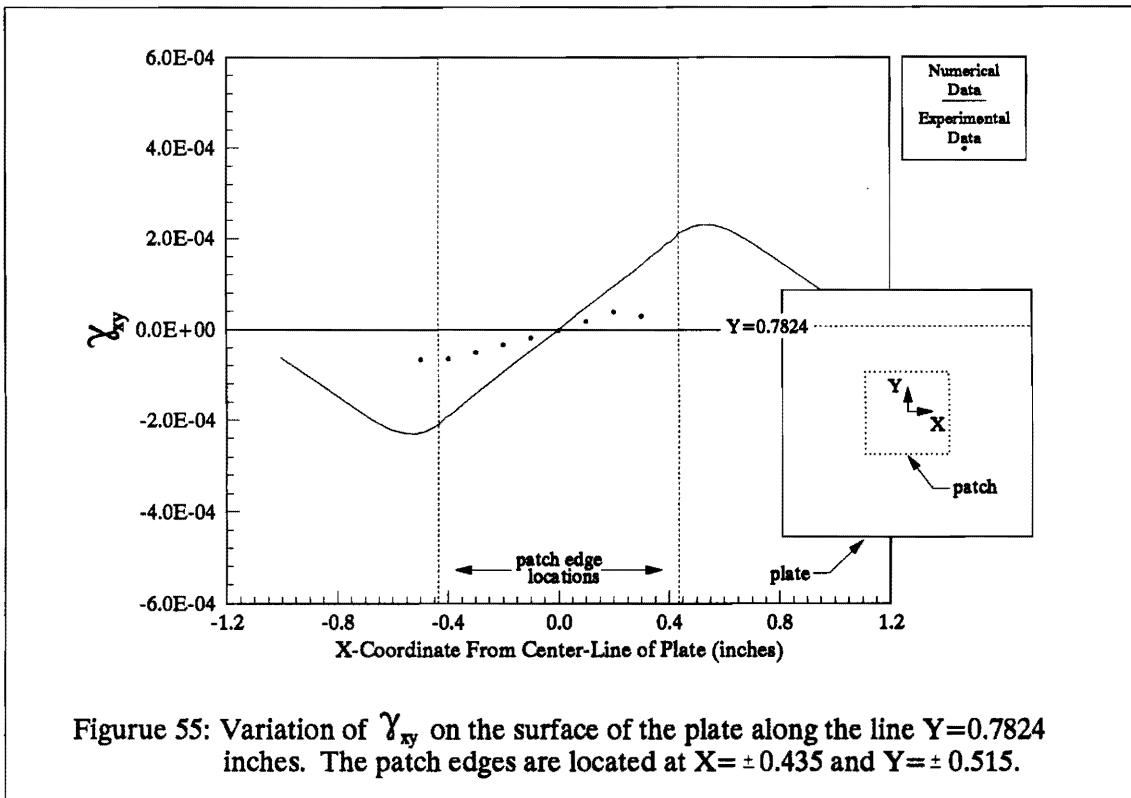
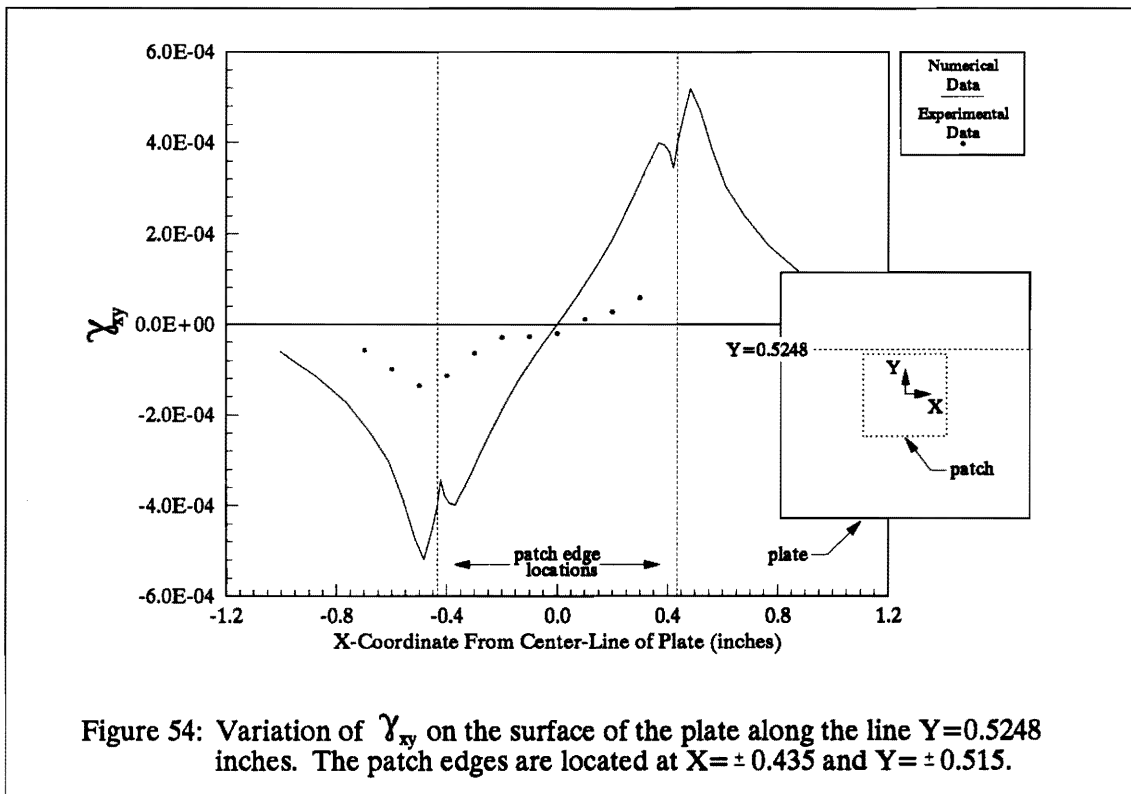
Figure 51: Variation of  $\epsilon_y$  on the surface of the plate along the line  $Y=0.7824$  inches. The patch edges are located at  $X=\pm 0.435$  and  $Y=\pm 0.515$ .

#### **4.3.3.3 $\gamma_{xy}$ strain data**

Experimental and numerical variations of  $\gamma_{xy}$  across the surface of the plate are plotted in Figures 52-55. The shear strain across the line  $y = 0.0451$  inches should be nearly zero, as seen in Figure 52. The shear would be zero at  $y = 0.0$  inches. The small number of experimental data points is a result of the difficulty of analysis of the cross derivative,  $\delta u / \delta y$ , across this particular line. The experimental variation of the in-plane shear in Figures 53-55 generally follow the same trends as the variation predicted numerically, but again are of a lower magnitude. A double peak in the numerical data occurs in Figure 54 across the projected patch boundary and is caused by the proximity of the patch corner. Maximum shear strains in this figure are on the order of 0.000520.







#### **4.3.4 Finite Element Strain Results Near the Surface and Mid-Plane of the Plate**

As before, the finite element analysis calculated strain data at the Gauss points. The following sections examine the variation of  $\epsilon_x$ ,  $\gamma_{xy}$ ,  $\epsilon_z$ , and  $\gamma_{xz}$  on two planes of Gauss points parallel to the x-y plane. These planes are located near the mid-plane and surface of the plate at  $z = 0.0005$  inches and  $z = 0.0452$  inches, respectively. The layer of Gauss points near the mid-plane includes elements modeling piezoceramic material as well as elements modeling PC-10C plate material. The strain variations  $\epsilon_y$  and  $\gamma_{yz}$  were omitted due to their similarity to the variations of  $\epsilon_x$  and  $\gamma_{xz}$  when rotated about the z-axis by 90 degrees. In contrast to the previously examined model, these strain components were not identical due to the non-square, rectangular shape of both the plate and patch.

##### **4.3.4.1 In-Plane Strains**

Variations of  $\epsilon_x$  near the plate surface and mid-plane are shown in Figures 56 and 57, respectively. The variation of strain near the surface is fairly smooth, with only one large oscillation near the right patch edge. Recall that the right and top patch boundaries occur at  $x = 0.435$  and  $y = 0.515$  inches, respectively. The strain is negative near the coordinate system origin with a magnitude near  $-0.000380$ , approximately 60% of the applied in-plane free patch strain of  $-0.000639$ . A gentle, tensile peak occurs in Figure 56 outside of the right patch boundary and has a magnitude of approximately  $0.000145$ . In Figure 57, the gentle tensile peak becomes a sharp ridge of strain just outside of the right patch boundary. As the patch boundary is approached, the strain first becomes more negative and then rapidly peaks to a tensile value of approximately  $0.001000$ . The maximum negative value approaches the applied in-plane free patch strain. Variations of  $\epsilon_x$  near the surface and mid-plane are nearly identical except in the regions surrounding the right patch boundary.

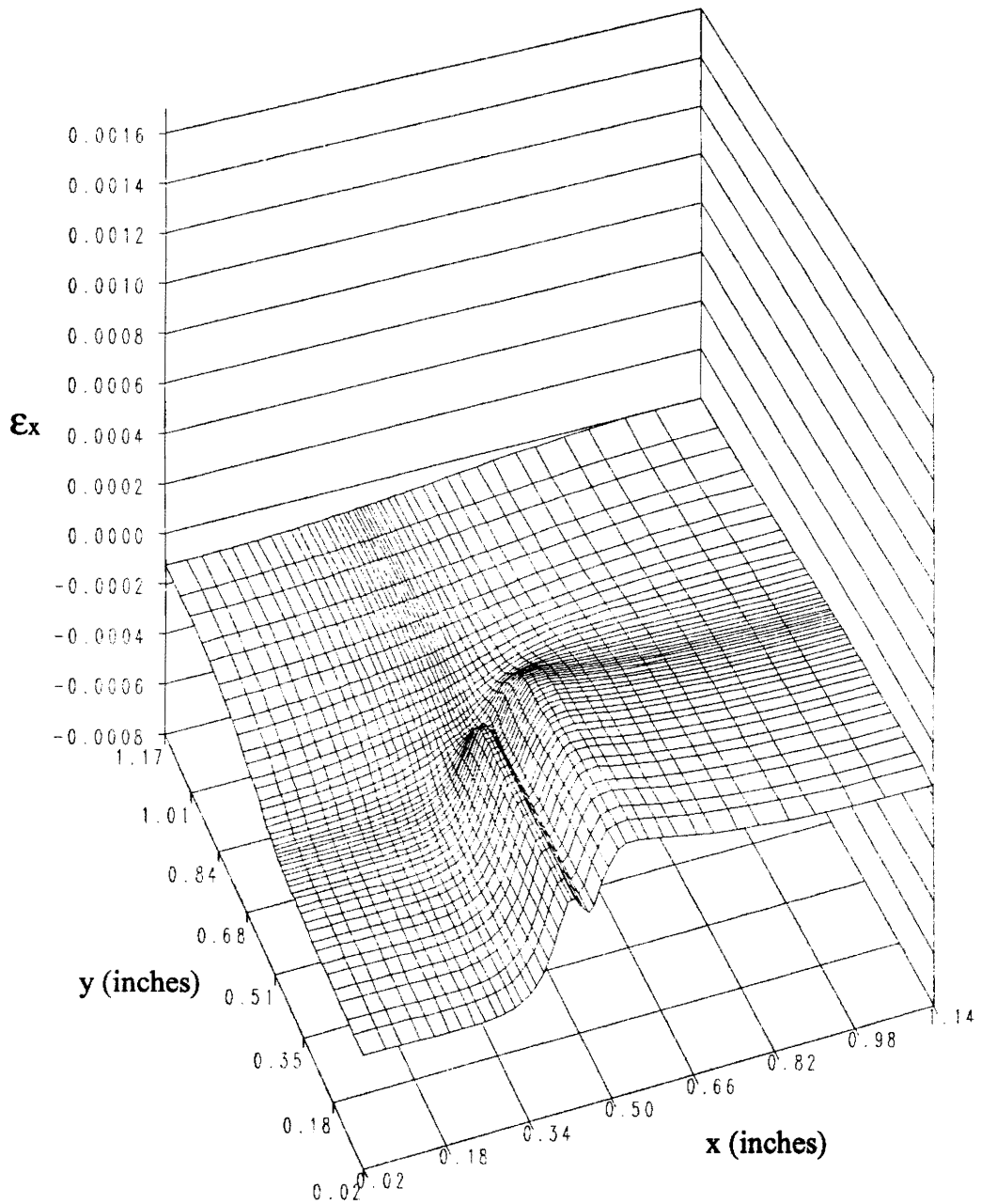


Figure 56: Variation of  $\epsilon_x$  on the plane of Gauss points nearest the plate surface of the embedded piezoceramic patch specimen.

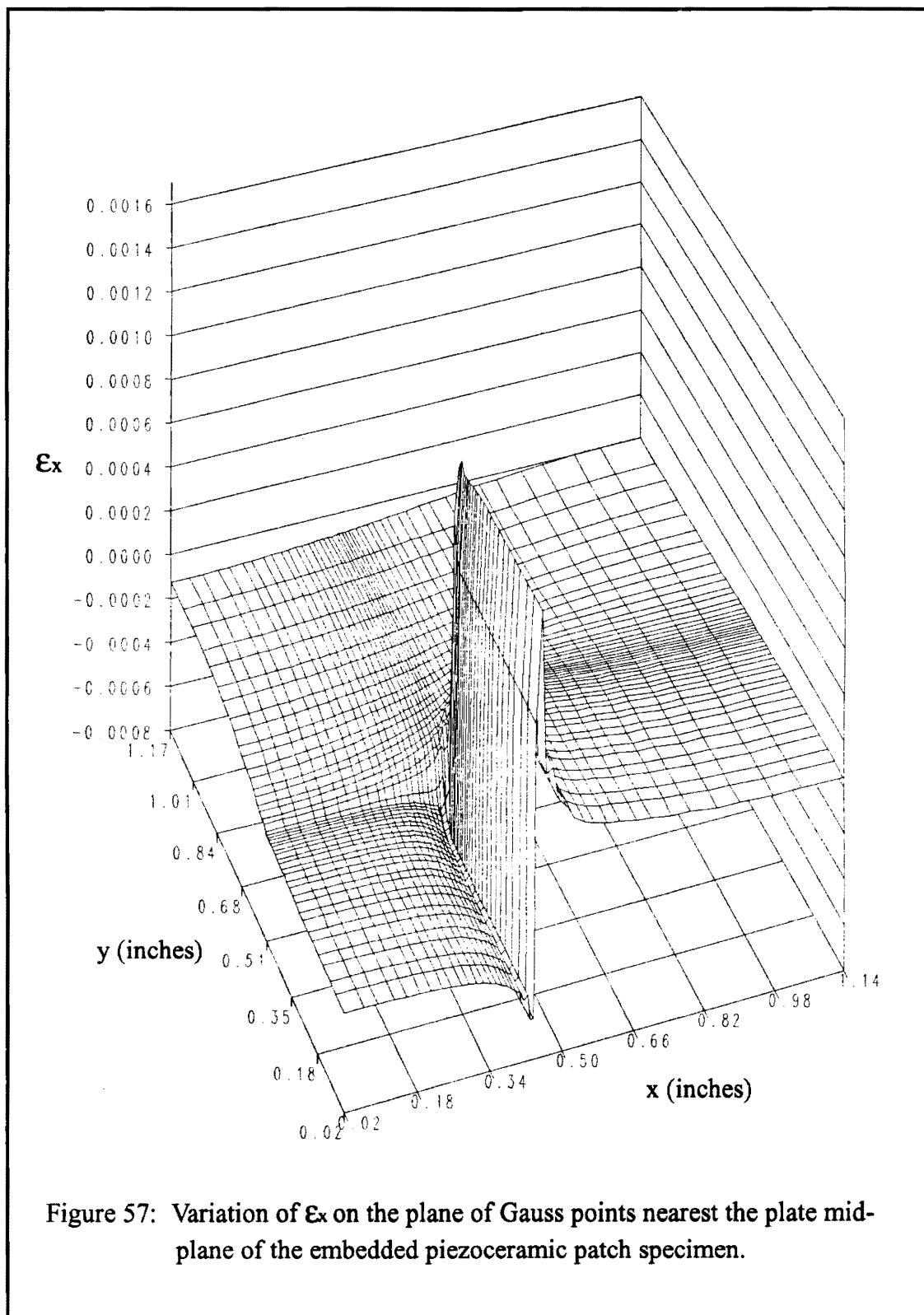


Figure 57: Variation of  $\epsilon_x$  on the plane of Gauss points nearest the plate mid-plane of the embedded piezoceramic patch specimen.

The variations of in-plane shear strain,  $\gamma_{xy}$ , near the specimen surface and mid-plane are presented in Figures 58 and 59. Near the plate surface, the variation is again smooth with a gentle, positive peak occurring near the patch corner and outside of the patch boundaries. This peak has a maximum value of 0.000575. The variation of shear near the mid-plane gradually increases as the patch edges are approached. Near the patch edge, the shear begins to decrease at a slight rate near the coordinate axes and at a rapid rate near the patch corner. On the line of Gauss points just outside of the patch boundary, the shear jumps abruptly higher, peaking at 0.003266 at the patch corner. As with  $\epsilon_x$ , the variations of  $\gamma_{xy}$  near the plate surface and mid-plane are nearly identical, except in the regions around the patch boundaries and especially near the patch corner.

The large peaks in Figures 57 and 59 demonstrate the singular nature of the intersection of patch edge with the plate material. The oscillations in the strain results could be reduced by refining the mesh in the areas surrounding the patch.

#### **4.3.4.2 Out-of-Plane Strains**

Variations of  $\epsilon_z$  near the plate surface and mid-plane are plotted in Figures 60 and 61. Near the surface,  $\epsilon_z$  is nearly constant over the face of the patch at a value of 0.000448, gradually decreasing toward the patch boundary. As the boundary is approached,  $\epsilon_z$  decreases more rapidly, then increases, and finally decreases again to a nearly constant value approaching zero at the plate corner. At the mid-plane,  $\epsilon_z$  is again nearly constant, with a values ranging from 0.002381 to 0.002418. This plateau, viewed in Figure 61, occurs within the elements modeling the piezoceramic material and is only slightly less than the applied out-of-plane strain of 0.002595. This demonstrates that the plate material is barely resisting the out-of-plane expansion of the patch. Just inside the patch boundary, the strain jumps to form a ridge around the plateau region with values of approximately 0.002530, peaking at the patch corner at 0.002648. Outside of the patch

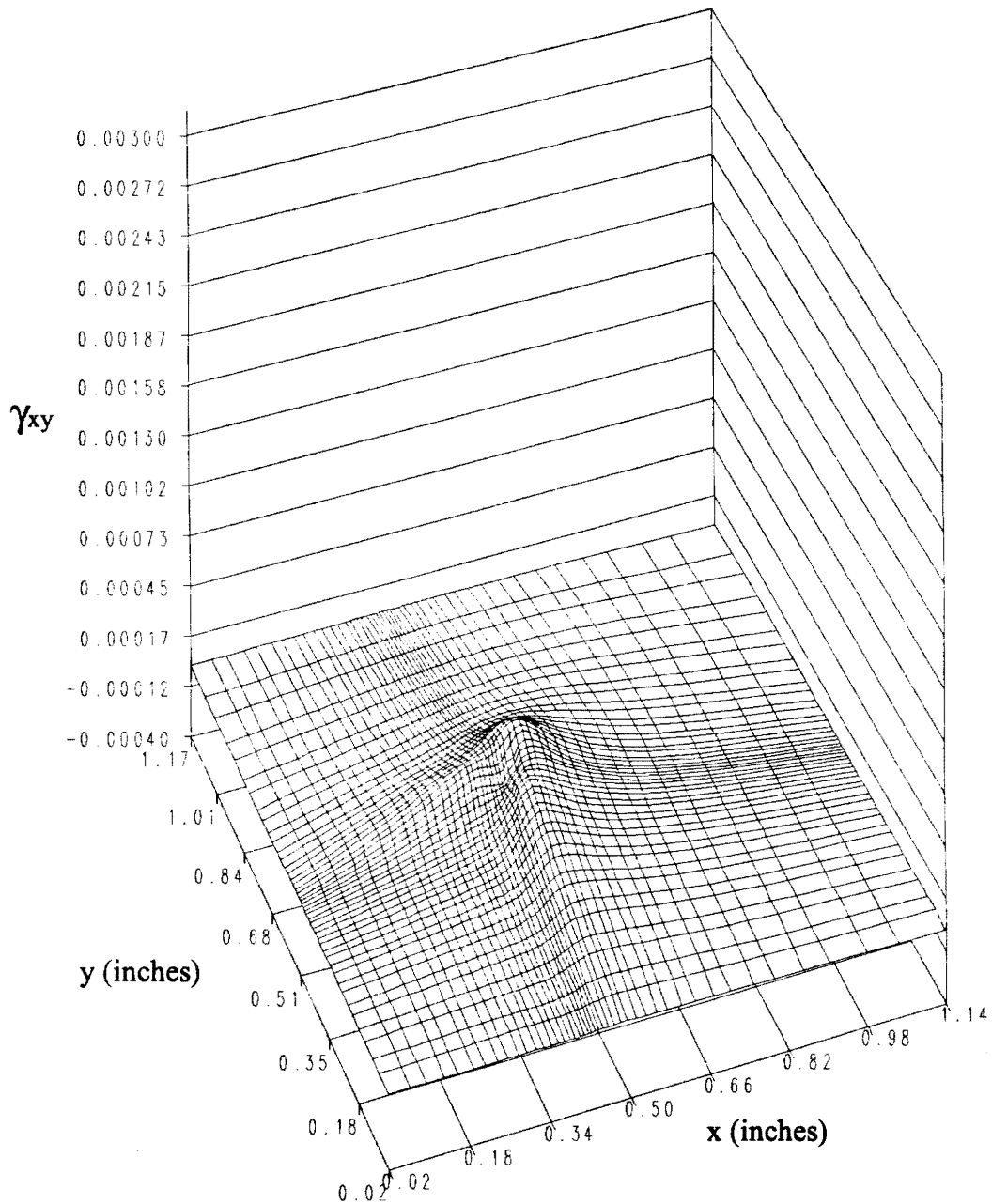


Figure 58: Variation of  $\gamma_{xy}$  on the plane of Gauss points nearest the plate surface of the embedded piezoceramic patch specimen.

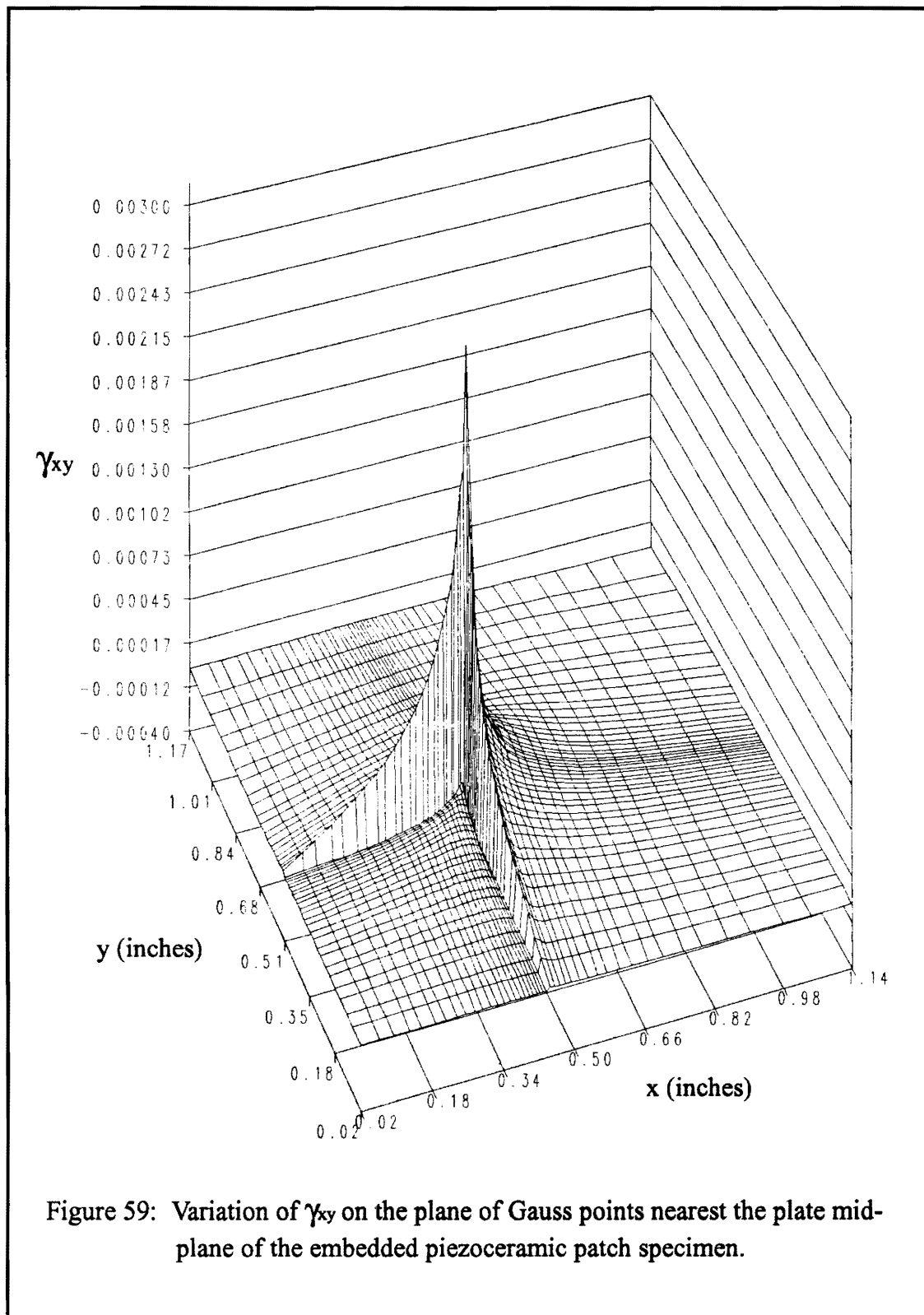


Figure 59: Variation of  $\gamma_{xy}$  on the plane of Gauss points nearest the plate mid-plane of the embedded piezoceramic patch specimen.



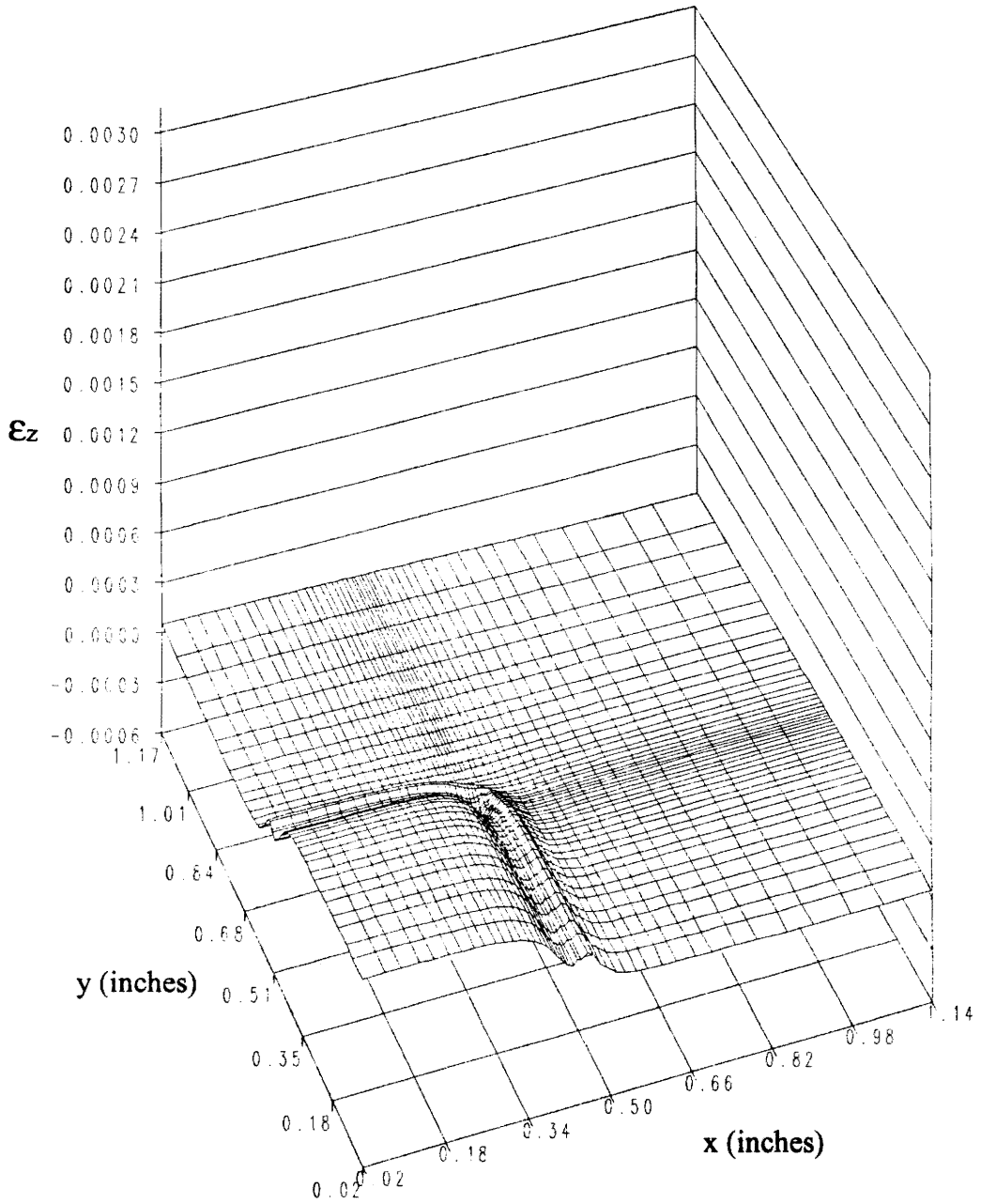


Figure 60: Variation of  $\epsilon_z$  on the plane of Gauss points nearest the plate surface of the embedded piezoceramic patch specimen.

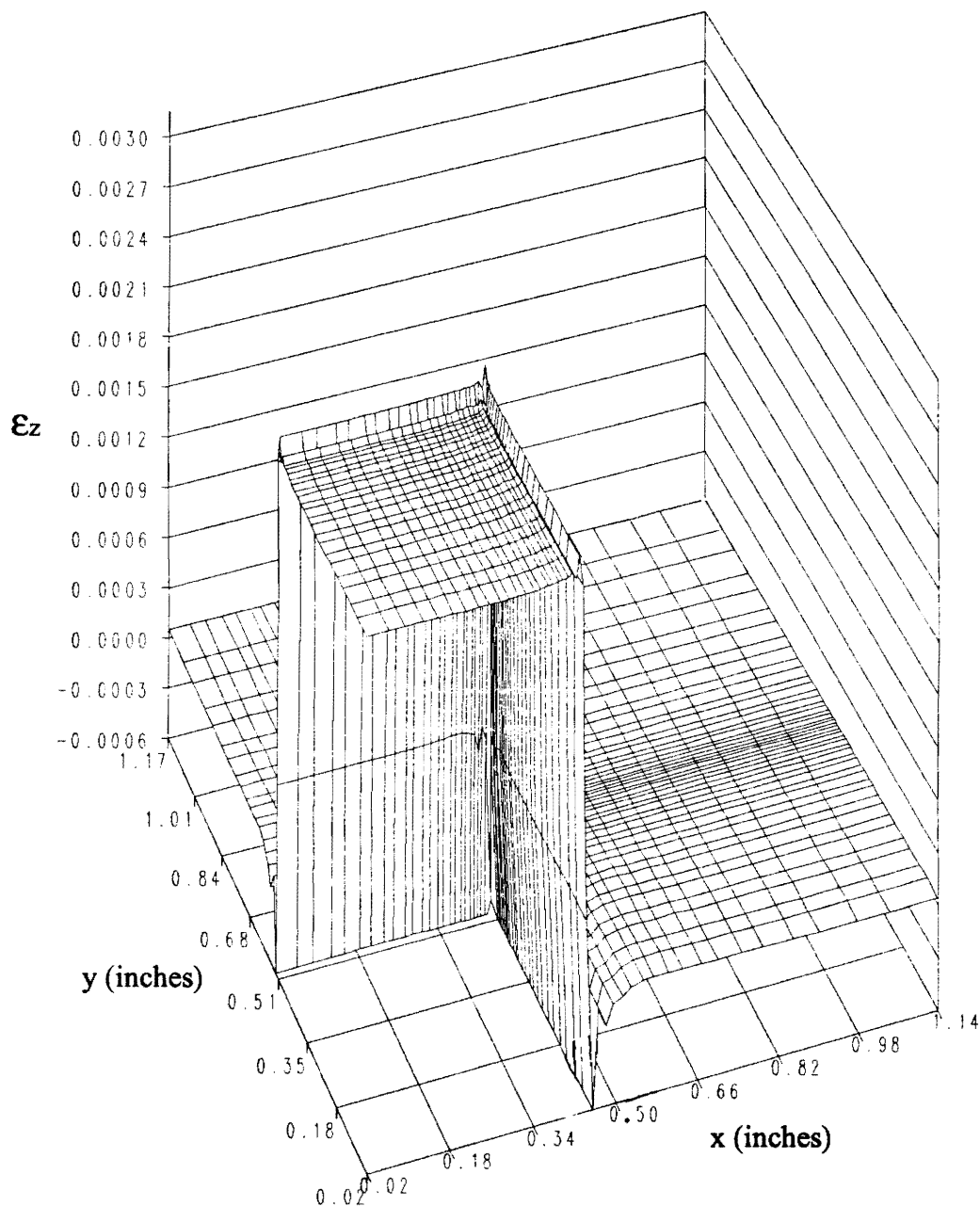


Figure 61: Variation of  $\epsilon_z$  on the plane of Gauss points nearest the plate mid-plane of the embedded piezoceramic patch specimen.

boundaries, the strain drops rapidly to a value of -0.000691 and then climbs to level out at a value near zero. As before, the variations of  $\epsilon_z$  near the mid-plane and surface are almost identical except, however, in the region of the patch as a whole, not just in the patch edge region.

The variations of  $\gamma_{xz}$  are shown in Figures 62 and 63. It is demonstrated in both figures that the out-of-plane shear is essentially zero, except for small variations located at the right edge of the patch. Near the surface, the values range from -0.000084 to 0.000095, while near the mid-plane, the values of  $\gamma_{xz}$  range from -0.000052 to 0.000175.

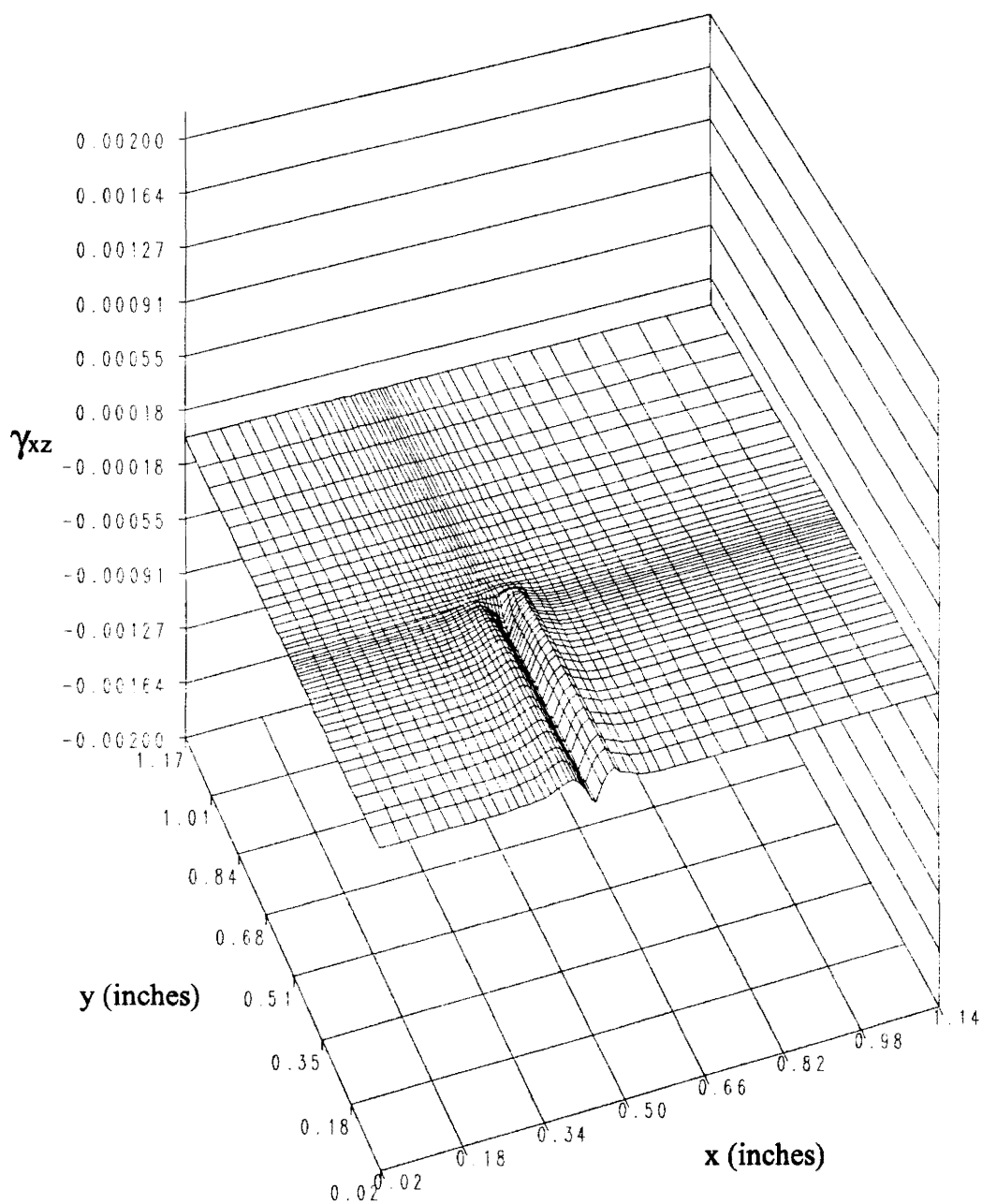


Figure 62: Variation of  $\gamma_{xz}$  on the plane of Gauss points nearest the plate surface of the embedded piezoceramic patch specimen.

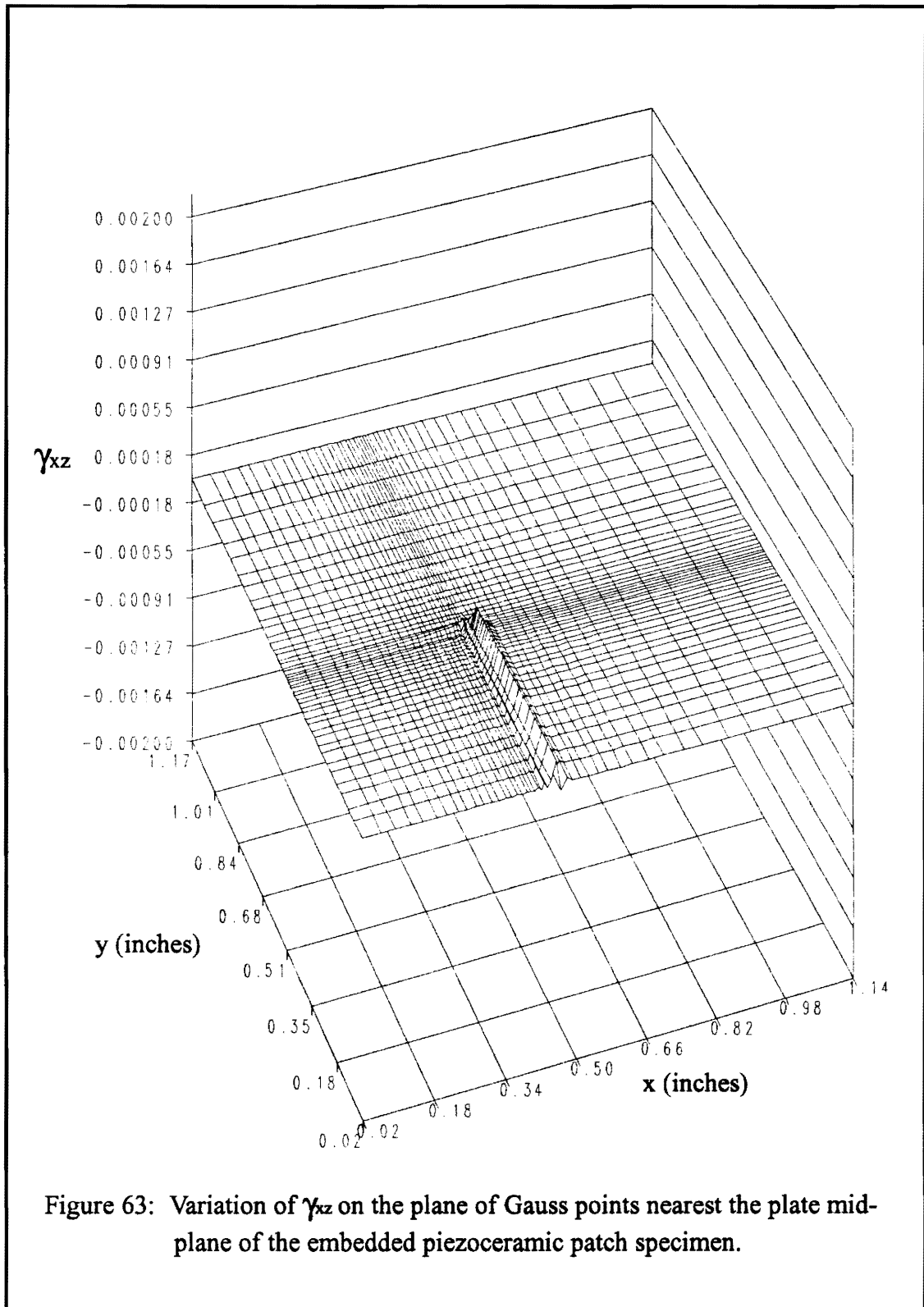


Figure 63: Variation of  $\gamma_{xz}$  on the plane of Gauss points nearest the plate mid-plane of the embedded piezoceramic patch specimen.

### 4.3.5 Stress Results Near the Specimen Mid-Plane

As in the previous chapter, Hooke's Law was employed to calculate the stresses at the Gauss points using the finite element calculated strain data. The only difference occurred with the elements modeling the patch material. Hooke's Law was modified to subtract the free thermal strain applied to these elements. Variations of  $\sigma_x$ ,  $\sigma_z$ ,  $\tau_{xy}$ , and  $\tau_{xz}$  on the plane of Gauss points near the mid-plane of the embedded piezoceramic/plate specimen are shown in Figures 64-67.

The variation of  $\sigma_x$  near the specimen mid-plane is plotted in Figure 64. Within the patch boundaries,  $\sigma_x$  is strongly tensile, with a maximum value of 3533 psi approximately 0.1 inches from the top edge of the patch. There exist slight oscillations at the top and right edges of the patch. The boundary between the piezoceramic material of the patch and the epoxy material of the plate occurs just before the stress variation begins to level out. Outside the top patch boundary,  $\sigma_x$  has values ranging around -100 psi, decreasing to approximately -50 psi at the top edge of the plate. As expected to satisfy the requirements of a free edge,  $\sigma_x$  approaches zero at the right edge of the plate.

The variation of  $\sigma_z$  is shown in Figure 65. The most prominent feature is the band of oscillatory stress located at the patch boundaries. Over most of the boundary,  $\sigma_z$  ranges between -1400 psi and 750 psi with peak values of -3500 psi and 1540 psi at the patch corner. The large number and magnitude of oscillations clearly demonstrates the presence of a singularity and the need for mesh refinement at the patch borders. Over most of the patch and outside of the patch boundaries,  $\sigma_z$  is essentially zero.

Variations of  $\tau_{xy}$  on the plane of Gauss points near the mid-plane of the embedded patch specimen are shown in Figure 66. The shear increases from zero at the center of the patch, to a peak value of 1100 psi near the corner of the patch. At the first row of

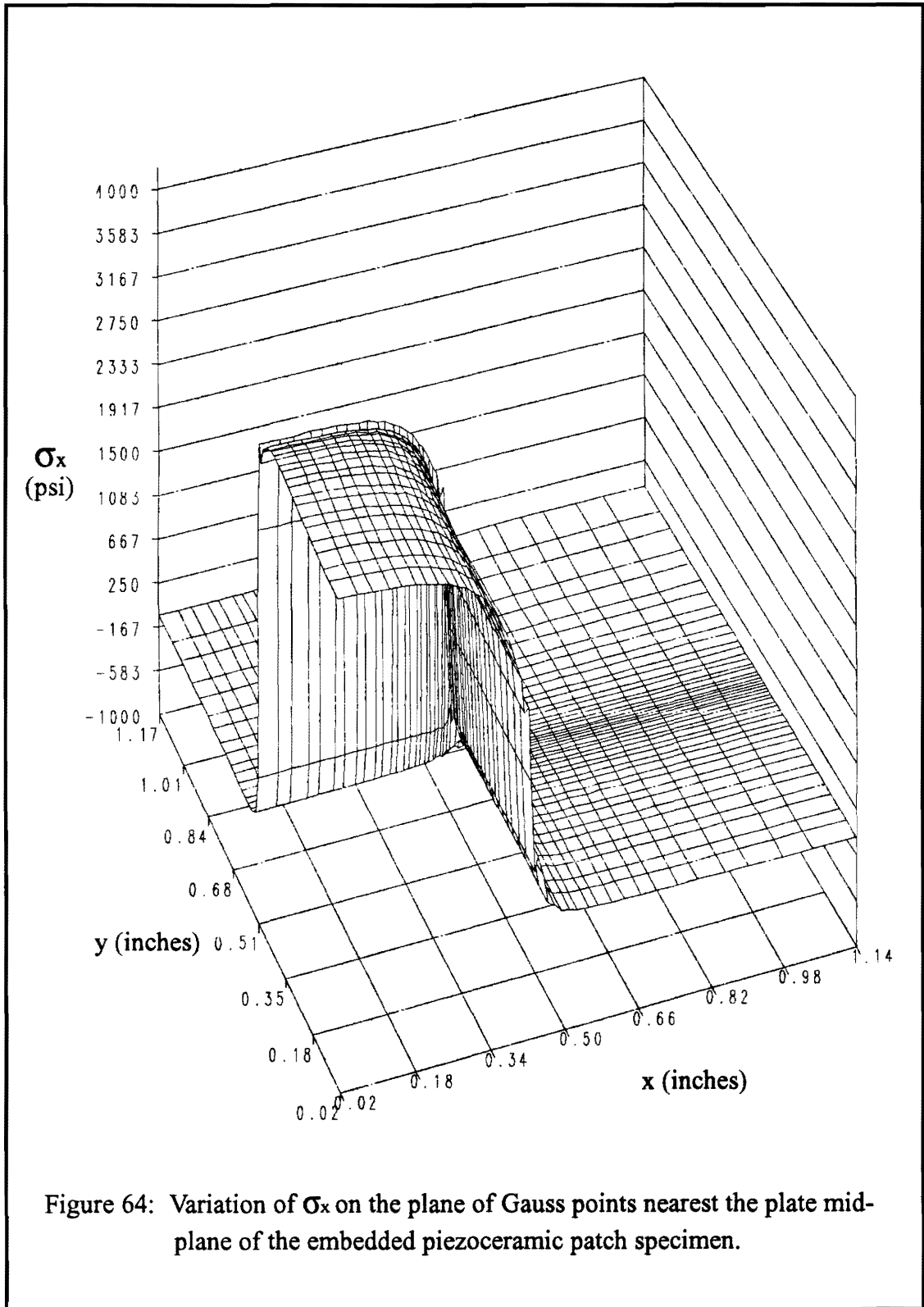


Figure 64: Variation of  $\sigma_x$  on the plane of Gauss points nearest the plate mid-plane of the embedded piezoceramic patch specimen.

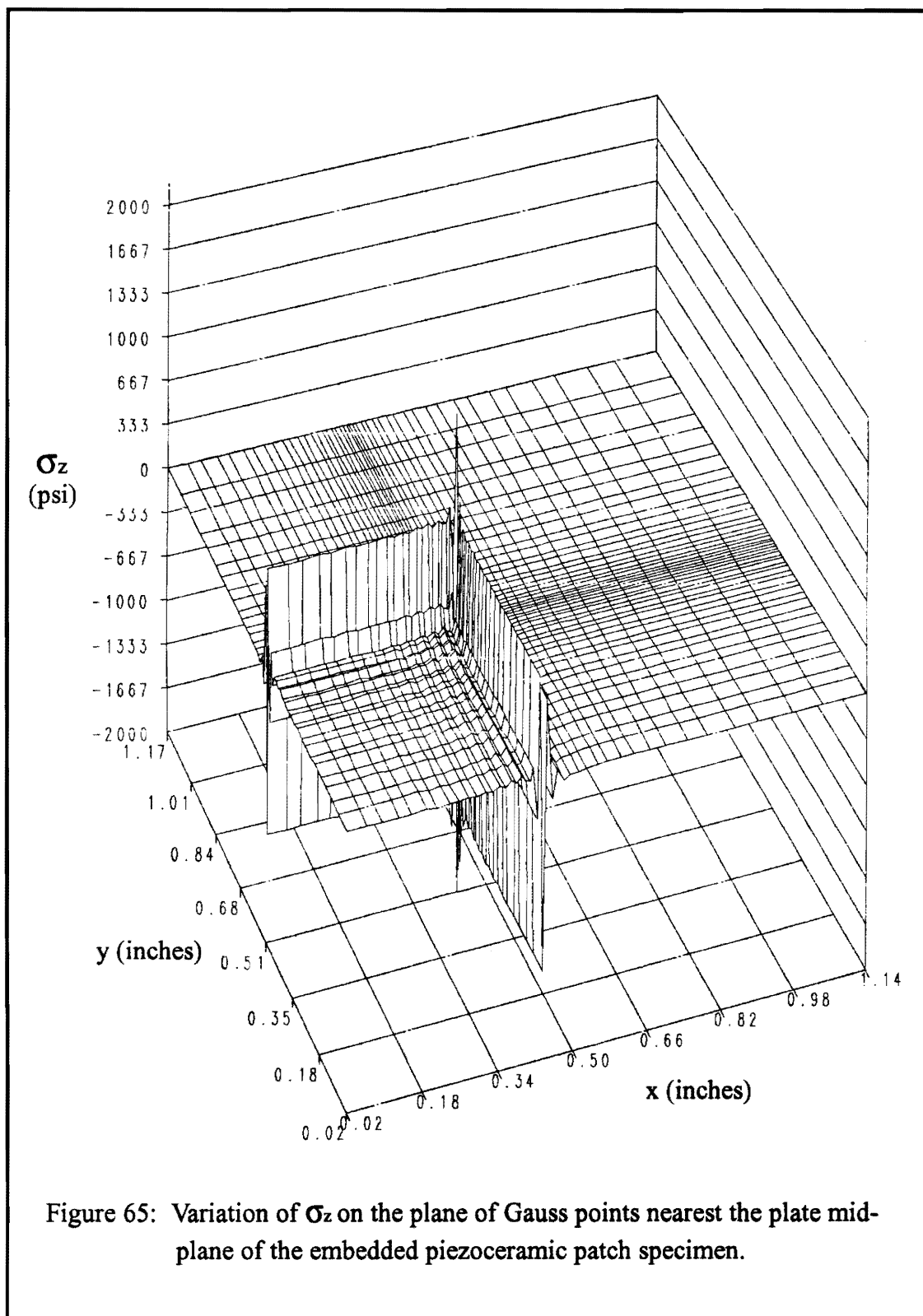


Figure 65: Variation of  $\sigma_z$  on the plane of Gauss points nearest the plate mid-plane of the embedded piezoceramic patch specimen.



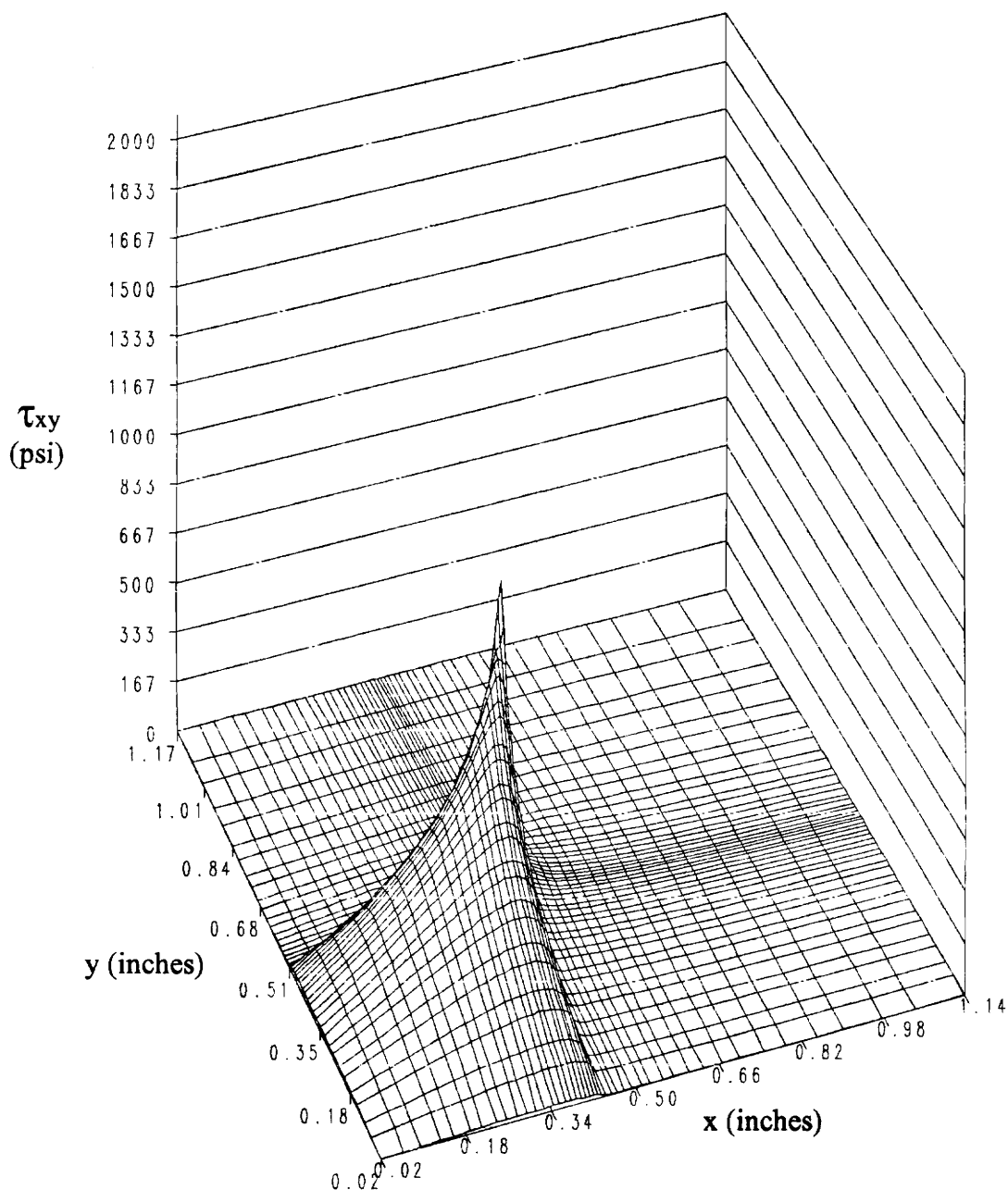


Figure 66: Variation of  $\tau_{xy}$  on the plane of Gauss points nearest the plate mid-plane of the embedded piezoceramic patch specimen.

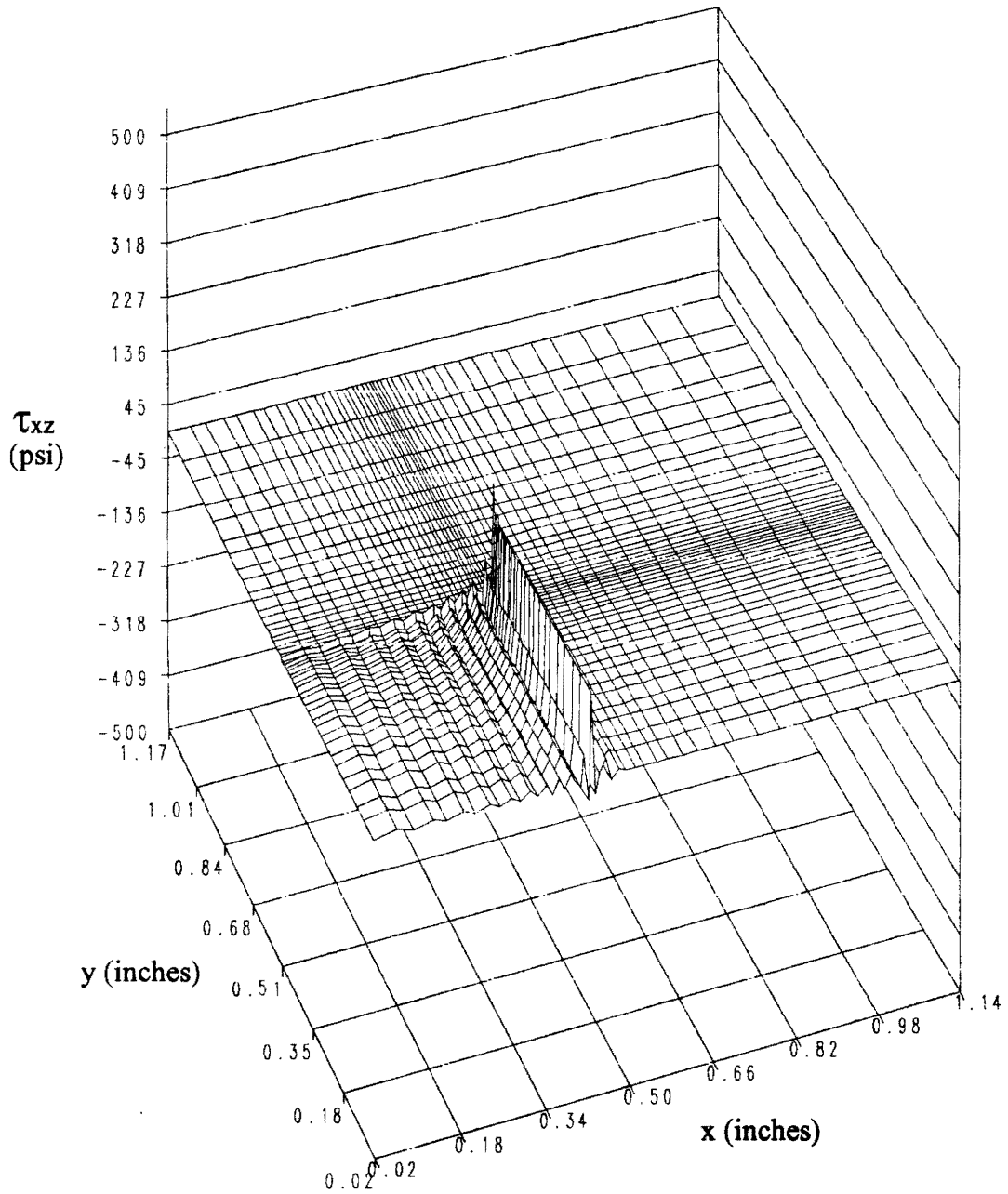


Figure 67: Variation of  $\tau_{xz}$  on the plane of Gauss points nearest the plate mid-plane of the embedded piezoceramic patch specimen.

Gauss points outside the elements modeling the piezoceramic material, the shear drops to approximately zero near the patch center and 300 psi near the patch corner. As the specimen edges are approached,  $\tau_{xy}$  approaches zero as expected.

The variation of  $\tau_{xz}$  on the layer of Gauss points near the mid-plane of the specimen is plotted in Figure 67. Within the elements modeling the piezoceramic material, the shear is zero near the y-coordinate axis. It becomes increasingly oscillatory as the right patch edge is approached. The maximum stress value at the patch edge is 200 psi. Outside the patch boundaries,  $\tau_{xz}$  is essentially zero.

The levels of stress resulting from this analysis are much higher within the elements modeling the piezoceramic material than within the elements modeling the epoxy plate. This is to be expected due to the significantly higher stiffness of the piezoceramic material when compared with the epoxy. The maximum compressive and tensile normal stresses of the G-1195 piezoceramic material is published at -75000 psi and 11000 psi, respectively. No maximum shear stress data was published. The maximum value of  $\sigma_x$  within the piezoceramic material was 3533 psi, approximately 32% of the maximum tensile strength value. The maximum tensile and compressive values of  $\sigma_z$  were 1540 psi and -3500 psi, respectively. Due to the presence of a singularity and the lack of mesh refinement at the patch edge, the values of  $\sigma_z$  calculated cannot be fully trusted. The maximum value of  $\sigma_x$  is more likely to be valid since it occurs 0.1 inches from the top patch edge. Statically, the maximum value of  $\sigma_x$  is not critical, but over many loading cycles, this level of stress will present a fatigue problem within the piezoceramic material.

If a patch were embedded between two layers of a fiber reinforced composite laminate, the induced out-of-plane or interlaminar stresses would be of great interest. Since the interlaminar strength of a composite laminate is generally much lower than the

in-plane strength, the successful use of embedded piezoceramic patches as actuators may hinge on the magnitude of the induced out-of-plane stresses. The results from this analysis indicated that the interlaminar stresses are quite low, except in the region of the patch edge. Although the specimen examined in this research is not a fiber reinforced composite, the interlaminar behavior should be similar. The proper calculation of these interlaminar stresses in a fiber reinforced composite would require proper refinement of the finite element mesh. It is unclear whether refinement of the mesh within the plane of the plate would be adequate. Refinement of the number of elements through the plate and patch thickness may also be necessary.

## **Chapter 5: Conclusions and Recommendations**

### **5.1 Conclusions**

The primary objective of this research was to examine the induced strain of actuation of piezoceramic patches, embedded and surface mounted, using moiré interferometry and a three-dimensional finite element model, and to evaluate the usefulness of each technique when applied to this subject. The characterization of the voltage/strain response of a free piezoceramic patch was a secondary goal, needed to complete the main objectives. To accomplish these goals, two piezoceramic patch/plate specimens were examined with moiré interferometry and a commercially available finite element analysis program. Moiré interferometry experiments and a Twyman-Green interferometry experiment were conducted on several free piezoceramic patch specimens for voltage/strain characterization. The conclusions drawn from this study are:

- 1) The in-plane piezoceramic voltage/strain response is nearly linear, except in the lower voltage range. When compared to the published response, the experimentally obtained response was much higher in magnitude. The published data is, on average, 40% lower than the experimental voltage/strain response.
- 2) The out-of-plane piezoceramic voltage/strain response is non-linear. The published response is linear and has a much lower magnitude. At 100 volts, the magnitude of the published data is approximately 35% of the experimental data, while at 343 volts the magnitude of the published data is 20% of the experimental data.

- 3) The excellent match between the finite element analysis of the surface bonded piezoceramic patch specimen and the moiré interferometry experiments verifies the finite element modeling technique of inducing patch actuation by manipulating the temperature and coefficients of thermal expansion.
- 4) The poor match between the experimental and finite element results for the embedded patch specimen are probably due to a combination of the off centered location of the patch and the partial depoling of the patch.
- 5) The nearly identical behavior of mid-plane and surface strains away from the patch boundaries indicated that a two-dimensional finite element analysis would be adequate for examining the far field induced strains of actuation.
- 6) The patch edges are singularities due to the geometry of the specimens and the large stiffness differences between patch and plate material. This is demonstrated by the stress and strain results from the finite element analysis and, to a lesser degree, the strain results from the moiré interferometry experiments.
- 7) Due to the singular nature of the patch edges, the finite element analysis requires a highly refined mesh in the region of the patch edges. It is clear from this research that the meshes used in the two analyses need to be refined before the stress and strain results along the patch edges can be fully trusted. It is not clear whether the mesh refinements need to be carried out within the plane of the plate, or whether an increased number of elements through the plate and patch thicknesses are necessary.
- 8) The only significant components of stress at the plate edges are  $\sigma_x$  and  $\sigma_y$ . Along the top plate edge, the induced  $\sigma_x$  is approximately -40 psi and -50 psi for the surface bonded patch and embedded patch specimens, respectively. All other stress

components along this edge are zero. Similar results for  $\sigma_y$  are seen along the right plate edge.

- 9) The peel tendencies of the surface bonded patch could present a fatigue problem depending on the fatigue characteristics of the bonding adhesive, as well as the substrate material. Large tensile stresses present within the embedded patch itself will represent long term fatigue problems.
- 10) Moiré interferometry is an excellent method for studying the far field induced strains of actuation and verifying finite element analyses. The difficulty of replicating a diffraction grating close enough to a patch edge to resolve the high strain gradients in this area prevents moiré interferometry from effectively examining the singular nature of the patch edge.
- 11) Although the three-dimensional finite element models are large, and properly refined models could be significantly larger, use of such models is invaluable in examining the response of a piezoceramic actuated intelligent structure in regions near patch edges.

## 5.2 Recommendations

Several recommendations for future studies can be made. These recommendations focus on the factors effecting the future use of piezoceramic patches as actuating material.

- 1) The in-plane and out-of-plane voltage/strain response of a free piezoceramic patch should be examined with the voltage being applied opposite to the poling voltage.

It is essential to learn the levels of voltage that can be used without depoling the patch.

- 2) The voltage/strain characteristics of a depoled or partially depoled patch after *in situ* repoling must be determined if depoling cannot be avoided in a design at all times.
- 3) For use with fiber reinforced composite materials, the interlaminar stresses induced by an embedded piezoceramic actuator need to be examined in detail.



## References

- Anders, W. S., Rogers, C. A., and Fuller, C. R., 1991, "Control of Sound Radiation From Shape Memory Alloy Hybrid Composite Panels By Adaptive Alternate Resonance Tuning," Proceedings of the Thirty Second AIAA/ASME/AHS/ASC Structures, Structural Dynamics & Materials Conference, Baltimore, MD.
- Braga, A., Honein, B., Barbone, P., and Herrman, G., 1990, "Active Suppression of Sound Reflection From a Submerged Plate," Proceedings of the First Joint U.S./Japan Conference on Adaptive Structures, Maui, HI, U.S.A.
- Crawley, E. F. and Anderson, E. H., 1990, "Detailed Models of Piezoceramic Actuation of Beams," *Journal of Intelligent Material Systems and Structures*, Vol. 1, pp 4-25.
- Crawley, E. F. and de Luis J., 1987, "The Use of Piezoelectric Actuators as Elements of Intelligent Structures," *AIAA Journal*, Vol. 25, No. 10, AIAA Paper 86-0878.
- Dehart, D. and Griffin, S., 1990, "Astronautics Laboratory Smart Structures/Skins Overview," Proceedings of the First Joint U.S./Japan Conference on Adaptive Structures, Maui, HI, U.S.A.
- Guo, Y., Post, D., and Czarnek, R., 1989, "The Magic of Carrier Fringes in Moiré Interferometry," *Experimental Mechanics*, Vol. 29, No. 2, pp 169-173.
- Ha, S., Keilers, C., and Chang, F., 1990, "Analysis of Laminated Composites Containing Distributed Piezoelectric Ceramics," Proceedings of the First Joint U.S./Japan Conference on Adaptive Structures, Maui, HI, U.S.A.
- Hickman, G. A., Gerardi, J. J., and Feng, Y., 1990, "Applications of Smart Structures to Aircraft Health Monitoring," Proceedings of the First Joint U.S./Japan Conference on Adaptive Structures, Maui, HI, U.S.A.
- Lazarus, K. B., Crawley E. F., and Bohlmann, J. D., 1990, "Static Aeroelastic Control Using Strain Actuated Adaptive Structures," Proceedings of the First Joint U.S./Japan Conference on Adaptive Structures, Maui, HI, U.S.A.
- MacNeal, R. H. and Harder, R. L., 1985, "A Proposed Standard Set of Problems to Test Finite Element Accuracy," *Finite Elements in Analysis and Design*, Vol 1, pp 3-20.
- Mollenhauer, D. H., Thompson, D. M., and Griffin, O. H. Jr., 1992, "Finite Element Analysis of Smart Structures," Proceedings of the Third International Conference on Computer Aided Design in Composite Material Technology, Newark, DE, U.S.A.

- "Piezoelectric Motor/Actuator Kit Manual," Piezo Systems, Inc., Cambridge, MA. 1990.
- Post D., 1987, "Moiré Interferometry," Chap. 7, *Handbook of Experimental Mechanics*, A.S. Kobayashi, ed., Prentice-Hall, Englewood Cliffs, NJ.
- Post D., 1989, "Moiré Interferometry for Composites," Chap. IV, *SEM Manual on Experimental Methods for Mechanical Testing of Composites*, M. E. Tuttle and R. L. Pendleton, eds., Society for Experimental Mechanics, Bethel, CT.
- Post D., 1980, "Optical Interference for Deformation Measurements -- Classical, Holographic and Moiré Interferometry," *Mechanics of Nondestructive Testing*, W. W. Stinchcomb, ed., Plenum Publishing Corporation, New York, pp 1-53.
- Rogers, C. A., Liang, C., and Li, S., 1991, "Active Damage Control of Hybrid Material Systems Using Induced Strain Actuators," Proceedings of the Thirty Second AIAA/ASME/AHS/ASC Structures, Structural Dynamics & Materials Conference, Baltimore, MD.
- Sirlin, S. W. and Laskin, R. A., 1990, "Sizing of Active Piezoelectric Struts for Vibration Suppression on a Space-Based Interferometer," Proceedings of the First Joint U.S./Japan Conference on Adaptive Structures, Maui, HI, U.S.A.
- Takagi, T., 1990, "A Concept of Intelligent Materials," *Journal of Intelligent Material Systems and Structures*, Vol. 1, pp 149-156.
- Vidussoni, M. A. and Griffin, O. H. Jr., 1990, "2-D to 3-D Global/Local Finite Element Analysis of Cross-Ply Composite Laminates," Center for Composite Materials and Structures Report, Virginia Polytechnic Institute and State University, CCMS-90-09.
- Wada B. K., Fanson, J. L., and Crawley, E. F., 1990, "Adaptive Structures," *Journal of Intelligent Material Systems and Structures*, Vol. 1, pp 157-171.
- Wang, B. and Rogers, C., 1991a, "Laminate Plate Theory for Spatially Distributed Induced Strain Actuators," *Journal of Composite Materials*, Vol. 25, pp 433-452.
- Wang, B. and Rogers, C., 1991b, "Modeling of Finite-Length Spatially-Distributed Induced Strain Actuators for Laminate Beams and Plates," *Journal of Intelligent Material Systems and Structures*, Vol. 2, pp 38-58.

## Vita

David Hilton Mollenhauer, born March 25, 1967, graduated from Texas A&M University in May 1990 with a Bachelor of Science degree in Aerospace Engineering. He had approximately one year of Cooperative Education work experience at the NASA Johnson Space Center. This work experience included a semester at the Propulsion and Power Division, the Crew and Thermal Systems Division, and the Advanced Programs Office, respectively. His work experience also includes two semesters of work on a Jet Propulsion Laboratory testing program conducted at Texas A&M University. This work involved the post impact buckling response of laminated plates. Currently, David is a civilian employee of the United States Air Force with the Palace Knight program. Upon graduation, he will be working at the Materials Laboratory at Wright Laboratories in Dayton, Ohio.

A handwritten signature in black ink that reads "David Hilton Mollenhauer". The signature is written in a cursive style and is positioned above a horizontal line.

David Hilton Mollenhauer